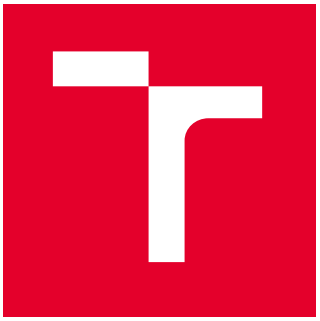

BRNO UNIVERSITY OF TECHNOLOGY

VYSOKÉ UČENÍ TECHNICKÉ V BRNĚ

FACULTY OF MECHANICAL ENGINEERING

FAKULTA STROJNÍHO INŽENÝRSTVÍ

ENERGY INSTITUTE

ENERGETICKÝ ÚSTAV

SUPERCAVITATION BEHIND AN OBSTACLE IN FLOW FOR USE IN WATER PURIFICATION

SUPERKAVITACE ZA PŘEKÁŽKOU V PROUDU PRO VYUŽITÍ V ČIŠTĚNÍ VODY

MASTER'S THESIS

DIPLOMOVÁ PRÁCE

AUTHOR — **Bc. Paulína Monková**

AUTOR PRÁCE

SUPERVISOR — **doc. Ing. Pavel Rudolf, Ph.D.**

VEDOUCÍ PRÁCE

BRNO 2024

BRNO UNIVERSITY OF TECHNOLOGY
FACULTY OF MECHANICAL ENGINEERING

Assignment Master's Thesis

Institut:	Energy Institute
Student:	**Bc. Paulína Monková**
Degree programm:	Power and Thermo-fluid Engineering
Branch:	Fluid Engineering
Supervisor:	**doc. Ing. Pavel Rudolf, Ph.D.**
Academic year:	2023/24

As provided for by the Act No. 111/98 Coll. on higher education institutions and the BUT Study and Examination Regulations, the director of the Institute hereby assigns the following topic of Master's Thesis:

Supercavitation behind an obstacle in flow for use in water purification

Brief Description:

A supercavitation is a continuous region in a liquid that is filled with water vapour that has been formed by the evaporation of the liquid when saturation vapour pressure is reached at a given temperature. One way to create supercavitation is to insert an obstruction in the pipe and form a vapour region behind the obstruction. Here, for example, a plasma discharge can then be ignited by inserting electrodes connected to a high voltage source.

Master's Thesis goals:

The student will use computational modelling to design a suitable body shape that will support the formation of a sufficiently large supercavitation region. Subsequently, the cavitator will be manufactured and experimentally tested on a hydraulic circuit in the laboratory of V. Kaplan Department of Fluid Engineering. Flow visualisation will be performed and basic hydraulic characteristics measured for different operating points.

Recommended bibliography:

FRANC, Jean-Pierre a MICHEL, Jean-Marie. Fundamentals of Cavitation. Springer, 2006. ISBN 978-1-4020-2233-3.

NESTERUK, Igor a SAVCHENKO, Yuriy N. Supercavitation: advances and perspectives. New York: Springer, [2012].

Deadline for submission Master's Thesis is given by the Schedule of the Academic year 2023/24

In Brno,

L. S.

doc. Ing. Jiří Pospíšil, Ph.D. Director of the Institute	doc. Ing. Jiří Hlinka, Ph.D. FME dean

ABSTRACT

The presented thesis deals with hydrodynamic cavitation behind an obstacle, which, in the future, could be used for water purification. In the introductory part, cavitation is characterized in general and the desired type of supercavitation is specified. The CaviPlasma device is marginally described in the thesis. This device is currently under development and is the first proposal for water purification in conjunction with hydrodynamic cavitation. In the next part of the thesis, the research that dealt with the shape of the body for cavitation is shown in more detail, where it was considered that ventilated cavitation, is not the subject of this thesis. From the conducted research, several body shapes were chosen. These body shapes were then compared using Ansys FLUENT software set as a 2D axisymmetric problem, and the body shape that appeared to be the most suitable was selected. A calculation with a user-defined function that adjusts the turbulent viscosity for the applied turbulence model was also made. Subsequently, the experimental track on which the selected body shape was successfully tested for the proposed diameter (40 mm), one larger diameter (42 mm) and one smaller diameter (38 mm) is presented in more detail. In the next part of the paper, the measured values are processed to obtain hydraulic characteristics. Additionally, the signals from acoustic emission sensor and pressure sensor records are evaluated. Finally, the experimental and simulation results are compared and then suggestions for solving the problems encountered in the work that could be improved are described.

Key words

Cavitation, supercavitation, water purification, CFD

ABSTRAKT

Predložená diplomová práca sa zaoberá hydrodynamickou kavitáciou za prekážkou, ktorá by mohla byť v budúcnosti využitá v zariadení za účelom dočisťovania vody. V úvodnej časti je bližšie charakterizovaná kavitácia všobecne a špecifikovaný typ superkavitácie, ktorý je žiadané vyvolať za obtekanou prekážkou. V práci je okrajovo opísané zariadenie CaviPlasma, ktoré je aktuálne vyvíjané a jedná sa o prvý návrh na dočisťovanie vody v spojení nízkoteplotného plazmového výboja s hydrodynamickou kavitáciou. V ďalšej časti práce sú bližšie zobrazené výskumy, ktoré sa zaoberali tvarom telesa na kavitáciu, kde sa jednalo o neventilovanú kavitáciu, ktorá je predmetom tejto práce. Z uskutočneného rešeršu boli následne vybrané tvary telesa, ktoré boli porovnané pomocou softvéru Ansys FLUENT pomocou 2D axisymetrickej úlohy. Zo simulácií bol následne vybraný tvar telesa, ktorý sa javil ako najviac vyhovujúci. Bol zhotovený výpočet s užívateľom definovanou funkciou, ktorá upravuje turbulentnú viskozitu pre použitý model turbulencie. Následne je bližšie priblížená experimentálna trať, na ktorej bol úspešne testovaný vybraný tvar telesa a to pre navrhnutý priemer (40 mm), a ďalej aj pre jeden väčší (42 mm) a jeden menší priemer (38 mm). V ďalšej časti práce sú vyhodnotené namerané veličiny ako hydraulické, tak aj spracované záznamy zo snímača akustickej emisie a tlakového snímača. V závere sú porovnané výsledky experimentu a simulácie a následne popísané návrhy riešenia problémov, ktoré sa v práci vyskytli.

Kľúčové slová

Kavitácia, superkavitácia, dočisťovanie vody, CFD

ROZŠÍRENÝ ABSTRAKT

Diplomová práca sa zaoberá návrhom telesa obtekaného vodou za účelom vyvolania hydrodynamickej kavitácie pre využitie pri dočisťovaní vody. Táto práca je súčasťou výskumu, ktorý prebieha v rámci vývoja zariadenia CaviPlasma. Výstupy z tejto práce by mali priniesť možnosť porovnania hydraulických veličín medzi existujúcim zariadením, zariadením opisovaným v tejto práci a poprípade inými navrhnutými zariadeniami.

Za telesom (ktoré je v tejto práci taktiež označované ako kavitátor) v prúde vody vzniká oblasť s nízkym tlakom. Pri dostatočne nízkom tlaku dochádza ku fázovej premene vody na vodnú paru. Táto fázova premena sa označuje ako kavitácia. Pri ďalšom znižovaní tlaku dochádza k vytvoreniu súvislej oblasti vyplnenej vodnou parou. Tento režim kavitácie, kde je oblasť pary súvislá sa nazýva superkavitácia.

Cieľmi práce bolo vybrať vhodný tvar telesa, za ktorým by v prúde vznikala superkavitácia s dostatočnou dĺžkou, vyhotovenie navrhnutého telesa, následné otestovanie telesa na hydraulickom okruhu a vyhotovenie vizualizácie. Ďalším z cieľov práce bolo spracovanie nameraných dát do hydraulických charakteristík pre rôzne pracovné body.

V práci je priblížená kavitácia všeobecne, ďalej sú bližšie popísované jednotlivé typy kavitácie, mechanizmy jej vzniku a kavitačné režimy. Bližším popisom superkavitácie a rozlíšením ventilovanej a parnej superkavitácie je vyzdvihnutý požiadavok nízkeho tlaku v oblasti vyplnenej parou, ktorý špecifikuje, že práca sa nezaoberá ventilovanou kavitáciou, t.j. kavitáciou s prisávaním vzduchu.

Súčasťou práce je aj základný popis funkcie zariadenia CaviPlasma, ktoré je patentovaným zariadením. Sú uvedené možnosti, ako je možné toto zariadenie využiť a taktiež sú uvedené hydraulické charakteristiky tohto zariadenia, ktoré boli merané v laboratóriu V. Kaplana, odboru fluidného inžinierstva.

Súčasťou rešeršnej časti práce je uvedenie aktuálnych poznatkov o vplyve tvaru telesa na kavitačnú oblasť, sú uvedené príklady tvarov telies, ktoré boli overované. Z rešeršu o vplyve rôznych tvarov telies na kavitačnú oblasť boli vybrané štyri. Z nich bol pomocou CFD simulácií v programe Ansys FLUENT urobený výber najvhodnejšieho tvaru. Okrajové podmienky zadávané do simulácií vychádzali z možností laboratória V. Kaplana. Simulácie boli nastavené na podtlak -50 000 Pa na výstupe definovanej domény. Tento podtlak je maximálnym podtlakom, ktorý bol pri experimentoch v tlakovej nádobe použitý. V tejto časti práce sú definované aj ďalšie obmedzujúce vstupy.

Pomocou 2D axisymetrických, tranzientných simulácií bol v rámci návrhu vybraný tvar dvojklinového kužeľa, ktorý vykazoval dostatočne dlhú kavitačnú kapsu, ale zároveň nevykazoval najvyššie straty. Závery, ktoré boli dosiahnuté pomocou porovnania CFD simuláciami boli v zhode so závermi získanými v z rešeršnej časti v práci Gopala Krishnan *et al.* (2019), z ktorej boli vybrané návrhy tvarov do tejto práce. V rámci popisu simulácii sú priblížené parametre siete, okrajové podmienky, použitý model turbulencie a použitý multifázový model ktoré boli pre simuláciu nastavené. Ďalším krokom v práci bolo pre vybraný tvar telesa vo výpočte zahrnúť úžívateľom definovanú funkciu (UDF), ktorej účelom je upraviť turbulentnú viskozitu, keďže vybraný model turbulencie potláča fázovú premenu. V rámci výpočtov s UDF bolo zistené, že tieto výpočty sú oveľa citlivejšie na kvalitu siete. V rámci simulácií s UDF boli taktiež pozorované dva nefyzikálne javy, a to vznik kavitácie v bode na stene trubice a oblasť v okolí osi symetrie, kde nenastávala fázová premena. Z dôvodu, že v oblasti osi symetrie nenastávala fázová premena, bolo usúdené, že 2D axisymetrická úloha nie je vhodná a bolo by výhodné vyhotoviť výpočty pre 3D doménu, ktoré budú ale časovo omnoho náročnejšie na výpočet. Pre vysvetlenie vzniku kavitácie na stene bolo vyhotovených niekoľko sietí, s rôznym počtom buniek a rôznou kvalitou siete. Tento jav sa však pre žiaden prípad nastavenia siete nepodarilo odstrániť.

V rámci experimentálnej časti práce je kladený dôraz na výrobu samotného navrhnutého tvaru telesa a to aj s výberom materiálu a riešením uchytenia telesa do trubice. Boli porovnané materiály PETG a PLA, kde boli kavitátory s troma navrhnutými typmi uchytenia vytlačené pomocou 3D FDM tlače so 100% výplňou. Tieto materiály a typy uchytenia boli podrobené statickému záťažovému testu a následne bol vybraný materiál PETG a najvhodnejšie uchytenie. Celkovo bolo vytlačených päť priemerov kavitátoru s geometriou dvojklinového kužeľa. Po vytlačení geometrií bola pracovníkmi laboratória ústavu V. Kaplana zostavená meracia trať osadená snímačmi. Boli merané veličiny prietoku, teploty, tlaku pred a za kavitátorom, akustickej emisie a pomocou vysokorýchlostnej kamery bola zhotovená vizualizácia prúdenia. Pri vizualizácií však pre niektoré prípady nebolo možné zachytiť celú dĺžku kavitačného mraku a to z dôvodu nedostatočnej dĺžky svetelného kužeľa, ktorý slúžil na podsvietenie.

Výstupmi z experimentálnej časti sú spracované dáta v podobe hydraulických charakteristík a ďalších závislostí ako je napríklad aj závislosť hydraulického výkonu na kavitačnom čísle, a spracovenie signálu akustickej emisie a signálu z tlakového snímača za telesom do podoby závislosti kavitačného čísla na amplitúde a frekvencii píku získaného z FFT pre jednotlivé pracovné body. Výstupom je aj závislosť kavitačného čísla na RMS zo snímača akustickej emisie.

V rámci experimentálnej časti boli naviac namerané a spracované dáta aj pre kavitátory v prúde otočené opačným smerom, teda s vodou natekajúcou na plochú časť kavitátora. Pri tejto konfigurácii dochádzalo ku vzniku samotnej kavitácie aj superkavitácie pri vyšších kavitačných číslach.

V závere práce je porovnaná simulácia s experimentom, pre rovnaké nastavenie tlaku a prietoku a vyzdvihnuté vzniknuté rozdiely a možnosť ich príčiny.

BIBLIOGRAFICKÁ CITACE

MONKOVÁ, Paulína. *Superkavitace za překážkou v proudu pro využití v čištění vody*. Brno, 2024. Dostupné také z: https://www.vut.cz/studenti/zav-prace/detail/158172. Diplomová práce. Vysoké učení technické v Brně, Fakulta strojního inženýrství, Energetický ústav. Vedoucí práce Pavel Rudolf.

AUTHOR'S DECLARATION

I declare that I have written this master's thesis on **Supercavitation behind an obstacle in flow for use in water purification** independently, under the guidance of the advisor and using the technical references and other sources of information cited in this paper and listed in the comprehensive bibliography at the end of this thesis.

Date *Paulína Monková*

ACKNOWLEDGEMENT

I would like to thank doc. Ing. Pavel Rudolf, Ph.D. for profesional guidance and for opportunity to be part of a project regarding CaviPlasma device.

Big thanks go also to the staff of laboratory of V. Kaplan departement. Ing. Martin Hudec Ph.D., Bc. Matěj Ostrezi and Bronislav Kusý for their hard work, time and help.

And last but not least, I would like to thank my family for standning by my side and cheering me on every step of the way.

CONTENTS

INTRODUCTION

Cavitation has been perceived as an unwanted phenomenon in engineering for a very long time. It was first described in 1895 by S. W. Barnaby. It lowers the performance of machines and has negative effects on materials.

In 2010 prof. prof. Ing. František Pochylý, CSc. and Ing. Blahoslav Maršálek, CSc. came with an idea to remove cyanobacteria from water using cavitation. This method was partially succesfull as the cyanobacteria have a high regenerative capacity. To achieve greater efficiency, the combitation of cavitation with other physical effects was required. In years 2017 – 2018, doc. Ing. Pavel Rudolf, Ph.D. came with an idea to combine hydrodynamic cavitation with low temperature plasma discharge. This invention combined many benefits and proved to be effective when removing micropollutants from water. In order to better understand the events taking place in the CaviPlasma device, a basic research project sponsored by the grant agency of Czech Republic is under way. The first CaviPlasma design used a venturi nozzle for inducing cavitation.

This work is part of a larger research, focused on gaining knowledge on the hydraulic behaviour of different types of inducing cavitation. The scope of this work includes the entire process from the research of existing obstacle shapes, through the production of the suitable body to the evaluation of the results gained from the experiment. Outcomes of this work should aid in choosing of the most suitable method of inducing cavitation with regards to efficiency and meeting given requiremens such as length of the cavity. At the same time, this work is the first work at Viktor Kaplan's institute that deals with the induction of cavitation behind an obstacle. For this reason, it provides initial knowledge of problems that occurred during the work and require further improvement.

1 Cavitation

Cavitation is a phenomenon in a liquid characterised by the formation, development, and collapse of cavitating cavities - bubbles. The name cavitation is based on the Latin word "cavitas", which generally means cavity. Cavitation in a liquid represents a disruption of its continuity, it occurs when a certain state of the liquid is reached at a given location. This state is determined mainly by the pressure and temperature of the liquid. Thus, if the pressure at a given location drops to a certain value called cavitation pressure, at a given temperature of the liquid, the continuity of the liquid is broken, and an observable small cavitation bubble is formed. If the pressure value decreases or remains the same, the bubble gradually increases in size. When a cavitation bubble is formed in a flowing liquid, the bubble moves to a region of higher pressure than the cavitation pressure and here it abruptly disappears, implodes. When the bubble disappears close to the wall the so call jet depicted in *Figure 1-2* occurs. [1]

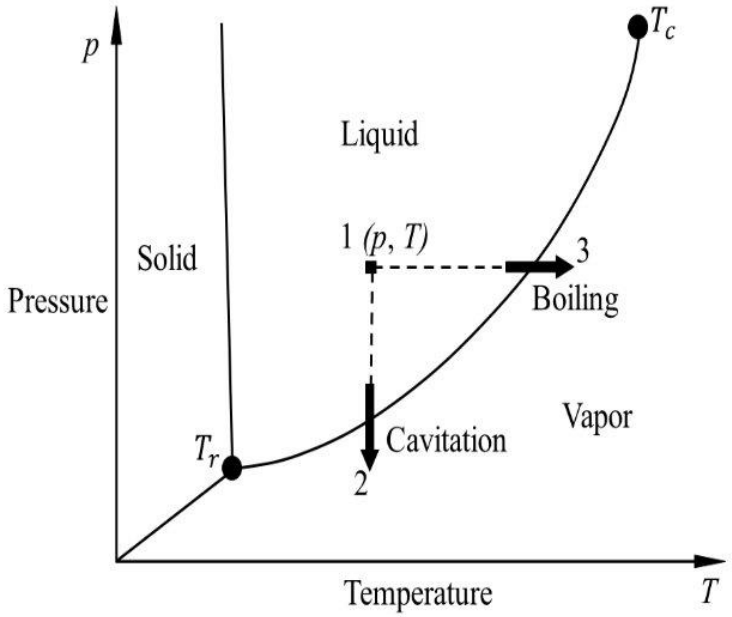

Figure 1-1 Schematic of phase diagram of water. Where p is pressure, T is temperature, T_r represents temperature corresponding to triple point and T_C temperature corresponding to critical point.[2]

Cavitation is a long-term problem in technical practice. The cavitation phenomenon itself was first described in 1895 by S. W. Barnaby, who explains it as the formation of steam bubbles. Cavitation caused a reduction in performance of ship propellers (failure to achieve design values), rapid and significant damage to the wrapped parts. Currently, the occurrence of cavitation is recorded mainly in water turbines, hydrodynamic and hydrostatic pumps, in hydrodynamic transmissions, in fittings, in jet devices, in hydrodynamic bearings, in water-cooled combustion engines, in gear transmissions, and in ship propellers and torpedoes. From the theoretical point of view there are three main steps in the formation of cavitation: breakdown (void creation), filling the void with vapor and saturation with vapor. The speed of these steps happening is so rapid that we can assume instantaneous saturation of the void with vapor. After the bubble is formed and moved into area of higher pressure, it collapses. The collapse of the cavitation bubble is a very fast process, much faster than the formation itself. The collapse of

the cavitation bubble can occur in two environments: symmetrical and non-symmetrical (near the wall). The implosion of the vapour bubbles occurs in microseconds (the speed of sound), generating light, noise, shockwaves, and microjets. For the bubble collapse near the wall, the interface close to the wall tends to flatten while a hollow develops on the opposite face with a change in curvature under a very high pressure. Then, a re-entrant jet, directed towards the solid wall, develops, with a rapidly increasing velocity. Finally, the jet pierces the bubble and strikes the solid wall as shown in *Figure 1-2*. The pressure inside the imploding bubbles can reach up to 10 MPa, and for a brief period, the surface of the bubbles can reach extremely high local temperatures (several thousand Kelvin). However, the high temperature occurs for a very short time and therefore, there is no heat exchange. Implosion of vapour bubbles is extremely quick and often erodes nearby surfaces. [3]

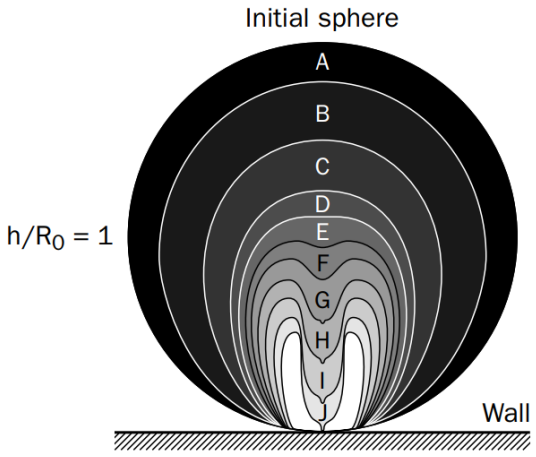

Shape	Time	Velocity (m/s)
A	0.63	7.7
B	0.885	19
C	0.986	42
D	1.013	65
E	1.033	100
F	1.048	125
G	1.066	129
H	1.082	129
I	1.098	128
J	1.119	128

Figure 1-2 - Numerical results of Plesset and Chapman (1971) for the collapse of a bubble near a wall [3]

Types of cavitation

- **Gas cavitation** occurs with a liquid in a saturated state. This process is then more likely in liquids with larger cavitation nuclei. If a saturated liquid experiences a decrease in pressure, it becomes a gas supersaturated liquid. This gas is expelled and passes into the bubble. This causes the bubble to expand to a new, larger, equilibrium size. The released air reaches the bubble interface by diffusion from the surrounding liquid. The diffusion is best explained by Henry's law *"Gas will dissolve in a fluid until there is an equilibrium between the partial pressure of the gas and the pressure in the fluid."*. Because diffusion is a slow process, gas cavitation is also a slow process. [4]
- **Vapour cavitation** - When a flowing liquid's local static pressure falls below its saturated vapour pressure at its actual temperature, **vapour cavitation** takes place, resulting in the formation of vapour bubbles. These vapour bubbles then almost immediately collapse or implode when the local static pressure of the liquid rises above the saturated vapour pressure of the liquid at the actual temperature (i.e. phase changes from liquid to vapour and back to liquid). [4]

- **Pseudocavitation** appears when gas bubbles are present inside of a liquid with large initial radius and the pressure lowers. The bubbles then increase steadily in size without evaporation of the liquid.

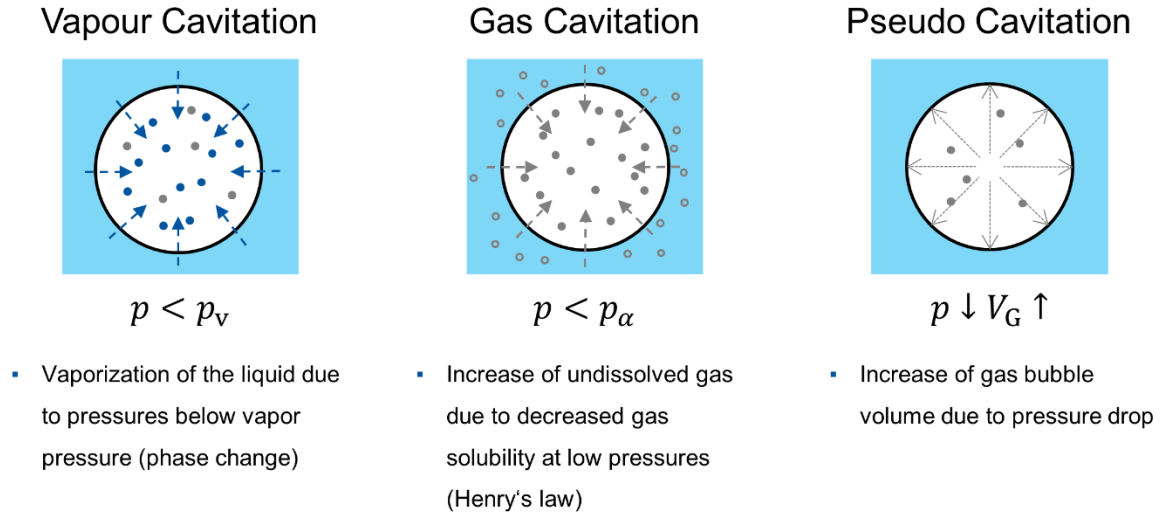

Figure 1-3 Types of cavitation [4]

There are several mechanisms of cavitation formation:

- Hydrodynamic cavitation is the most common type and is also the type that will be looked at in this work. Hydrodynamic cavitation appears in cases, when pressure drops due to narrowing of the flow area and increases in speed.
    - Vortex cavitation is a special case of hydrodynamic cavitation. This cavitation forms in the core of the vortex occurring in the liquid. It is the result of a reduction in the pressure of the vortex compared to the pressure in the surrounding fluid.
- Acoustic cavitation is intentionally induced cavitation. This type of cavitation is induced in a still, non-flowing fluid by the introduction of a high-frequency, large-amplitude pressure wave. The pressure waves thus induce vibration of the fluid and cavitation bubbles are formed and disappear within the amplitude changes of these waves. Acoustic cavitation has been extensively exploited for biological applications in the form of bioprocessing and drug delivery/uptake.
- Vibration cavitation – in stationary liquid the cavitation can occur due to oscillation of solid surfaces in liquid. This movement of solid surfaces induces pressure waves. When the surfaces move apart from each other, the pressure lowers. The pressure can fall below the cavitation pressure when cavitation bubbles are created. Then, when the walls move back towards each other, these bubbles vanish. The acceleration of the wall's surface determines the amount of pressure decrease in the liquid. The need to refer to vibration cavitation is because vibrational cavitation is not intentionally created, in contrast to acoustic cavitation. This method is used in cavitation erosion testing according to norm ASTM G132-96 Standard Test Method for Pin Abrasion Testing [5].

- Optic cavitation (laser) – the energy needed to form the bubble is provided by a pulsed laser focused in and absorbed by the liquid. Process of bubble formation is mediated by the breakdown of water through the generation of a plasma. [6]

Jean-Pierre Franc and Jean-Marie Michel in their work *Fundamentals of Cavitation* define three main forms of vapor cavities:

- Transient isolated bubbles – they grow from small air nuclei present in the liquid due to low pressure and are carried downstream by the flow. They disappear once they enter areas with high enough pressure.
- Attached or sheet cavities – oftentimes found forming from the leading edge of a body or foil.
- Cavitating vortices – this cavitation appears in the core of vortices due to sufficiently low pressure.

Some patterns do not fall easily into these categories.

It is useful to distinguish cavitation regimes as [7]:

- Limiting regime – this regime is between cavitating flow and non-cavitating flow.
- Regime of developed cavitation – in this regime, in case of attached cavities another distinction can be made:
    - Partial cavities – They usually develop in regions of separated flow. Initially, cavitation appears in the shear layers. As cavitation number (described in 1.1) is further decreased, it turns into a supercavity.
    - Supercavities – their closure is downstream the foil, inside the liquid domain.

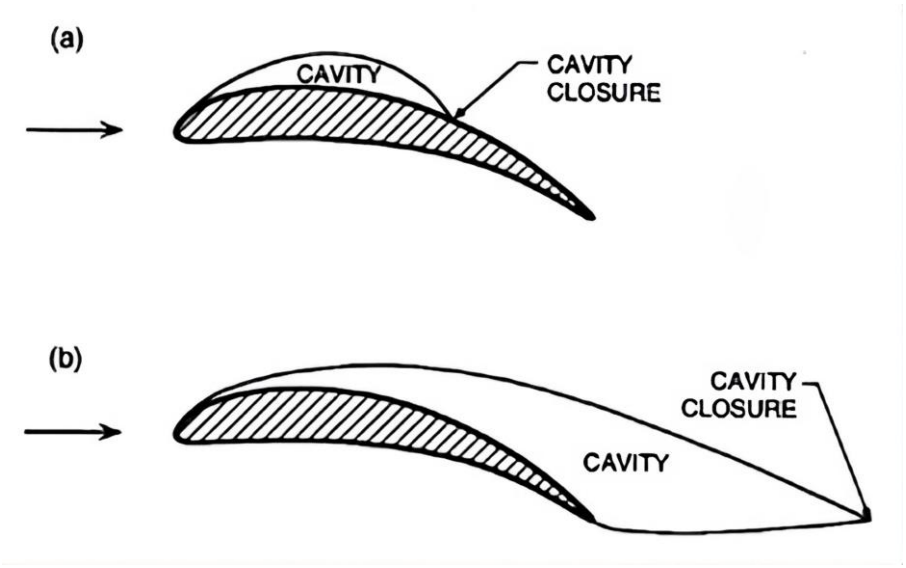

Figure 1-4 Sketch of the types of attached cavitation on a lifting foil. (a) partial cavitation; (b) supercavitation [8]

In this work the focus is on the positive impact of cavitation on water treatment, which has been studied in recent years. The main objective is the supercavitation formed behind an obstacle (cavitator). Another form of water treatment using cavitation will be described in chapter 2.

1.1 Cavitation number

Cavitation number can be defined primarily as a proportion of pressure difference to dynamic pressure,

$$\sigma_v = \frac{p_r - p_v(T)}{\rho \frac{v^2}{2}} \qquad (1.\ 1)$$

Where:

σ_v	cavitation number	[-]
p_r	pressure at reference	[Pa]
p_v	vapor pressure (temperature dependent)	[Pa]
$\rho \frac{v^2}{2}$	dynamic pressure	[Pa]

or can be defined as

$$\sigma_v = \frac{p_r - p_v(T)}{\Delta p} \qquad (1.\ 2)$$

Where:

Δp	pressure difference characteristic to the system	[Pa]

Cavitation number is a non-dimensional parameter. It can be said, that the lower the cavitation number, the higher the probability of cavitation. It is important to note, that the cavitation number is defined using dynamical parameters and not the geometrical ones.

In non-cavitating flows, this parameter can't be considered as a scaling parameter. The difference between reference pressure p_r and vapor pressure p_v has no physical significance for single phase flow. The cavitation number becomes a similarity parameter only at cavitation inception.

1.2 Supercavitation

Supercavitation can be classified as vapor or ventilated. Vapor cavities are formed by the combination of smaller cavities whereas in the ventilated cavitation, gases are released into the cavitating bubble by the cavitator or a nearby water surface. [9]

Supercavitation is a condition when the cavitation parameter is decreased below the critical value. The small cavity attached to the hydrofoil extends and grows longer. It becomes a supercavity as soon as it ceases to enclose the cavitator and forms a single cavity. The

supercavitating object is surrounded by a stable and predictable bubble formed by this single, enormous cavity. These days, supercavitation surrounding an object is typically employed to lessen drag on objects in motion, like torpedoes. [9] The drag is made up of viscous and pressure components. During supercavitation, the viscous drag is decreased due to reduction of shear stress near the body and pressure drag increases. Nonetheless, there is a noticeable drop in the overall drag force. [10] The most common example of supercavitation is that of a hydrofoil. In such case the drag on the foil increases, while the lift of the foil decreases.

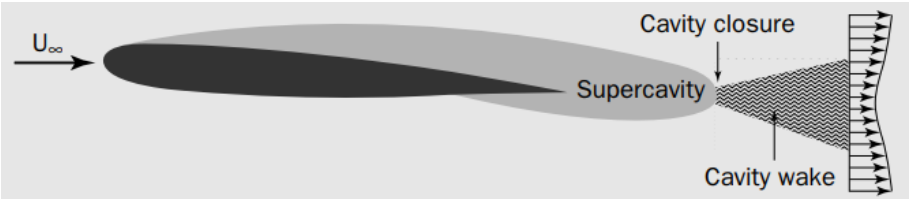

Figure 1-5 Scheme of supercavitating flow [3]

The position of detachment is unknown beforehand if there is no sharp edge or step to fix the detachment point of the cavity. The detachment criterion is necessary to predict the location of the cavity detachment. There are two main criteria that can be used:

- Villant-Armstrong criterion – established on the inviscid two-dimensional flow theory. The cavity must detach tangentially to the solid wall. This criterion assumes, that the cavity is the zone of minimum pressure for the whole field.

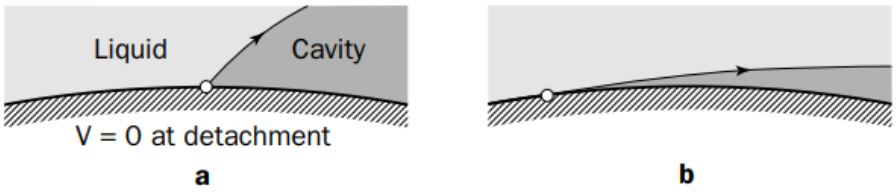

Figure 1-6 a) non-tangential detachment b) tangential detachment [3]

- Laminar separation criterion – Viscosity effects predominate in cavitation inception, as demonstrated by Arakeri and Acosta's analysis of cavitation inception on spheres, circular cylinders, and ogives. They demonstrated that the presence of laminar separation on a wall creates an inception site, and that inception is strongly impacted by the removal of an existing laminar separation caused by stimulating the boundary layer with a trip. Arakeri (1975) developed a criterion based on those trials to forecast the cavity's detachment position. The local effects of surface tension are also considered by this criterion, which requires the free streamline to be non-tangential to the body at detachment. According to the laminar separation criterion, a supercavity separates at the boundary layer's laminar separation point. The position of laminar separation, and even its existence in some cases, may strongly differ from the case of the fully wetted flow because of the changes in pressure distribution due to the developed cavitation.

Cavity detachment really occurs slightly downstream of laminar separation as surface tension causes the cavity to bend locally as shown in Figure 1-7. [3]

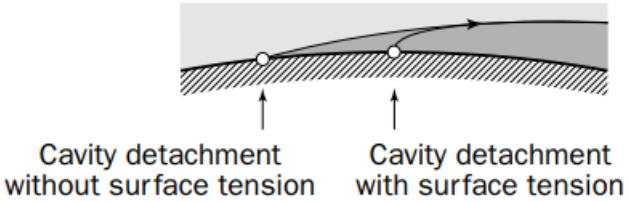

Figure 1-7 Effect of surface tension [3]

1.2.1 Main parameters of axisymmetric cavities [3]

In the case of a disc or cone cavitator, the shape of the cavity approaches an ellipsoid whose length l and maximum diameter d_c can be expressed versus σ_c by the following asymptotic equations, if gravity is disregarded and the relative underpressure σ_c of the cavity is small enough (usually for $\sigma_c < 0{,}1$):

$$\begin{cases} \dfrac{d_c}{d} = \sqrt{\dfrac{C_D}{\sigma_c}} \\ \dfrac{l}{d} = \dfrac{1}{\sigma_c}\sqrt{C_D ln\dfrac{1}{\sigma_c}} \end{cases} \qquad (1.\ 3)$$

Where:

d_c	Maximum diameter	[m]
d	Diameter of a cavitator	[m]
l	Length of an ellipsoid	[m]
σ_C	Relative underpressure	[-]
C_D	Drag coefficient	[-]

Where drag coefficient C_D is defined as:

$$C_D = \frac{D}{\frac{1}{2}\rho v_\infty^2 \frac{\pi d^2}{4}} \qquad (1.\ 4)$$

Where:

D	Drag force	[N]
ρ	Water density	[kg/m^3]
v_∞	Ambient velocity	[m/s]

is connected to its value $C_D(0)$ for $\sigma_c = 0$ by:

$$C_D(\sigma_c) \approx (1 + \sigma_c) C_D(0) \tag{1. 5}$$

and relative cavity underpressure is defined as:

$$\sigma_c = \frac{p_\infty - p_c}{\frac{1}{2}\rho {v_\infty}^2} \tag{1. 6}$$

Where:

p_∞	Ambient pressure	[Pa]
p_c	Cavity pressure	[Pa]

Equation (1. 3) can be obtained from the momentum balance of the liquid contained in the domain. The domain is shown in Figure 1-8. The surface $\sum_\infty$ is made up of a tupe of streamlines, surface S_u is at upstream at infinity and surface S is an annular surface made of a cross section along the cavity. The domain is closed by the cavitator and part of the cavity interface. The momentum balance leads to the calculation of the drag force D:

$$D = (p_\infty - p_c) S_c - \iint_S (p - p_\infty) \mathrm{d}S + \rho v_\infty^2 S_u - \iint_S \rho v_v^2 \mathrm{d}S \tag{1. 7}$$

Where:

S_c	Cross-section area of the cavity	[m^2]
S_u	Limiting surface at upstream	[m^2]
p	Pressure	[Pa]
p_∞	Ambient pressure	[Pa]
v_x	Axial velocity	[ms^{-1}]
v_∞	Ambient velocity	[ms^{-1}]

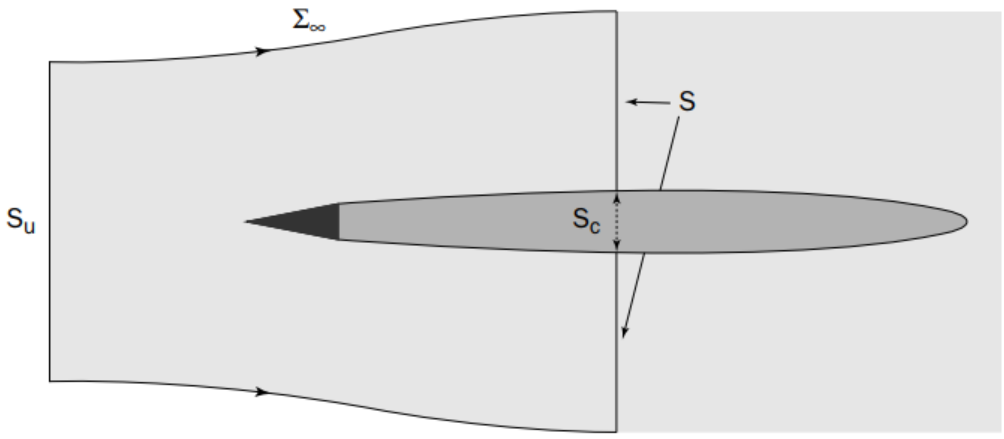

Figure 1-8 Domain for momentum equation [3]

The mass conservation equation between cross-section S_u and S can be expressed as:

$$\rho v_\infty S_u = \iint_S \rho v_x dS \qquad (1.\ 8)$$

The momentum balance becomes:

$$D = (p_\infty - p_c)S_c - \iint_S (p - p_\infty)\mathrm{d}S + \iint_S \rho v_x (v_\infty - v_x)\mathrm{d}S \qquad (1.\ 9)$$

After expressing pressure from the Bernoulli equation as:

$$p - p_\infty = \frac{1}{2}\rho(v_\infty^2 - v_x^2) - \frac{1}{2}\rho v_r^2 \qquad (1.\ 10)$$

Where:

v_r Radial velocity [m/s]

we can obtain drag force as:

$$D = (p_\infty - p_c)S_c - \iint_S \frac{1}{2}\rho(v_\infty^2 - v_x^2)\mathrm{d}S + \iint_S \frac{1}{2}\rho v_r^2 \mathrm{d}S \qquad (1.\ 11)$$

1.3 Ventilated supercavitation

While vapor cavities arise naturally, ventilated cavities are created artificially by injecting gas into the low-pressure areas of liquid flows. In ventilated supercavities, gas pressure can be high, mostly due to ambient pressure and the injection flowrate. Ventilation decreases the relative cavity underpressure σ_c by increasing the cavity pressure, so that large artificial cavities comparable with vapor supercavities can be obtained. Nonetheless, ventilated and vapor supercavities differ in two key ways:

- The gas behaves differently at the **rear portion** of the cavity **due to its non-condensable nature**. Because of the effects of gas compressibility, this relies on the ambient pressure.
- Since huge voids are produced even at low velocities, gravitational effects are to be expected.

The gas flowrate that must be injected into the wake to achieve a specific cavity length, drag, or lift is a crucial parameter.

Ventilation is currently used to limit the risk of erosion in spillways of large concrete dams, where a large amount of water must be discharged in a short time, in ventilated hydrofoils or propellers and supercavitating torpedoes.

Unsteady, axisymmetric supercavity flows are encountered especially when the relative cavity underpressure is time-dependent, either because of external pressure changes (as in the

case of vertical motion of the cavitator in a gravity field), or because the pressure inside the cavity is time-dependent, which is generally the case for ventilated cavities.

1.3.1 The main parameters of ventilated supercavitation

The cavity main parameters like length, lift or drag are dependent on the relative cavity underpressure σ_c:

$$\sigma_c = \frac{p_r - p_c}{\frac{1}{2}\rho v^2} \qquad (1.\ 12)$$

The pressure inside the cavity is a summation of vapor pressure and the pressure of the injected air as shown in equation (1. 13), however for ventilated supercavities, vapor pressure p_v is generally negligible.

$$p_c = p_v + p_{air} \qquad (1.\ 13)$$

From this equation it is obvious, that pressure inside the cavity of ventilated supercavitation is higher than that of a vapor cavity. [8]

2 CaviPlasma

Cavitation is usually an unwanted phenomenon in technical practise, however for years the beneficial effect of cavitation has been used, for example to kill cyanobacteria and bacteria in water treatment, to create emulsions and in other applications. Several ways of inducing cavitation have been tested such as orifice plate (simple design that worked least), cavitating nozzle, rotating cavitator. These methods however had unsatisfactory results. The closeup picture of previously tested design of CaviPlasma, which is currently the most promising device, can be seen in Figure 2-1.

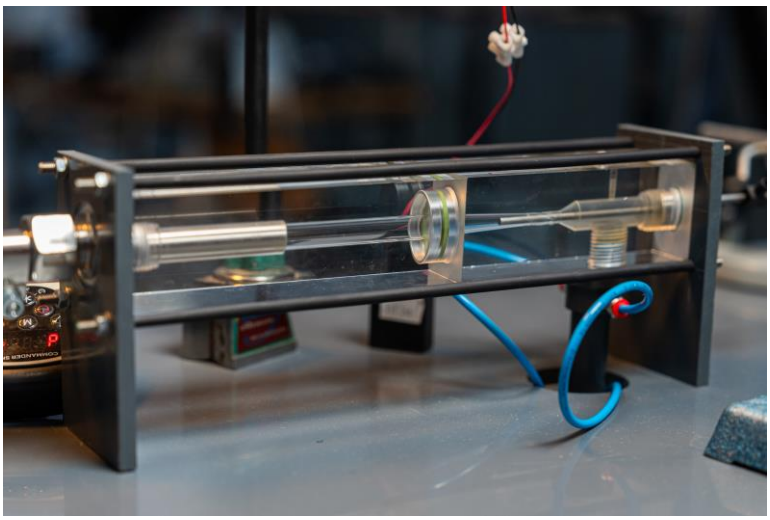

Figure 2-1 CaviPlasma design of the convergent-divergent nozzle with an electrode for measurement of hydraulic characteristics.

The CaviPlasma device is patented technology [11], on which several studies are currently being done to ensure the most effective way of water treatment. There are physical and chemical effects that ensure cavitation is a great tool for water treatment. The mechanical (physical) processes enhance reactions in a gas-liquid system. These effects include extreme temperature, pressure, and turbulence generated from the collision of bubbles. The large number of bubbles can produce powerful shockwaves that are destructive to materials during the collapse of a bubble and can also damage cell walls. Chemical effects include production of free radicals due to the dissociation of water molecules. These radicals can induce various chemical reactions that involve processes in equations (2. 1) and (2. 2). However, cavitation as a physical process produces very low amounts of chemical reactions. By combining the effects of cavitation and low temperature plasma discharge, the number of chemical reactions is considerably higher, and the higher number of produced radicals can significantly affect the final quality of water.

$$H_2O \rightarrow H\cdot + OH\cdot \qquad (2.\ 1)$$

$$OH\cdot + OH\cdot \rightarrow H_2O_2 \qquad (2.\ 2)$$

Direct generation of electrical discharges in liquids is complicated mainly due to the required high breakdown strength of liquids, higher than 1 MV/cm. Introduction of the gas-

phase allows reduction of the breakdown strength to technically more feasible values of 10 kV/cm. To ignite plasma discharge, the gaseous environment must be created. There are several ways in which the gaseous environment can be ensured:

- Evaporation of water by high temperature on the electrode – this solution is extremely energy demanding and disadvantageous.
- Air intake either through bubbling or air intake – this solution is less demanding in energy consumption, however, the plasma discharge in atmospheric pressure is rather short, approximately 1,5 – 2,5 cm, which is not sufficient for water purification.
- Cavitation – with cavitation, the low pressure in the cavity (non-ventilated) is favourable when using plasma discharge. In low pressures, plasma discharge can be relatively long, approximately 20 cm with a low breakdown voltage 1 kV/cm.

An advantageous low-pressure environment can be obtained by non-ventilated cavitation. In this type of low-pressure gas-phase environment, which is formed inside the flowing liquid, even a moderate high-voltage field of 1 kV/cm can sustain discharge plasma in a considerable amount of liquid.

Today, there are two possible applications for CaviPlasma:

- Water treatment – relatively lightly polluted water flows through the region in between electrodes with plasma discharge where the cavitation is induced. This combination can degrade persistent pollutants such as pesticides, herbicides, anticonception, drug residues and fluorinated substances that are in water in relatively low concentrations, but they cannot be broken down in the body, so they accumulate.
- Production of plasma activated water (PAW) – in agriculture, the exposure of seeds to PAW can lead to a better seed germination process and growth, PAW has strong bactericidal effect, other applications of this water include chemical synthesis, nanoparticle synthesis, and other.

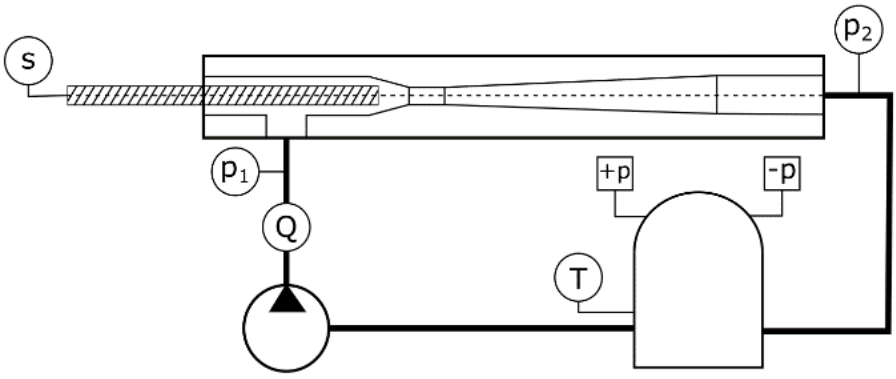

Figure 2-2 Schematic illustration of an experimental setup of experiments with the convergent-divergent nozzle [12]

The previous design of CaviPlasma was made of the convergent-divergent (CD) nozzle with high voltage electrode inside the throat and ground electrode downstream. The schematic sketch of the device is shown in Figure 2-2 and the detail of the CD nozzle with a high voltage electrode is shown in Figure 2-3. On this setup removal of cyanobacterial biomass was tested. The experimental evaluation conducted on this device with ignition of cold plasma discharge showed that hydrodynamic cavitation was able to cause the collapse of gas vesicles of Microcystis cells, while plasma treatment halted metabolic activity of biomass and during this process, the integrity of the cell remained undamaged. [12]

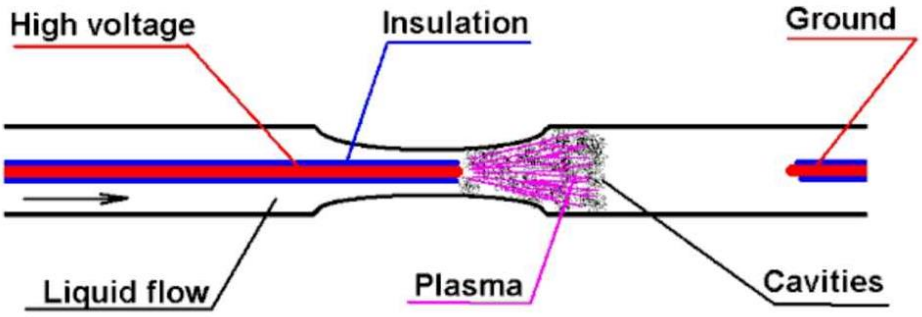

Figure 2-3 Detail of the electrode inside the throat of CD nozzle [12]

In the work Hydraulic characteristics of the convergent-divergent nozzle with the inner electrode in cavitating conditions [13], the hydraulic characteristics were developed based on the calculated loss coefficient and the cavitation number. Three different nozzles were tested, with neck diameters of 3, 4 and 5 mm. The inner electrode was set for several positions. From the results, it was concluded, that the insertion of an electrode has no effect up to 2 mm before the neck. It appeared to be most advantageous to use the nozzle with the neck diameter of 5 mm and an electrode in the convergent part of the nozzle, near the throat, as this arrangement offered relatively small losses and a low cavitation number, which was desired. Hydraulic characteristics of the nozzle with a neck diameter of 5 mm can be seen in Figure 2-4 through *Figure 2-6*, where the black cross marks the cavitation inception.

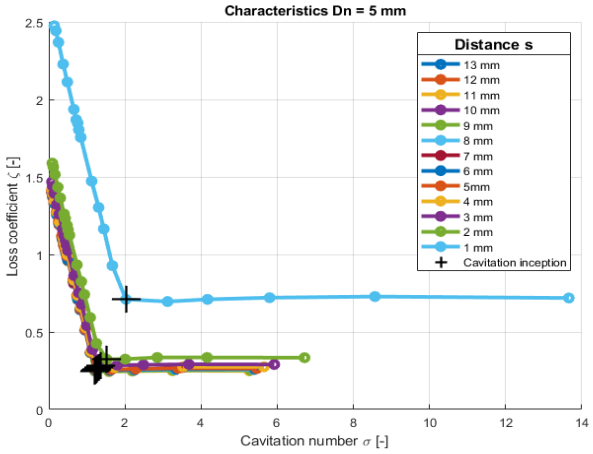

Figure 2-4 Hydraulic characteristic of CD nozzle with neck diameter of 5 mm – convergent section [13]

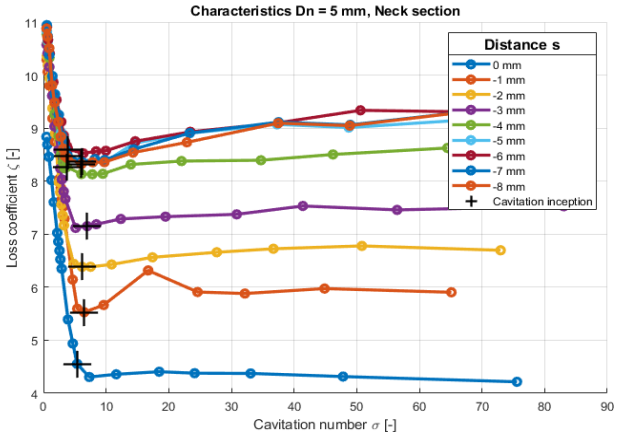

Figure 2-5 Hydraulic characteristic of CD nozzle with neck diameter of 5 mm – neck section [13]

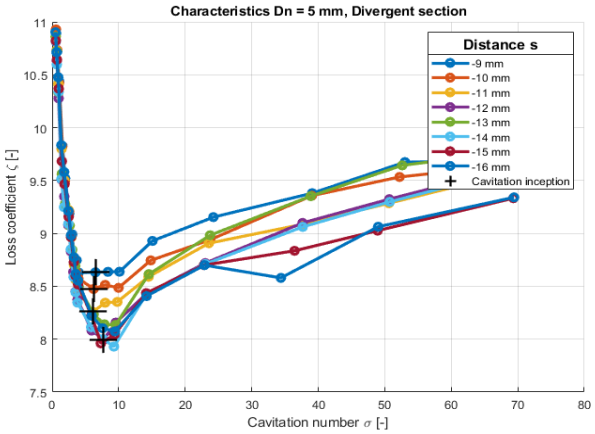

Figure 2-6 Hydraulic characteristic of CD nozzle with neck diameter of 5 mm – divergent section [13]

3 Choice of geometry for the cavitator

Cavitator (the obstacle inserted into a stream behind which cavitation occurs) affects cavity size as well as the magnitude of losses. The aim is to find the best shape of the cavitator that is easy to manufacture and provides sufficient cavity size while producing minimum drag. Since the cavitator will be located upstream to the end of a high voltage electrode to generate a gaseous environment for the plasma ignition, it must be designed so it would allow the high voltage electrode to be routed through the cavitator. The supercavity length must span from the cavitator to the grounding electrode.

3.1 Previous research

Shafaghat *et al.* (2011) applied the NSGA-I optimization technique to optimize the size of the cavitator. They employed the rational parabolic curve, which can be seen described by equation (3. 1) Figure 3-1. The optimization of results showed, that for a specific cavitation number, as the required cavity length became longer, the drag coefficient increased and the optimum shape of the cavitator changed from a long flat nose shape to a short smooth one. [14] The definition of shape that was used in the optimization is shown in Figure 3-1 with equation (3. 1). Moghimi *et al.* (2016) conducted experiments focusing mainly on parabolic cavitators. Experiments were carried out in a high-speed water tunnel but due to insufficient velocity, the absolute pressure of the tunnel was reduced, and air was injected into the cavity. Therefore, the cavitation in their experiments was artificial. However, they concluded that cone cavitators with low wertex angles have low drag but create cavities with short lengths and diameters. By increasing the wertex angle the cavity elongates but the drag is increased. The disk cavitators create large cavities but also create a large drag force. Parabolic cavitators can combine the sufficient length of a cavity while also lowering the drag. [10] Gopala Krishnan *et al.* (2019) tested several cavitator types using CFD 2D axisymmetric simulations. The cavitators they tested are shown in Figure 3-2. For the same diameter, the longest cavity was achieved using a disk cavitator and the smallest using a hemispherical one. A double-wedged cone proved to be better than conical. [15]

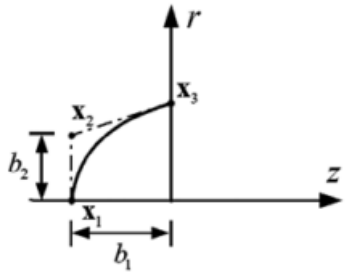

Figure 3-1 Cavitator geometrical modeling [14]

$$X(\eta) = \frac{(1-\eta)^2 X_1 \omega_1 + 2\eta(1-\eta) X_2 \omega_2 + \eta^2 X_3 \omega_3}{(1-\eta)^2 \omega_1 + 2\eta(1-\eta)\omega_2 + \eta^2 \omega_3} \qquad (3.\ 1)$$

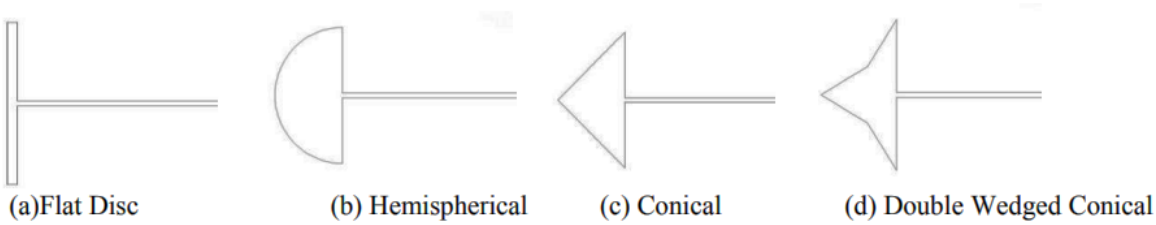

Figure 3-2 Types of cavitators used in optimization. [15]

3.2 Limiting conditions

Several shapes of cavitators from previous research will be considered for this CaviPlasma design. For this specific work the main optimization parameters are the length of the cavity, which should be long enough to surround both the high voltage electrode and the ground electrode in a gaseous environment. The cavitator itself should be designed so the losses are minimal. The minimal outlet gauge pressure is given by hydraulic losses and the technical parameters of the pressure vessel and flow rate are given by the pump and flow meter. The main dimensions and conditions that were expected of the experimental setup at the beginning of the simulations are listed in the Table 1.

Table 1 Given parameters

Name	*Label*	*Value*	*Unit*
Inner dimension of the tube	$Ød$	50	mm
Minimum distance of the electrodes	L	140	mm
Maximum Flow rate	Q	13	l/s
Minimum outlet gauge pressure	p_{omin}	-50000	Pa
Maximum outlet gauge pressure	p_{omax}	30000	Pa

Another requirement is for the cavitation to be natural i. e., without air injection to ensure low pressure inside the cavity to achieve sufficient length of the plasma discharge. Since in the future, the device will be used in combination with plasma discharge, the cavitator itself should either be made from non-conductive material or be suitably insulated. The mounting of the cavitator must be done in such a way, that the cavitating cloud behind an obstacle would not be disrupted and would allow for plasma discharge to occur in this area in between the electrodes.

All the above-mentioned limitations were considered from the start. However, during the computational modelling part of this work, simplifications were made to obtain results faster.

4 Computational modelling

The four geometries from [15], which were mentioned in chapter 3.1, were used to compare the length of cavity, losses and the force on the body using ANSYS Fluent. The geometry with the most suitable results will be then used to perform the experimental part of this work documented in chapter 5 and 6. When we neglect the ribs and mounting discussed in chapter 5.2, which will be used to increase rigidity and to safely attach the cavitator, the problem is fully axisymmetric, therefore, the geometries of the cavitator will be compared as such. This step will help to reduce number of elements used in the mesh and to reduce the computing time, but it shouldn't affect the outcomes regarding which cavitator shape will have the best required parameters.

4.1 Geometry

All geometries of the considered cavitators lower the cross-section area in the tube. The aim is to find the cavitator with the maximal length of the cavitation cloud behind the obstacle. If possible, the losses for the given shape should be possibly minimized. For the testing of shapes, a 2D axisymmetric problem was observed in Fluent. These geometries did not take into consideration the mounting which will further decrease the cross-section area, which will result in higher velocities reached in the liquid.

Main dimensions used in the 2D axisymmetric problem are shown in Figure 4-1. Default dimensions remained unchanged for every specific geometry of the cavitator. The geometry of each cavitator is then closer described in Figure 4-2 through Figure 4-5.

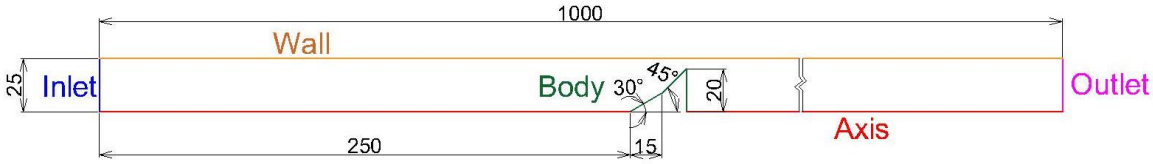

Figure 4-1 Main dimensions and boundary conditions of the 2D axisymmetric domain

Cavitator 1 - Flat disc:

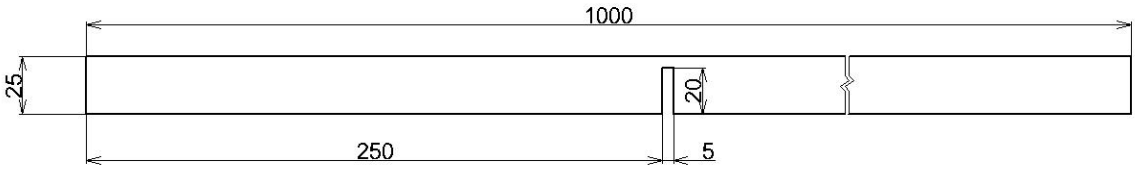

Figure 4-2 Dimensions of the flat disc geometry

Cavitator 2 – Hemispherical:

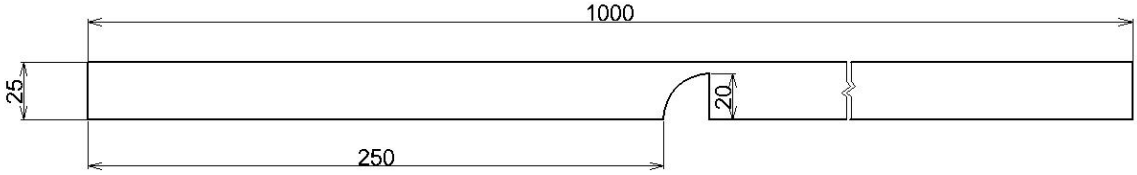

Figure 4-3 Geometry of the hemispherical cavitator

Cavitator 3 – Cone:

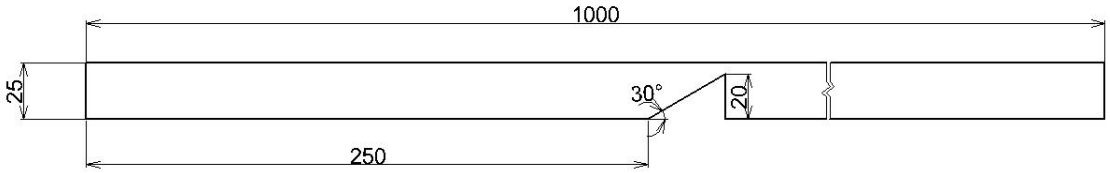

Figure 4-4 Geometry of the cone cavitator

Cavitator 4 – Double-wedged cone:

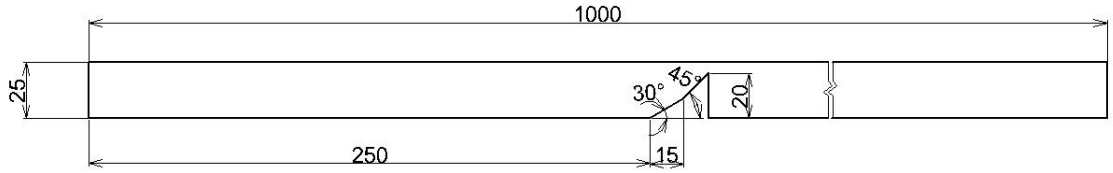

Figure 4-5 Geometry of the double-wedged cone

4.2 Mesh

The mesh was created in Workbench meshing and an example of a mesh is shown in Figure 4-6. The Multizone Quadrilateral Dominant Method was used with a free face mesh type set to all quads on the entire domain. Inflation was used to achieve the required y^+. The value of y^+ is best around 1, with a SST k-ω turbulence model. The high aspect ratio occurred due to the first layer, to obtain a sufficient y^{+}.

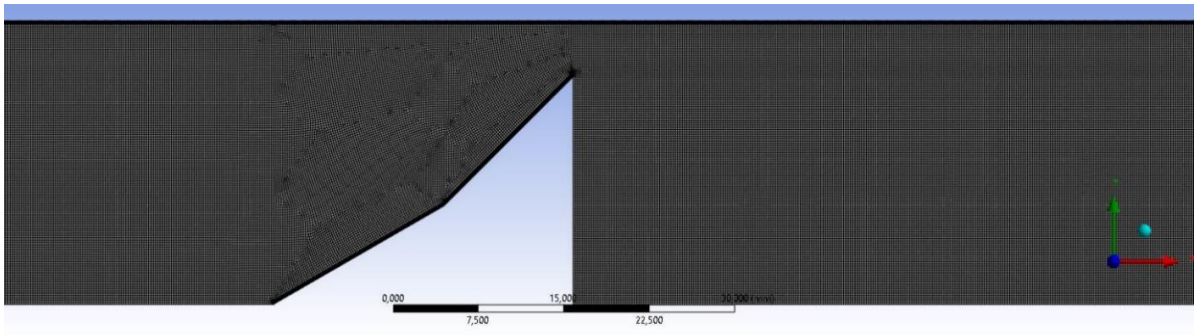

Figure 4-6 Example of a mesh

Table 2 Mesh statistics for individual cavitators

Geometry	*Number of elements*	*Max. skewness*	Max. aspect ratio	y^+
Flat disc	705 669	0,98	*241*	1,2
Hemispherical	700 441	0,95	*200*	0,8
Cone	523 020	0,88	*234*	3
Double wedged cone	543 463	0,96	*200*	1

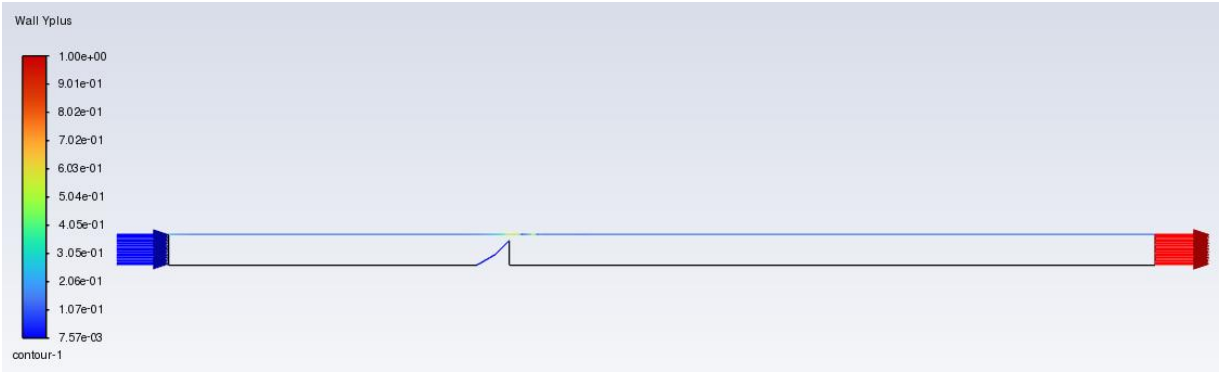

Figure 4-7 Example of rendering y+ on zones of interest

4.3 Boundary conditions

Provided Figure 4-1 illustrates boundary conditions with their name selections. Note that the geometry of the body is different for each case. Closer specification of each boundary condition:

Inlet

The velocity at the inlet was calculated based on the desired flow rate Q. The maximum flow rate, as mentioned above in Table 1 is 13 l/s, anyhow, to be on the safe side, the simulations were performed for the flow rate of 11 l/s. Subsequently, boundary conditions were established using the mean velocity $\bar{v}$. Turbulence specifications were implemented through turbulence intensity and a hydraulic diameter. The turbulence intensity value of 5% was assigned to the inlet. The hydraulic diameter of the circular cross-section is equal to the diameter of the tube $d_{in} = d_h$. The diameter on the inlet is also equal to the diameter on the outlet.

$$Q = 11\,\mathrm{l}/s = 0.011\ m^3/s$$

$$d_h = d_{in} = d_{out} = 50\ \mathrm{mm} = 0.05\ \mathrm{m}$$

$$\bar{v} = \frac{Q}{S} = \frac{4Q}{\pi d_{in}} = 5.602\ \mathrm{m/s} \qquad (4.\ 1)$$

Where:

Q	flow rate	[m^3/s]
d_{in}	inlet diameter	[m]
d_{out}	outlet diameter	[m]
d_h	hydraulic diameter	[m]
$\bar{v}$	mean velocity	[m/s]
S	inlet area	[m^2]

Outlet

The outlet boundary condition was defined as a pressure outlet. On outlet, the vacuum pump and compressor will be attached. Therefore, the outlet gauge pressure can be set from

30 000 Pa to -50 000 Pa. Turbulence settings were applied with a turbulence intensity of 10% and hydraulic diameter same as was defined on the inlet.

Wall

The wall boundary condition was applied to the body of the cavitator and the wall of the tube, as can be seen in Figure 4-1. Wall boundary conditions were assigned with a no-slip condition as stationary wall, ensuring the velocity drop to zero near the wall.

Axis

In Ansys Fluent, the term "axisymmetric" describes a domain that is symmetric about the x axis. The 2D axisymmetric form of the governing equations is solved rather than the 2D Cartesian form when the axisymmetric is enabled. The specified axis can be seen in Figure 4-1.

Material

Since the problem is solved as a multiphase (mixture), two materials had to be chosen from the Ansys database. They were 'water-liquid' as a primary material and 'water-vapor' as a secondary material.

4.4 Solver set-up

The Reynolds averaged Navier-Stokes (RANS) method is a primary tool for the cavitation simulation as it can provide satisfactory predictions at lower computational costs. The typical representatives are models k-ε, k-ω and their other formulations. The RANS closure model is based on the assumptions of equilibrium and the isotropic turbulence. The cavitation model considers the dual phase flow as a homogenous mixture. The RANS models produce excess turbulent viscosity during the computational simulations with multiphase flow and therefore supress non-stationary phenomena. This can cause significant differences in the RANS forecast for cavitating flow. This problem can be tackled by using the user defined function (UDF) described in chapter 4.6.

The SST k-ω turbulence model [Menter 1993] was chosen. The shear stress transport (SST) combines the use of the k-ω formulation in the inner parts of the boundary layers, hence it can be used as a low-Reynolds turbulence model but can automatically switch to k-ε behaviour in the free-stream. The switching is done automatically and is dependent on the critical Reynolds turbulence number. The general solver settings were configured as pressure-based. The initialisation was done using hybrid initialisation. Firstly, several hundred steps were pre calculated using steady-state flow and then the calculation was switched to transient.

4.4.1 Multiphase model [16]

There are several approaches that can be applied to the model multiphase problems. Euler models deal with the concentration of phases. Euler based models include a volume of fluid model theory, mixture model theory and eulerian model theory.

To model the multiphase flow, the mixture model theory was applied. This approach works with volume fraction which can be described as:

$$\alpha = \frac{V_v}{V} \qquad (4.\ 2)$$

Where:

α Vapor volume fraction [-]

V_v	Vapor volume	[m^3]
V	Volume	[m^3]

This volume fraction is in the range from 0 to 1, where 1 is 100% of the given phase. The mixture model can model *n* phases, in our case 2, by solving the momentum, continuity, and energy equations for the mixture.

A basic two-phase cavitation mixture model uses the standard flow equations governing the transport of the mixture. In cavitation, the mass transfer between the liquid and vapor phases is governed by the vapor transport equation:

$$\frac{\partial}{\partial t}(\alpha\rho_v) + \nabla \cdot \left(\alpha\rho_v \overrightarrow{V_v}\right) = R_e - R_c \qquad (4.\ 3)$$

Where:

ρ_v	Vapor density	[kg/m^3]
$\overrightarrow{V_v}$	Vapor phase velocity	[m/s]
R_e, R_c	Mass transfer source terms connected to the growth and collapse of the vapor bubbles respectively	
t	time	[s]

We can assume that there are plenty of nuclei for the inception of cavitation, therefore the focus is on the proper accounting of the bubble growth and collapse. In a flowing liquid with zero velocity slip between the fluid and bubbles, the bubble dynamics equation can be derived from the generalized Reyleigh-Plesset equation (4. 4). When the second-order terms and the surface tension force are neglected, we get the simplified equation (4. 5), which provides the physical approach that is necessary to introduce the effect of bubble dynamics into the cavitation model.

$$\mathcal{R}\frac{D^2\mathcal{R}}{Dt^2} + \frac{3}{2}\left(\frac{D\mathcal{R}}{Dt}\right)^2 = \left(\frac{p_B - p}{\rho_l}\right) - \frac{4v_l}{\mathcal{R}}\mathcal{R} - \frac{2S}{\rho_l\mathcal{R}} \qquad (4.\ 4)$$

Where:

$\mathcal{R}$	bubble radius	[m^3/s]
t	time	[s]
σ	Liquid surface tension coefficient	[m]
ρ_l	Liquid density	[m]
p_B	Bubble surface pressure	[m]
p	Local far-field pressure	[m/s]

$$\frac{D\mathcal{R}}{Dt} = \sqrt{\frac{2}{3}\frac{p_B - p}{\rho_l}} \qquad (4.\ 5)$$

Schnerr and Sauer Model [17]

For the Schnerr and Sauer model, the net mass source term is:

$$R = \frac{\rho_v \rho_l}{\rho} \frac{\partial \alpha}{\partial t} \tag{4. 6}$$

The general form for the vapor volume fraction is:

$$\frac{\partial}{\partial t}(\alpha \rho_v) + \nabla \cdot \left(\alpha \rho_v \overrightarrow{V_v}\right) = \frac{\rho_v \rho_l}{\rho} \frac{\partial \alpha}{\partial t} \tag{4. 7}$$

To connect the vapor volume fraction to the number of bubbles per volume of liquid, the Schnerr and Sauer model uses the expression:

$$\alpha = \frac{n_b \frac{4}{3} \pi \mathcal{R}^3}{1 + n_b \frac{4}{3} \pi \mathcal{R}^3} \tag{4. 8}$$

from the above mentioned information, we can derive the following equations for the mass transfer rate and bubble radius:

$$R = \frac{\rho_v \rho_l}{\rho} \alpha (1 - \alpha) \frac{3}{\mathcal{R}} \sqrt{\frac{2}{3} \frac{(p_v - p)}{\rho_l}} \tag{4. 9}$$

$$\mathcal{R} = \left(\frac{\alpha}{1 - \alpha} \frac{3}{4\pi} \frac{1}{n}\right)^{\frac{1}{3}} \tag{4. 10}$$

the function $f(\alpha_v, \rho_v, \rho_l) = \frac{\rho_v \rho_l}{\rho} \alpha (1 - \alpha)$ has a property at which it aproaches zero when $\alpha = 0$ and $\alpha = 1$ and reaches the maximum inbetween. In this model, there is olny one parameter which needs to be determined and that is the number of spherical bubbles per volume of liquid.

The fianl form of the equation for modeling the condensation procees is as follows:

When $p_v \geq p$

$$R_e = \frac{\rho_v \rho_l}{\rho} \alpha (1 - \alpha) \frac{3}{\mathcal{R}} \sqrt{\frac{2}{3} \frac{(p_v - p)}{\rho_l}} \tag{4. 11}$$

When $p_v \geq p$

$$R_c = \frac{\rho_v \rho_l}{\rho} \alpha (1 - \alpha) \frac{3}{\mathcal{R}} \sqrt{\frac{2}{3} \frac{(p - p_v)}{\rho_l}} \tag{4. 12}$$

4.4.2 Courant number

The Courant number is a dimensionless parameter. This number expresses, how much the information travels across the domain in time. The courant number should be lower than one, to ensure that the information doesn't skip any cell in the mesh. The Courant number helps to determine the step size needed according to the equation (4. 13), where C_{max} is dependent on the integration scheme. If the time step size is selected incorrectly, the simulation might give

nonphysical results. The graphical illustration of the meaning of the Courant number is shown in Figure 4-8. From the knowledge of the velocity and the size of the cell, the time step was calculated to be $1e-5$ second.

$$C = \frac{U\Delta t}{\Delta x} \leq C_{max} \qquad (4.\ 13)$$

Where:

C	Courant number	[-]
U	Volume fraction of water in mixture	[m/s]
Δt	Density of vapor phase	[s]
Δx	Cell length in the examined direction	[m]

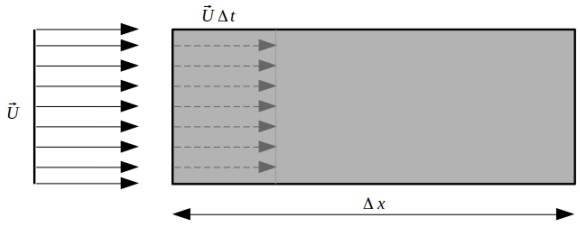

Figure 4-8 Interpretation of Courant number [18]

4.5 Conclusion of the 2D axisymmetric simulations for choice of geometry

For the length of the cavity, only the area filled with more than 90% vapor (red color in Figure 4-10 and Figure 4-11) was measured in length. The summary of the observed quantities can be seen in Table 3. The data from the simulations was obtained after the stabilization of the amount of steam in the volume as can be seen in Figure 4-9. Hydraulic losses were calculated as the difference between the total pressure on the inlet minus the total pressure on the outlet.

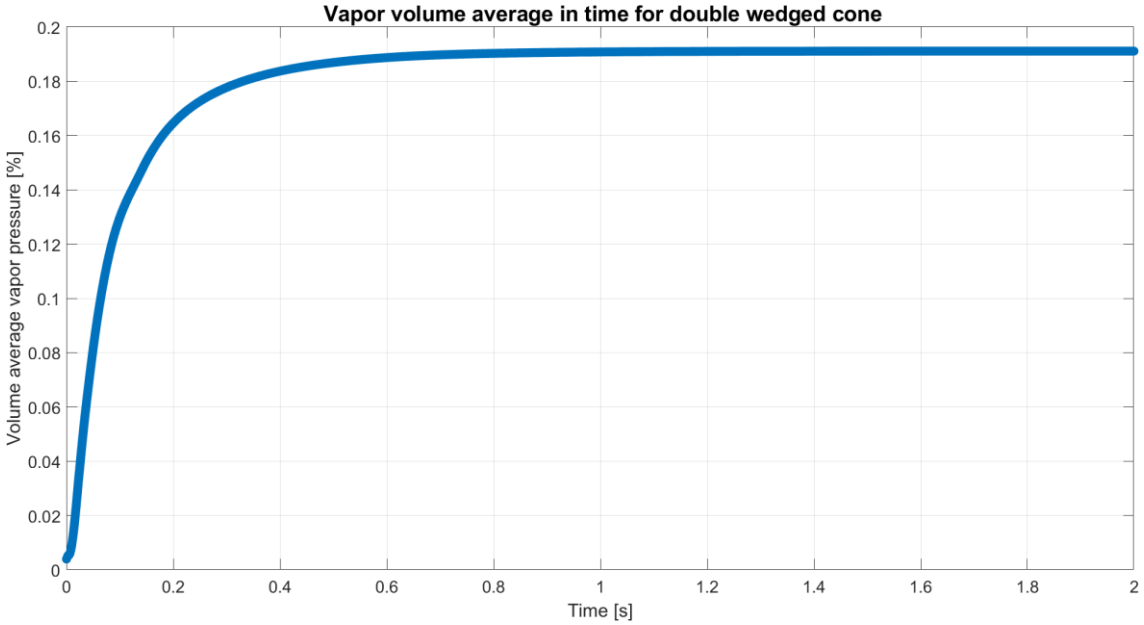

Figure 4-9 Volume average of vapor in time

Table 3 The summary of simulations for cavitators

	Length of cavity [cm]	*Inlet total pressure [Pa]*	*Outlet total pressure [Pa]*	*Hydraulic losses [Pa]*	*Force on body [N]*
Flat disc	25	205 224,2	-31 358,3	236 582,5	352
Hemispherical	-	38 905,7	-34 163,7	73 069,4	115
Conical	20	84 387,4	-28 361,4	112 748,8	175
Double-wedged cone	22,5	113 670,4	-34 258,7	147 929,1	217

The hemispherical obstacle was deemed inappropriate, since the longest the cavity gets is around 3 cm as shown in Figure 4-10 and moreover is unstable and periodically forms and vanishes. The flat disc showed the highest hydraulic losses, and the length of the cavity wasn't exceptionally larger than with the conical cavitator and the double-wedged cone cavitator. For the final choice of the geometry, the double-wedged cone was chosen. This geometry provides cavity that is bit longer, and the hydraulic losses aren't much higher. Therefore, the additional computation of the double-wedged cone with an implemented UDF was performed.

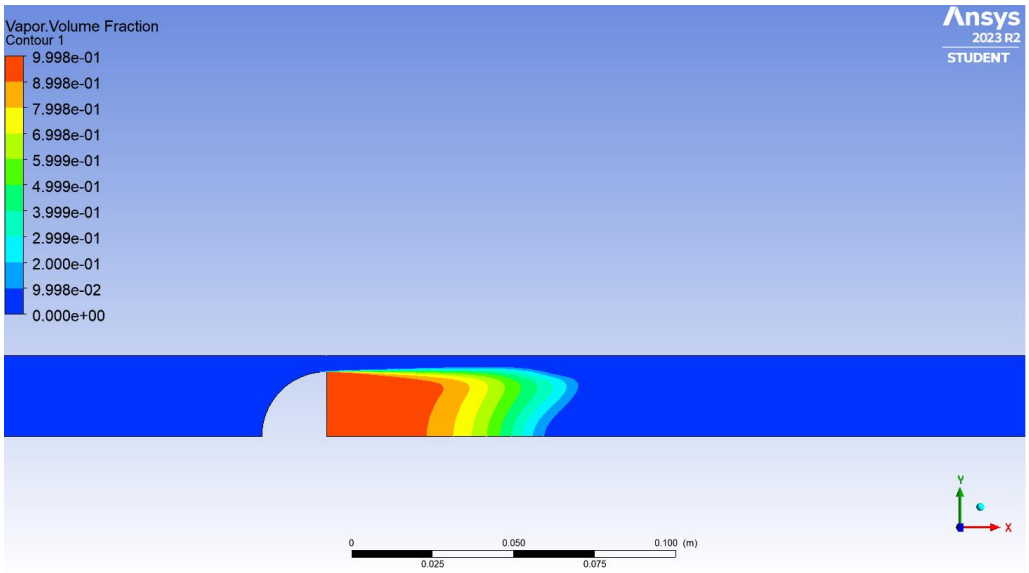

Figure 4-10 The longest cavity for a hemispherical cavitator

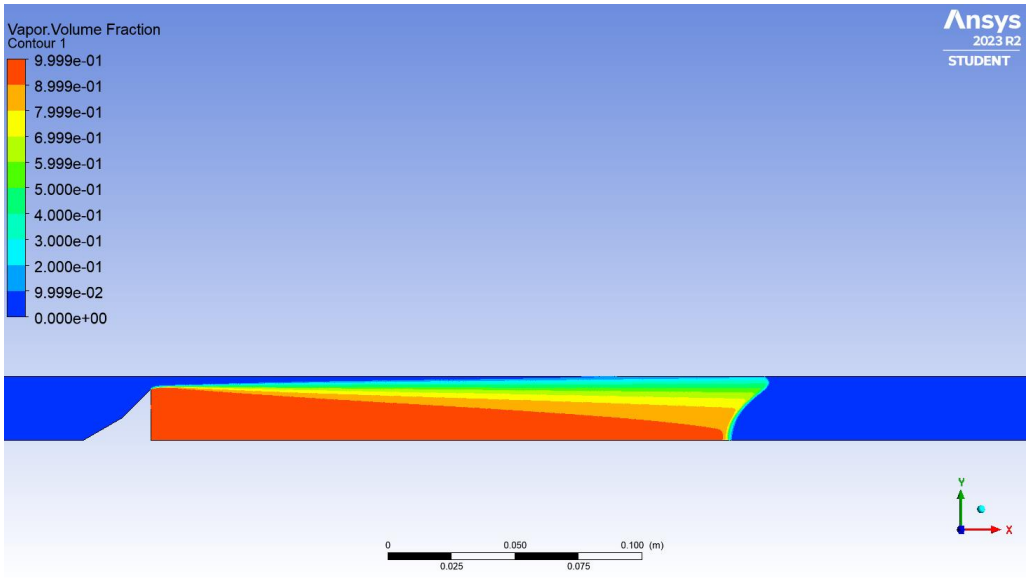

Figure 4-11 The length of the cavity for the doule-wedged coninal cavitator

4.6 User defined function (UDF)

The correction of the reboud function was suggested by *Delgosha and col.* (2003) for the k-ω and the k-ε turbulence models, which supress turbulent viscosity in the cavitation domain. The correction can be seen in Figure 4-12. The correction of the turbulent viscosity for the SST k-ω turbulence model for the implementation in UDF can be seen in equations 4-2 through 4-4. The skript of UDF itself can be seen in APPENDIX A - User defined function. [19]

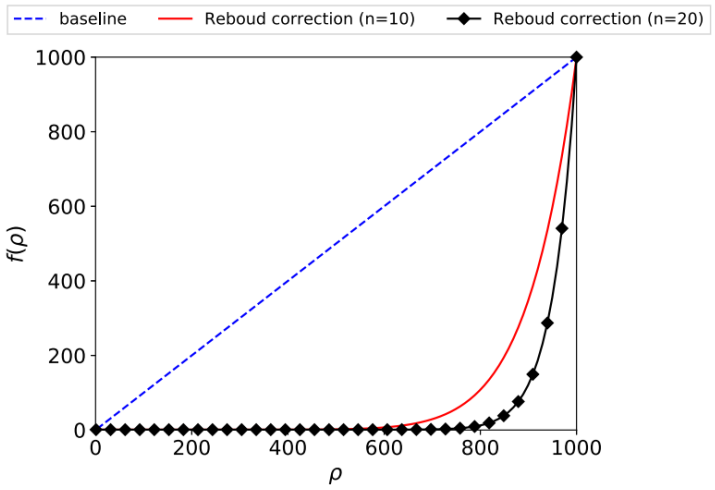

Figure 4-12 Plot of the Reboud correction function [20]

Correction $f(\rho)$ is given as [21]:

$$f(\rho) = \rho_V + \alpha^n(\rho_L - \rho_V) \qquad (4.\ 14)$$

Where:

$f(\rho)$	Reboud correction function	[kg/m^3]
α^n	Volume fraction of water in mixture	[-]
ρ_V	Density of vapor phase	[kg/m^3]

ρ_L	Density of liquid phase	[kg/m^3]
n	coefficient	[-]

Turbulent viscosity for the SST k-ω turbulence model is defined as:

$$\mu_T = \frac{\rho_S k}{\omega} \frac{1}{\max\left(\frac{1}{a^*}, \frac{SF_2}{a_1 \omega}\right)} \qquad (4.\ 15)$$

Where:

μ_T	Reboud correction function	[kg/m^3]
ρ_S	Volume fraction of water in mixture	[-]
k	Density of vapor phase	[kg/m^3]
ω	Density of liquid phase	[kg/m^3]
a^*	coefficient	[-]
S	Strain rate magnitude	[-]
F_2	Blending function	[-]

After the density ρ is replaced by $f(\rho)$ in the equation (4. 15), we get the final definition of turbulent viscosity with correction as:

$$\mu_T = \frac{f(\rho) k}{\omega} \frac{1}{\max\left(\frac{1}{a^*}, \frac{SF_2}{a_1 \omega}\right)}$$

4.7 Conclusion of the 2D axisymmetric simulations with UDF

After the implementation of UDF into ANSYS Fluent, the volume of vapor fraction increased significantly. However, as can be seen in Figure 4-13, the results are clearly physically incorrect. At first glance, the phase alongside the axis remained unchanged and after taking a closer look, it can be seen, that the cavitation arises also at the wall of the tube. These problems were tackled by trying a few different meshes, but no improvement was observed. Therefore it was concluded that the 2D axisymmetric calculation is not suitable for this kind of problem and in the future, use of a 3D simulation is recommended.

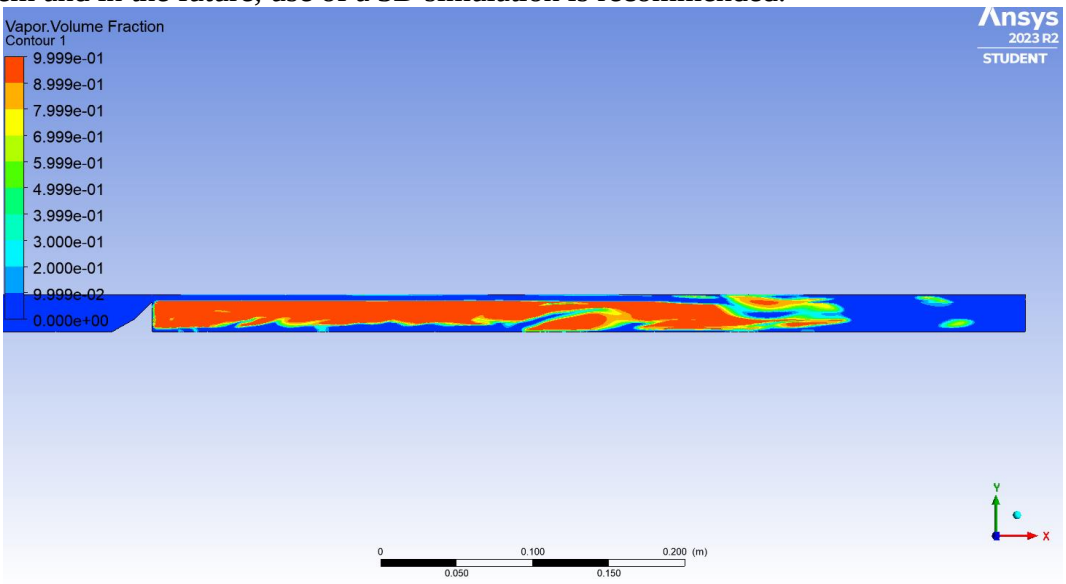

Figure 4-13 Simulation of double-wedged cone with implemented UDF

5 Experimental setup

In order to perform the experiment, it was first necessary to make a 3D model of the cavitator with the design of the attachment, to select the material from which it will be made and to manufacture it. Several types of cavitators with different attachment methods were created for the production, which were subsequently tested with static tests for loads up to 400 N to ensure that the cavitator could withstand the 217 N load based on the simulations. Subsequently, the circuit itself had to be assembled. The circuit was assembled by the staff of Viktor Kaplan's Fluid Engineering Department laboratory and then the circuit was fitted with the individual sensors.

From the chosen geometry, which was designed for a diameter of 40 mm, four more 3D prints with various diameters were made. The measured diameters of the cavitator were 22,9 mm, 38 mm, 40 mm, 42 mm, and 45,8 mm. With the cavitator with a 22,9 mm diameter, the cavitation wasn't observed for overpressures in the pressure vessel and with the underpressure, the cavitation occurred in the tube connections upstream from the cavitator, therefore the data from this experiment weren't processed. For the cavitator of the diameter 45,8 mm, the cavitator didn't withstand the forces acting upon it during the first few measurements and broke, therefore, there is very little data, and they weren't processed.

The cavitators with diameters of 38 mm, 40 mm and 42 mm were measured in two configurations. The first one was as they were designed, with water flowing on the nose of the cone, for the second one they were reversed, which can mimic the disc cavitator. Data evaluated for the second regime are marked as 'reversed' so it can be easily distinguished. Therefore, there are six geometries in total: 38 mm, 38 mm reversed, 40 mm, 40 mm reversed, 42 mm and 42 mm reversed.

5.1 Material of the cavitator

The choice of material is very important in any engineering application. In this case, the choice is greatly affected by price, time of manufacturing and the fact, that in the future, the discharge electrode should be located closely behind the cavitator. For this reason, only the non-conductive materials are considered for testing. For this reason, the plastic will be used for experiments. Plastic is cheap, easy to shape and is non-conductive. However, in the future, the degradation of plastic in the flow should be considered and looked at closely, to ensure the best possible outcome of water quality.

5.2 Mounting of the cavitator

Proper mounting of the cavitator will also be crucial. The attachment of the cavitator to the centre of the cross section is possible by either fixing it to the walls of the tube using ribs or by simply attaching it to the electrode. From previous experience with CaviPlasma in the design of the convergent-divergent nozzle, the simple attaching of the cavitator to the electrode without any other mounting will not be tested, since in higher flow rates the electrode itself tended to oscillate. Therefore, attachment of the cavitator to the walls by means of supports will be considered. These supports should generate as little loss as possible, should occupy as little flow area as possible, but at the same time should give the design sufficient operational rigidity. Mounting on a rod behind the cavitator (as can be seen in Figure 3-2) can't be used, since the area downstream from the cavitator must remain empty to later allow for the cold plasma discharge to occur between electrodes.

Several ways of mounting were tested, firstly by static load tests. The types of mounting can be seen in Figure 5-1. For the 3D print in the middle, the dimples were pre-printed and later

it was drilled. These types of mounting were then printed using fused deposition modelling (FDM). During the static load tests, two types of filaments were compared. The materials were PLA and PETG. The PLA and PETG materials were printed using 100 % infill.

A sketch of the proposed mountings that were printed using the 3D FDM printer can be seen in Figure 5-1. In Figure 5-2 the printed cavitators from PLA plastic can be seen with various types of proposed mountings. The static load tests were done on a scale with a maximum range of 50 kg. All types of mountings passed the test, howerer some very small cracks were visible on mounting number 3 from Figure 5-2. Mounting number 3 tested with material PETG was successful and no crack or cracking sound was observed during the test.

After thorough consideration mounting number 3 was chosen. Mounting number 1 was deemed inappropriate, since the insulation on the tube could be problematic. The mounting number 3 is the geometry which is the easiest one to center inside a tube, therefore it was deemed as the most appropriate geometry.

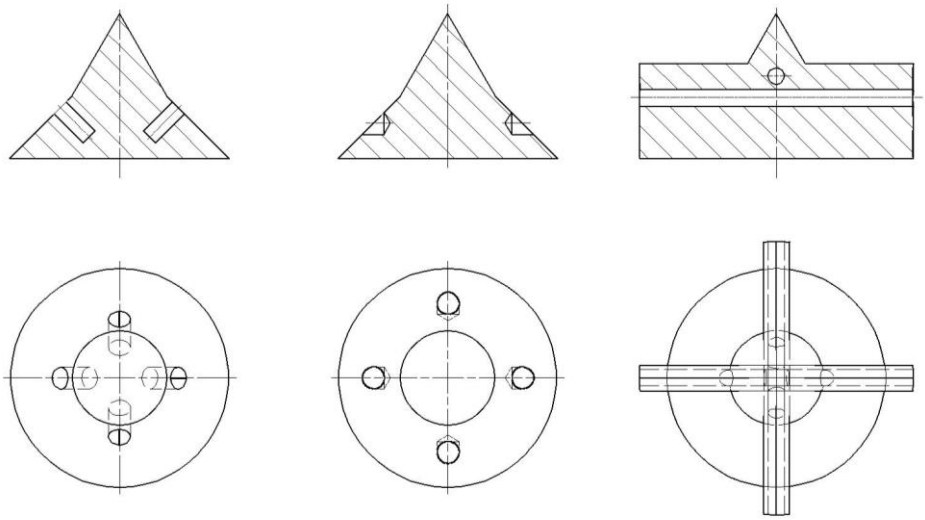

Figure 5-1 Sketches of 3D prints for mounting testing

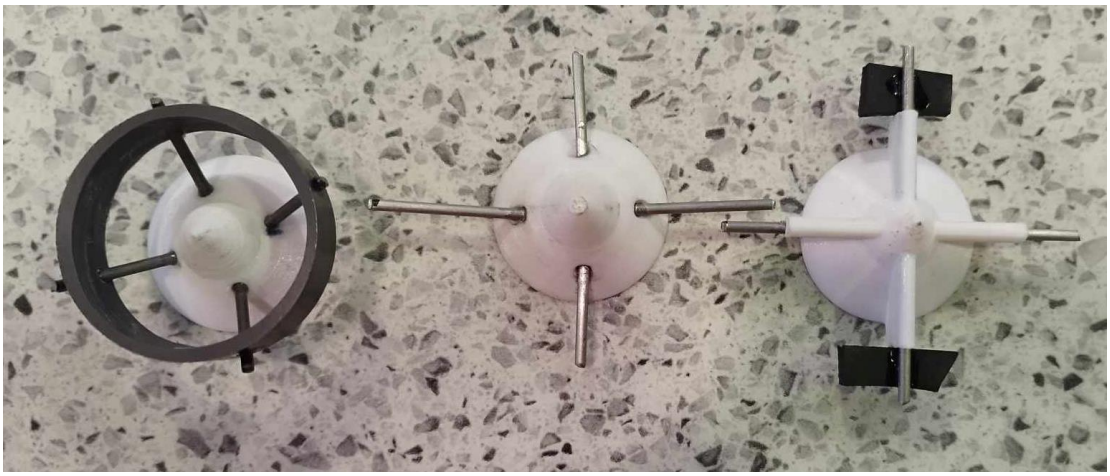

Figure 5-2 Tested mountings

5.3 Experimental circuit

The experimental setup consists of the circuit itself, pressure vessel, cavitator and its mounting, pump, sensors, a camera for flow visualisation and a light to visualise. Unfortunately, the length of the light limited the length of the frames for camera recording.

- The flow is ensured by ISH pump 125-100-NHG-400-22-ZC-020-09 pump with a power of 21,5 kW, powered by a SIEMENS motor, specifications of the pump and motor can be seen in Appendix B. Two of these pumps are available for the circuit and can be run one at a time, together in series or as a parallel.
- Flow measurement is provided by an electromagnetic flow meter Ela-Brno, type MQI 99-SN, range 20 l/s, accuracy class 0,3% from the measured value for range 10-100%, marked as 'Q' in Figure 5-3.
- The pressure p_1 at upstram of the cavitator is measured by an absolute pressure sensor BD Sensors, type DMP331, range 10 bar, absolute, accuracy class 0,25% from range.
- Four same pressure sensors p_2 to p_5 located at downstream of the cavitator are measure pressure by an absolute pressure sensor BD Sensors, type DMP331, range 6 bar, absolute, accuracy class 0,25% from range.
- The temperature in the pressure vessel marked as ‚T' in Figure 5-3 is measured using a RAWET, type PTP55, range -5°C to 50°C, accuracy class 0,3% from range.
- Acoustic emission sensor DAKEL, MDK13-AS, 30dB, marked as 'AE' in Figure 5-3.
- Acoustic emission amplifier DAKEL, frequency range 50 Hz – 50 kHz, voltage output.
- Voltage measurement cards NI 9215 and NI 9222, located in ethernet bus NI cDAQ 9185, fast channels measured using metering station NI PXIe-1078, measuring card for IEPE NI PXIe-4492.

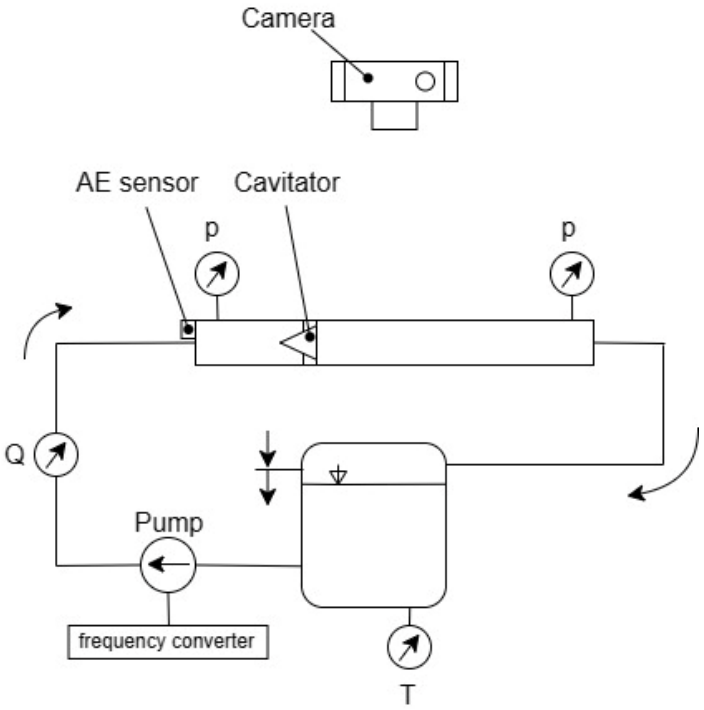

Figure 5-3 Schematic sketch of the setup

The pressure vessel can operate as open to atmosphere, connected to overpressure, or using vacuum pump with vaacuum to up to -50 kPa. Large enough vessel allows for separation of air from water, dissipation of pressure impulses and helps regulate the temperature inside a circuit. The low flow rates weren't accessible by only lowering frequency, therefor a bypass branch was used. To be able to visualise the flow, the cavitator must be mounted inside a see-through pipe component. The length of this component was chosen to be 1 m, with 25 cm length before the cavitator. The see-through pipe component is from acrylic glass and has inner diameter of 50 mm. The mounting must be sealed properly, to prevent lecage, or worse intake of air, which would lead to ventilated cavitation. During the experiments, some lecages were observed, but to prevent the intake of the air caused by low pressure, the body sealant shown in the Figure 5-4 was applied from the outer part of the tube, as seen in Figure 5-5. The schematic sketch of the setup can be seen in Figure 5-3 and photo of the real circuit is shown is Figure 5-6.

Figure 5-4 Body sealant used to prevent air intake in underpressures

Figure 5-5 Cavitator in water with body sealant applied on the outside of screw connection

Figure 5-6 Experimental setup in real life

6 Data processing

Measured data itself don't offer enough information to draw conclusions from them. For this reason, the data needs to be processed. The main goal during this data processing is to obtain dependency of loss coefficient on cavitation number. For this dependency, the error of measurement must be calculated, to determine the difference between a measured value and its amount of inaccuracy. Another very important outcome of this work is dependency of hydraulic performance on cavitation number. This information will help with comparison of this method with other types of cavitation induction. Another very important dependency is that of cavitation number on length of the cavity.

Apart from hydraulic characteristics, the signals from sensor of acoustic emission and pressure sensor downstream of the cavitator were processed. The signal for acoustic emission was processed using fast Fourier transform and root-mean-square value. The signal from pressure sensor was processed using fast Fourier transform.

All the data processing in this chapter was done using MATLAB software. Part of this work was also writing of the code for data processing.

6.1 Hydraulic characteristics

The knowledge of hydraulic characteristics leads to better understanding of behaviour of cavitators and in future will aid with choice of an optimal design of the CaviPlasma device. To measure the characteristics, the closed circuit was used to measure pressure differences before and behind cavitator and the flow rate. The characteristics were developed based on the calculated loss coefficient ξ and the cavitation number σ.

6.1.1 Measurement procedure

Measurements were conducted for the three diameters (38 mm, 40 mm, and 42 mm) of chosen double-wedged cone cavitator. Flow parameters were adjusted by changing the pressure in the pressure vessel, in the range of 30 000 Pa to -50 000 Pa of relative pressure. Flow parameters were also adjusted by a frequency converter connected to the pump motor. The minimum flow rate was 2 l/s and the maximum flow rate was 13 l/s. Each operating point was set by always changing only one of the parameters (pressure or flow rate). During the measurement, the temperature of the system was monitored. It was monitored, that the temperature never exceeded 30 °C, as the vapor pressure alongside the density are temperature dependent.

6.1.2 Evaluation procedure

To evaluate the data the procedure was followed. Firstly, the data were measured as setting the specific operating point according to above-described measurement procedure. The measured values were allowed to stabilize before recording them. The provided sampling frequency of 2 000 samples per second for pressure sensors, thermometer, and flow rate meter. A 30 second data set was saved for the specific operating point. If the inception of cavitation or supercavitation was observed, the data set was specifically marked to later distinguish it from the rest. After the data set was saved another operating point was set, until all the operating points were measured.

The data set with inception of cavitation was marked, when the first bubbles forming were visible with naked eye. However, this initial mode of cavitation was not visible with the high-speed camera. The data set was marked as one with supercavitation, when formation of first continuous volume of vapor was visible. This regime was however harder to distinguish, as the continuous cavity could have been formed a bit sooner but wasn't visible through cloud of bubbles surrounding it. An example of supercavitation is shown in Figure 6-1. The inside of the cloud is forming a continuous region; however, it is surrounded by individual bubbles.

After the supercavitation occurs, the length of cavity increases rapidly. For this reason, only several supercavitation regimes were evaluated, as for most of them, the cavity was so long, it affected the pressure sensor downstream of the cavitator. For this experiment, four pressure sensors were located downstream of the obstacle. First three pressure sensors were spaced 10 cm apart. The fourth sensor was placed approximately 80 cm doenstream. If the experiment was to be repeated in the future, the length of the tube should be much longer, and the pressure sensors should be placed further apart, with the last sensor at least 150 cm from the cavitator.

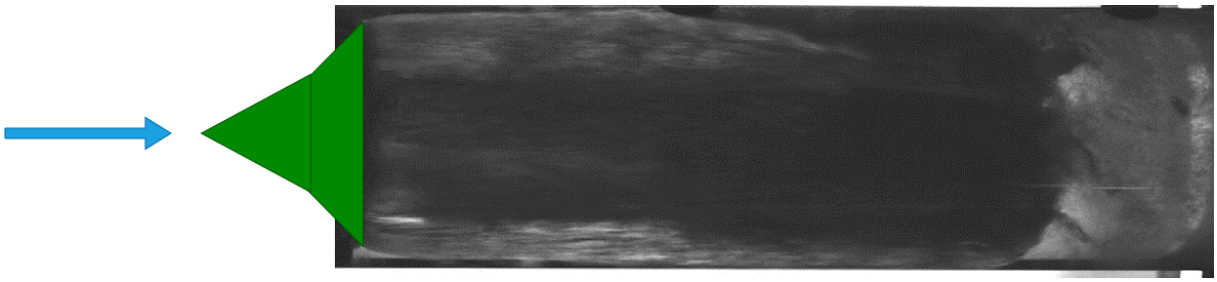

Figure 6-1 Start of supercavitation with cavitator and flow direction indicated

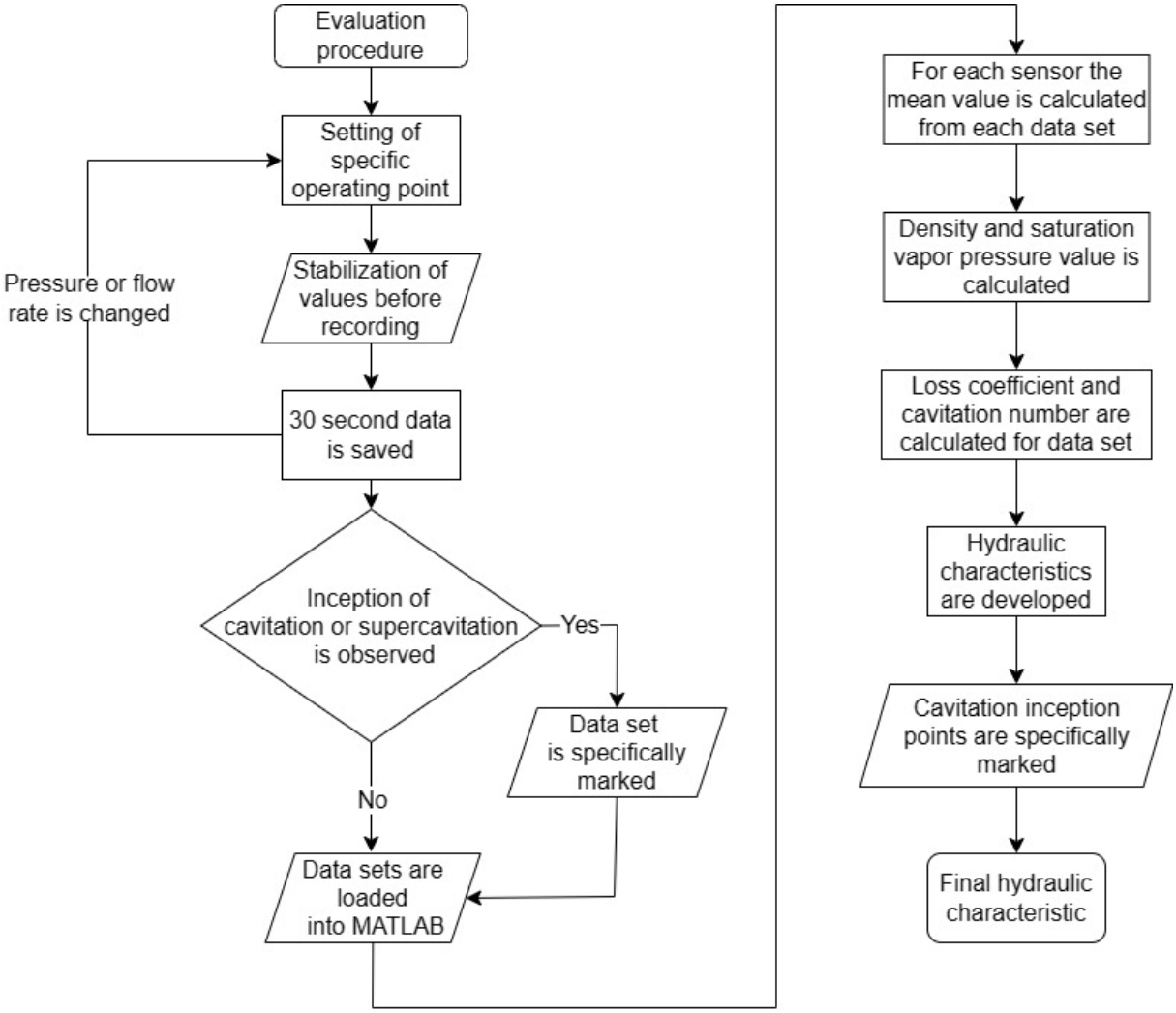

Figure 6-2 Diagram of data evaluation process

After all the data were recorded, they were loaded into MATLAB software. From each data set, specific to each operating point, the mean values were calculated for each sensor. The density value and the saturation vapor pressure value were determined based on empirical formulas in (6. 1) [22] and (6. 2) [23] as function of temperature. Afterwards, the cavitation number σ, which characterizes the cavitation flow was calculated according to (6. 3). Loss coefficient ξ, which characterizes the degree of hydraulic losses was calculated according to (6. 6) and (6. 7). For the calculation of cavitation number, the average flow velocity in the smallest cross-section v_n was calculated according to (6. 4), where S_n is the cross-section area. The cross-section area was calculated for each diameter of cavitator using Autodesk Inventor, to take into consideration the area of the mounting at the maximum diameter of cavitator. The area of one quarter of the cross-section for the cavitator diameter of 38 mm can be seen in Figure 6-3. The evaluation process is described in the diagram in Figure 6-2.

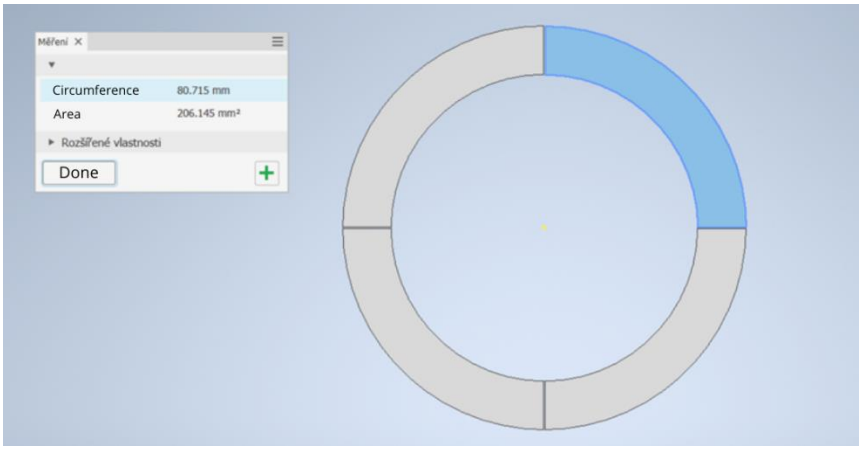

Figure 6-3 Calculation of one quarter of the cross-section area

$$\rho = \frac{999{,}83952 + at + bt^2 + ct^3 + dt^4 + et^5}{1 + ft} \qquad (6.\ 1)$$

Where:

ρ	Water density	[kg/m^3]
a, b, c, d, e, f	Constants	[-]
t	Temperature	[°C]

$$a = 16{,}945176$$
$$b = -7{,}9870401 \cdot 10^{-3}$$
$$c = -46{,}17041 \cdot 10^{-6}$$
$$d = 105{,}56302 \cdot 10^{-9}$$
$$e = -280{,}54253 \cdot 10^{-12}$$
$$f = 16{,}897850 \cdot 10^{-3}$$

$$p_v = 610{,}94 e^{\frac{17{,}625t}{t+248{,}04}} \qquad (6.\ 2)$$

Where:

p_v	Vapour pressure	[Pa]
t	Temperature	[°C]

$$\sigma = \frac{p_2 - p_v}{\rho \frac{v_n^2}{2}} \quad (6.\ 3)$$

Where:

p_2	Pressure downstream of the cavity	[Pa]
p_v	Vapour pressure	[Pa]
ρ	Temperature	[kg/m^3]
v_n	Average flow velocity	[m/s]

$$v_n = \frac{Q}{S_n} \quad (6.\ 4)$$

Where:

Q	Flow rate	[m^3/s]
S_n	Cross-section area at the maximum diameter of the cavitator	[m^2]

The calculation of loss coefficient can be obtained from Bernoulli equation for the domain shown in Figure 6-4. The Bernoulli equation is as follows:

$$\frac{p_1}{\rho} + \frac{v_1^2}{2} + g h_1 = \frac{p_2}{\rho} + \frac{v_2^2}{2} + g h_2 + \xi \frac{v_n^2}{2} \quad (6.\ 5)$$

Where:

g	Standard acceleration of gravity	[m/s^2]
p_1, p_2	Pressures from pressure sensors upstream and downstream respectfully	[Pa]
v_1, v_2	Velocities upstream and downstream respectfully	[m/s]
v_n	Average flow velocity	[m/s]
h_1, h_2	Reference height	[m]
ξ	Loss coefficient	[-]

For this case $h_1 = h_2$. The velocities can be calculated as velocity v_n for corresponding areas. If we consider, that area of the tube downstream and upstream of the cavitator are the same, therefore $v_1 = v_2$, the final equation for calculation of loss coefficient:

$$\xi = \frac{p_1 - p_2}{\rho \frac{v_n^2}{2}} \quad (6.\ 6)$$

When we include the correction on static pressure (where $Q = 0$) into equation (6. 6), we get:

$$\xi = \frac{p_1 - p_2 - p_s}{\rho \frac{v_n^2}{2}}$$

Where:

p_s	Static pressure	[Pa]

The static pressure can be calculated as:

$$p_s = p_{1s} - p_{2s}$$

Where:

p_{1s}, p_{2s}	Static pressures from pressure sensors upstream and downstream respectfully	[Pa]

In the experiment, this equation was used for calculation of loss coefficient for doble-wedged cone with diameter of 38 mm, as the pressure sensor downstream of the cavitator was mounted on the same tube as the pressure sensor upstream of the cavitator. However, for larger diameters and all reversed geometries, the evaluation was done from pressure sensor further downstream. This pressure sensor was mounted on the tube with inner diameter $\emptyset d = 53{,}6$ mm, which is slightly different of that made of plexiglass. For the case, where $v_1 \neq v_2$, the calculation of loss coefficient was calculated as:

$$\xi = \frac{(p_1 - p_2 - p_s) - \left(\rho \frac{v_1^2}{2} - \rho \frac{v_2^2}{2}\right)}{\rho \frac{v_n^2}{2}} \qquad (6.\ 7)$$

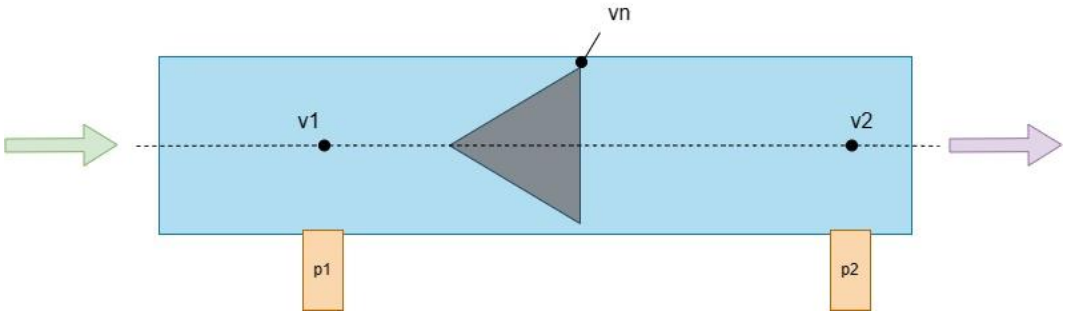

Figure 6-4 Sample domain

6.1.3 Calculation of error of measurement [24]

In order to determine with what accuracy the measurements of the cavitator were done we need to calculate the error of measurement. The error of measurement is parameter related to measurement result and it characterizes the range of values, which can be rationally assign to measured quantity. The final error of measurement consists of several partial errors of measurement. In order to determine the final error of measuremnt two partioal errors are possible: error of measurement type A, which is a statistical evaluation of measured data and

error of measurement type B, which covers other form of error than statistical evaluation of measured data. In this work, the error of measurement type A wasn't calculated as it can be neglected. And the total error was calculated using only type B.

Error of measurement type A

Type A error of measurement is evaluated for control measurements, where each point needs to be measured several times. For our case the error of measurement type A is calculated as standard deviaton of data set that was measured throughout 30 second time span witn sampling frequency of 1 000 samples per second. The errors were calculated for cavitation number σ and loss coeficient ξ. From measured data the mean value was calculated for each measured point as:

$$\bar{x} = \frac{1}{N}\sum_{i=1}^{N} x_i \qquad (6.\ 8)$$

Where:

$\bar{x}$	Arithmetic mean
N	Number of measured values
x_i	Measured values

Then the standard deviation u_A can be determined using equation:

$$u_A = \sqrt{\frac{1}{N(N-1)}\sum_{i=1}^{N}(x_i - \bar{x})^2} \qquad (6.\ 9)$$

Where:

$\bar{x}$	Arithmetic mean
N	Number of measured values
x_i	Measured values
u_A	Standard error of measurement type A

Error of measurement type B [25]

The type B error of measurement is calculated from the inaccuracy of measuring equipment. The final error of measurement type B can be calculated according to equation (6. 10).

$$u_B = \sqrt{\sum_{j=1}^{p} A_j^2 u_{Bzj}^2} \qquad (6.\ 10)$$

Where:

u_B	Standard error of measurement type B

A_j Sensitivity coefficient

u_{Bzj} Uncertainties of individual sources

And sensitivity coefficient can be calculated as:

$$A_j = \frac{\partial y}{\partial x_i} = \frac{\partial f(x_1,\ x_2, \dots\ x_i, \dots x_m)}{\partial x_i} \qquad (6.\ 11)$$

Where:

y Function

x_i The relevant input quantity

Firstly the error for measuring equipment needs to be calculated, for both pressure sensors and flow meter:

$$u_{Bp_1} = 2500$$
$$u_{Bp_2} = 1500$$
$$u_{BQ} = 0{,}00006$$

The error of measurement for cavitation number σ is:

$$u_{B\sigma} = \sqrt{\left(\frac{\partial \sigma}{\partial p_2} u_{Bp_2}\right)^2 + \left(\frac{\partial \sigma}{\partial Q} u_{BQ}\right)^2}$$

$$u_{B\sigma} = \sqrt{\left(\frac{2S^2}{Q^2\rho} u_{Bp_2}\right)^2 + \left(\frac{4S^2(p_v - p_2)}{\rho Q^3} u_{BQ}\right)^2}$$

The error of measurement for loss coefficient ξ is:

$$u_{B\xi} = \sqrt{\left(\frac{\partial \xi}{\partial p_2} u_{Bp_1}\right)^2 + \left(\frac{\partial \xi}{\partial p_2} u_{Bp_2}\right)^2 + \left(\frac{\partial \xi}{\partial Q} u_{BQ}\right)^2}$$

$$u_{B\xi} = \sqrt{\left(\frac{2S^2}{Q^2\rho} u_{Bp_1}\right)^2 + \left(-\frac{2S^2}{Q^2\rho} u_{Bp_2}\right)^2 + \left(-\frac{4(p_1 - p_2)S^2}{\rho Q^3} u_{BQ}\right)^2}$$

Final error of measurement

The final error of measurement can be calculated according to equation (6. 12), however the values of the standard deviation are very small and are neglected when calculating the absolute error of measurement and only error of measurement type B is considered.

$$u_c = \sqrt{u_A^2 + u_B^2} \qquad (6.\ 12)$$

6.1.4 Final hydraulic characteristics

During this work, six geometries were experimentally measured, and each geometry contained 9 characteristics. All the characteristics are shown in APPENDIX C - Hydraulic characteristics. In Figure 6-5 is an example of a characteristic for an obstacle with diameter of 38 mm and underpressure of 40 kPa. In the example and in all characteristics, after the inception of cavitation, with lowering cavitation number, the loss coefficient drops. The drop is most likely caused by decrease in friction,when the body is surrounded by bubbles. In this case it can be observed, that after the supercavitation occurs, the loss coefficient grows.

In figures, where the dependency is plotted on cavitation number, the inception of cavitation and beginning of supercavitation are marked. For the plots in this chapter, where the plots are done for one diameter and one specific pressure, the markers of cavitation inception and start of supercavitation are the values for specific points. For cases, where the dependencies are plotted for more than one pressure, the values of markers for inception of cavitation and start of supercavitation are calculated as average from points with inception of cavitation for different pressures or as average of values marked as start of supercavitation for different pressures.

In the example characteristic in Figure 6-5 it appears, that in the non-cavitation regime, with lowering cavitation number, the loss coefficient increases. This is not necessarily true. In Figure 6-6 the same characteristic is drawn out but with the calculated errors of measurement. For the low flow rates (high cavitation numbers) the error is extremely large. This is because the pressure difference between the pressure sensors is at the limit of the sensor's accuracy. It is therefore assumed that the loss coefficient is constant for the cavitation-free regime. In Figure 6-7 the errorbars of characteristics for body with maximum diameter of 40 mm is depicted. The losses in this cease are still relativley large, especially in the non-cavitation regime. All plots of errorbars can be seen in APPENDIX D - Errorbar for hydraulic characteristics.

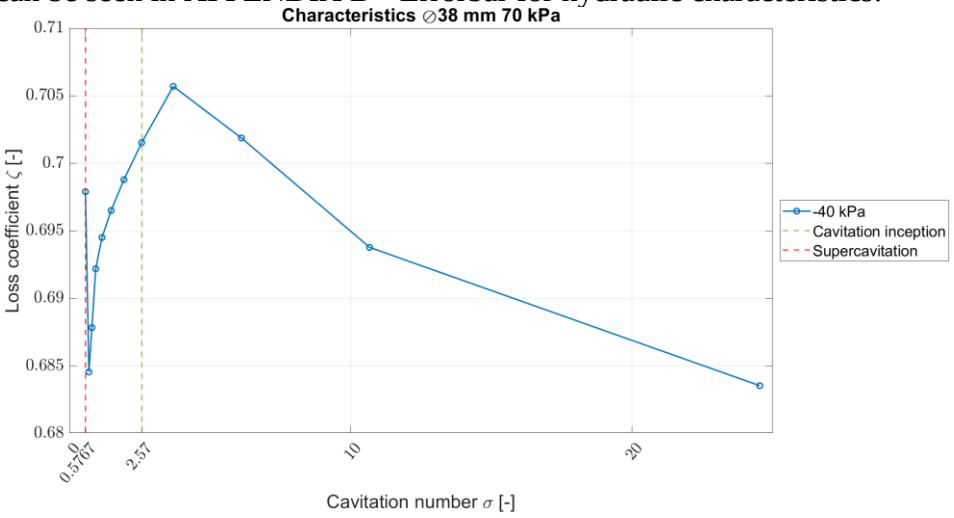

Figure 6-5 Hydraulic characteristic 38 mm -40 kPa

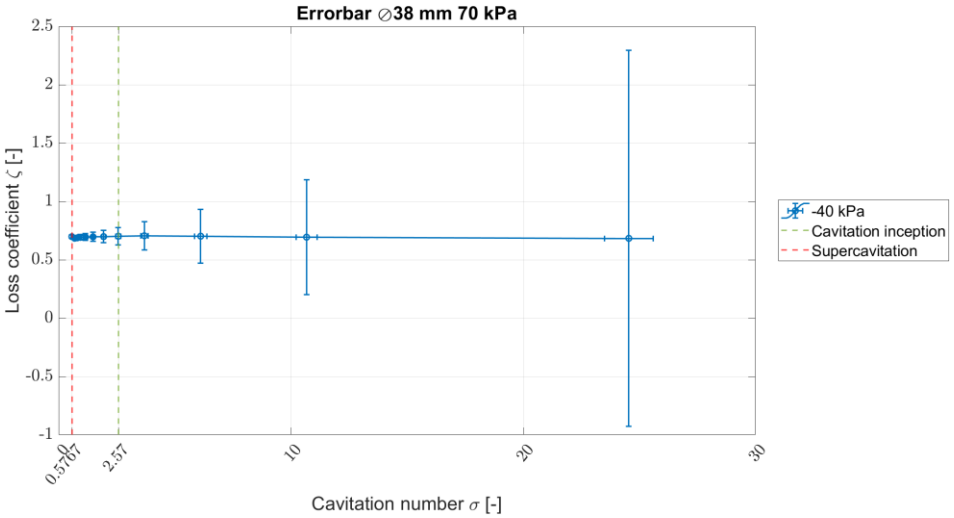

Figure 6-6 Errorbar of hydraulic characteristic 38 mm -40 kPa

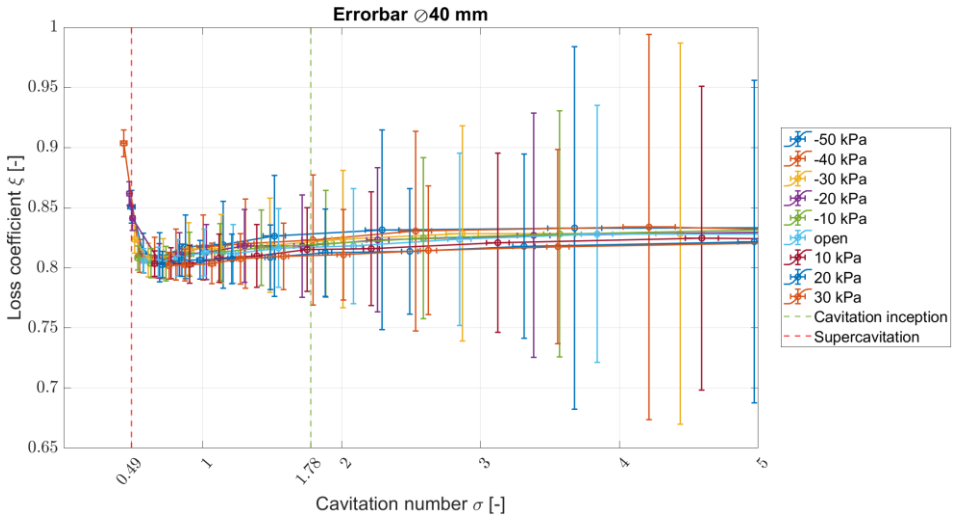

Figure 6-7 Errorbar for characteristics of cavitator with diameter of 40 mm

Figure 6-8 depicts the length of cavity on cavitation number. The length of cavity was measured by hand using measuring tape. The length of cavity for first four points after inception of cavitation was considered as 0. In Figure 6-9, for flow rate 8 l/s and 9 l/s, the cloud isnt't formed and only few bubbles appear. Dependencies for all cavitators can be found in APPENDIX E - Length of cavity on cavitation number. In Figure 6-9 the visualisation of cavitation for cavitator with maximum diameter of 38 mm and gauge pressure of -40 kPa is shown. The cavitation inception was observed with naked eye from flow rate of 7 l/s, but for this flow rate, tha cavitation was not visible for the high-speed camera.

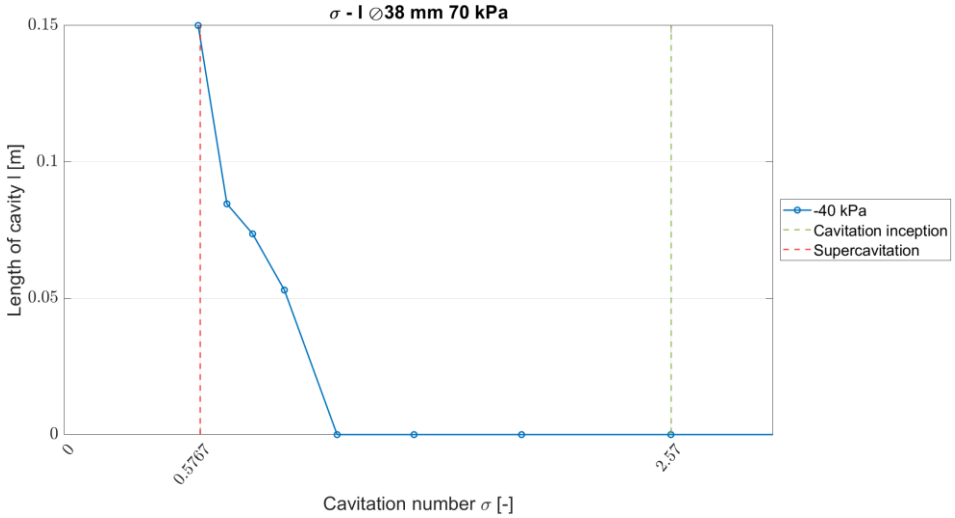

Figure 6-8 Length of cavity on cavitation number 38 mm -40 kPa

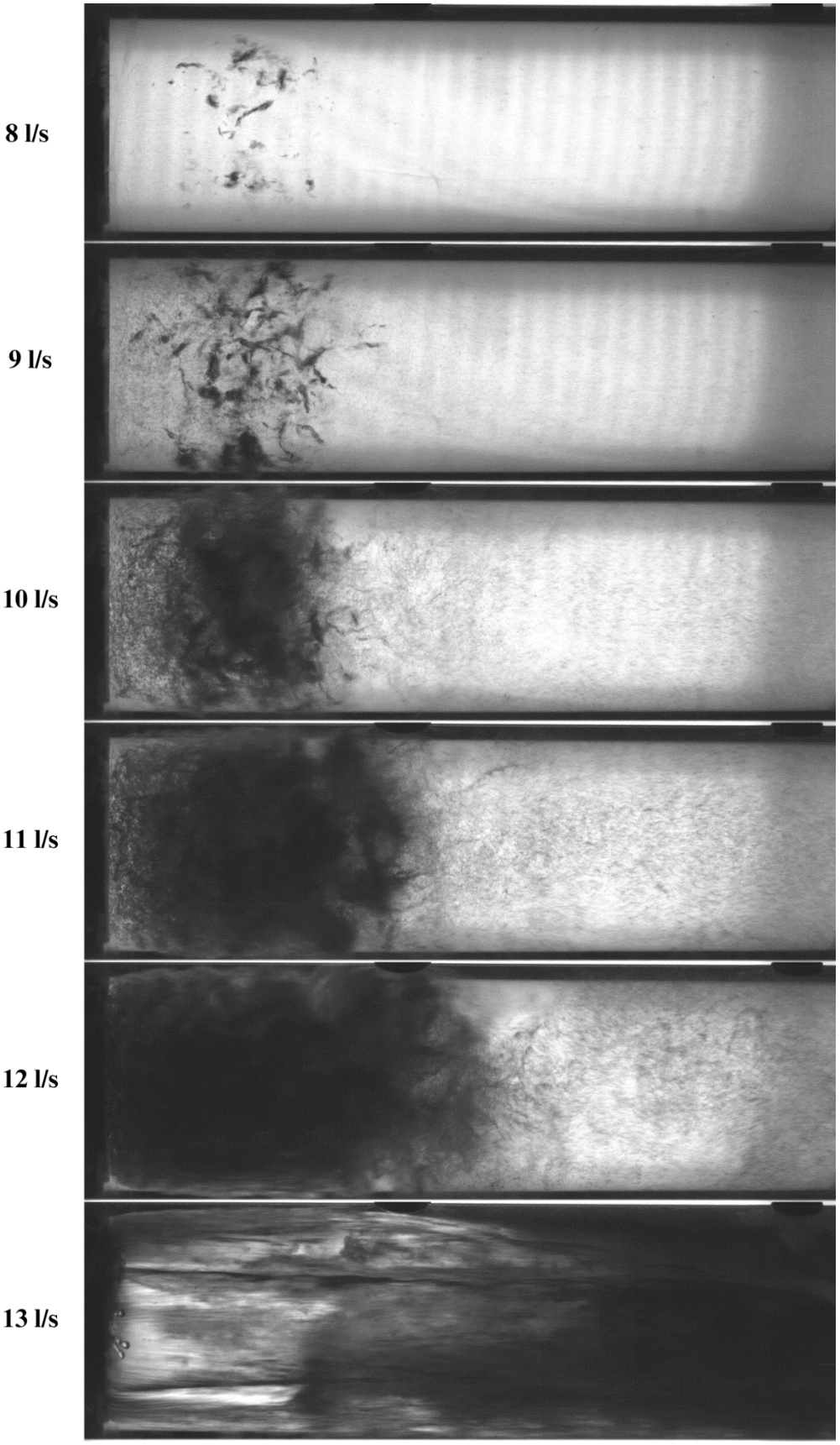

Figure 6-9 Visualisation of cavitation behind an obstacle for flow rates from 8 l/s to 13 l/s for cavitator of diameter 38 mm pressure inside vessel -40 kPa

Figure 6-10 shows dependency of pressure difference on cavitation number. Pressure difference is later used to calculate hydraulic performance, as is shown in equation (6. 13). The plots for all geometries can be found in APPENDIX F - Pressure difference on cavitation number

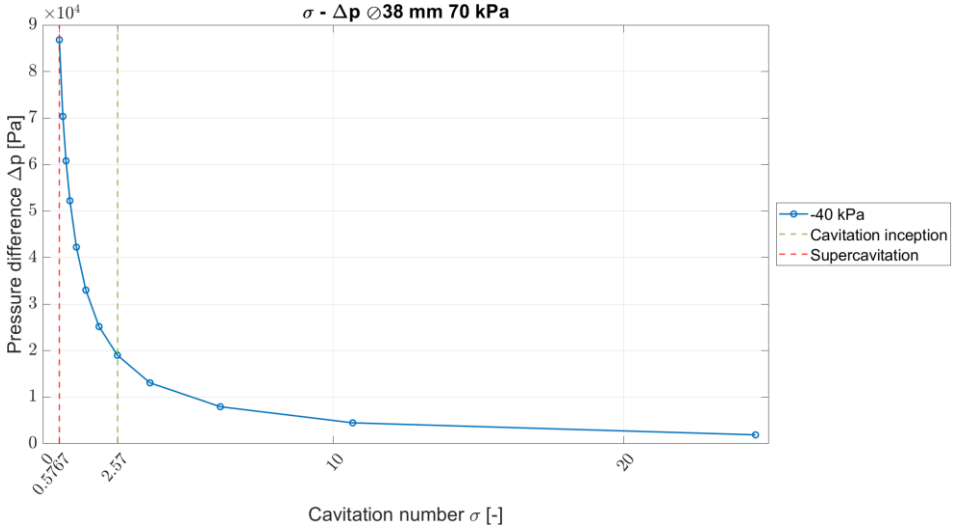

Figure 6-10 Dependancy of pressure diffrence on cavitation number for cavitator of diameter 38 mm -40 kPa

Another important parameter, which will be used for comparison with other methods of inducing cavitation is hydraulic performance, which can be calculated as:

$$P_h = \Delta p Q \qquad (6.\ 13)$$

In Figure 6-11 the dependency of hydraulic performance on cavitation nuber is shown. It can be seen, that after the inception of cavitation, the hydraulic performance grows rapidly. All other dependancies of hydraulic performance on cavitation number are shown in APPENDIX G - Hydraulic performance on cavitation number.

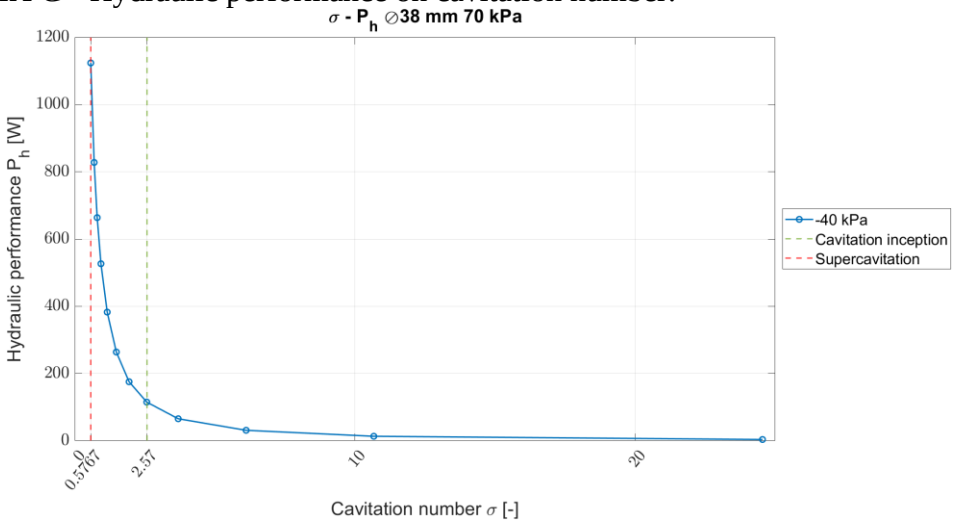

Figure 6-11 Hydraulic performance on cavitation number for cavitator with diameter 38mm

In Figure 6-12 is possible to obesrve, how loss coefficient behaves in dependancy on flow rate. At flow rate of 6 l/s, we can see that the loss coefficient drops. Tho flow rate of 6 l/s is when the cavitation was first observed with naked eye. At 13 l/s, the loss coefficient increases, as this is the flow rate, what supercavitation regime starts.

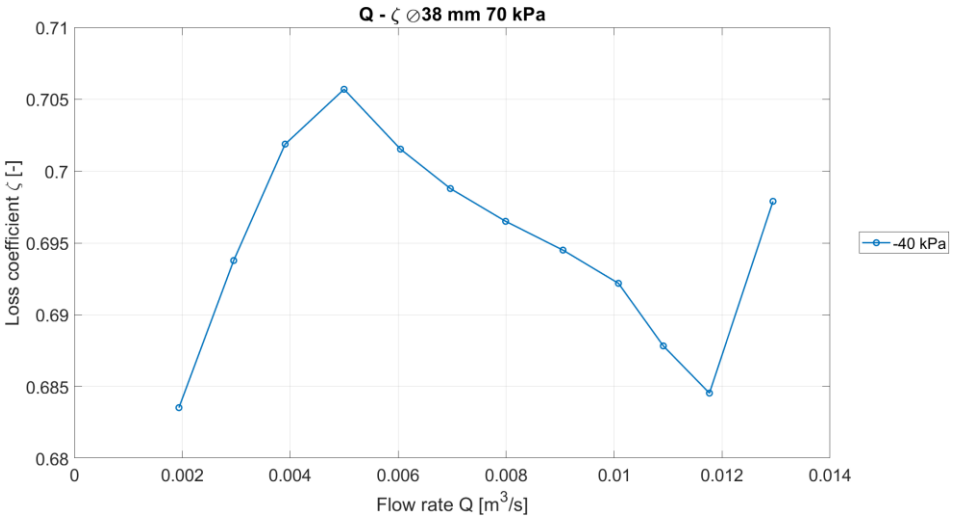

Figure 6-12 Dependancy of loss coefficient on flow rate for cavitator with diameter 38 mm

6.2 Recorded signal processing

Apart from hydraulic characteristics, it is possible to gain some knowledge about the dynamics of the flow from processing of recorded signals from sensor of acoustic emission. The signal from pressure sensor downstream of the cavitator is also processed in this work.

6.2.1 Fast Fourier Transform

To obtain knowledge about dynamics of the flow, the Fast Fourier Transform (FFT) of signals from acoustic emission (AE) sensor and from the pressure sensor downstream of the cavitation was performed. Fourier analysis converts a signal from original domain to frequency domain. The signal from AE sensor for cavitator diameter 38 mm, underpressure -40 kPa and flow rate of 9 l/s is shown in Figure 6-13 and corresponding FFT in Figure 6-14. From each FFT the amplitude and frequency of the main peak were plotted as a function of the cavitation number shown in Figure 6-15 and Figure 6-16. From these figures it is obvious that after the inception of cavitation both amplitude and frequency increase.

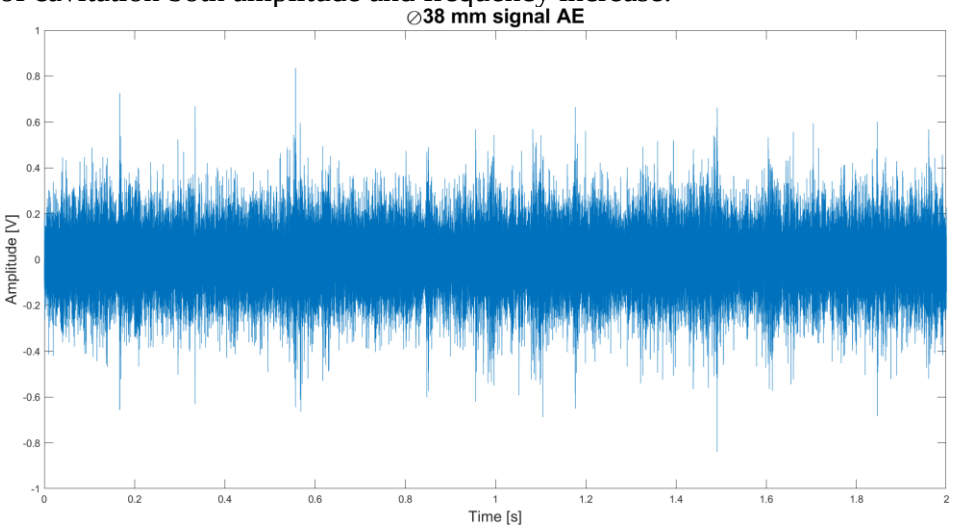

Figure 6-13 Signal recording for cavitator with diameter 38 mm -40 kPa and flow rate 9 l/s

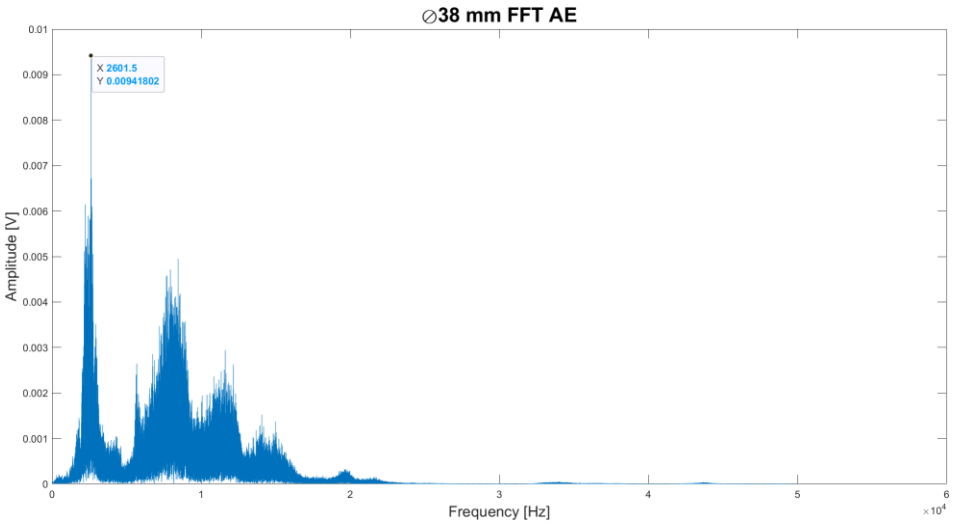

Figure 6-14 FFT for cavitator with diameter 38 mm -40 kPa and flow rate 9 l/s

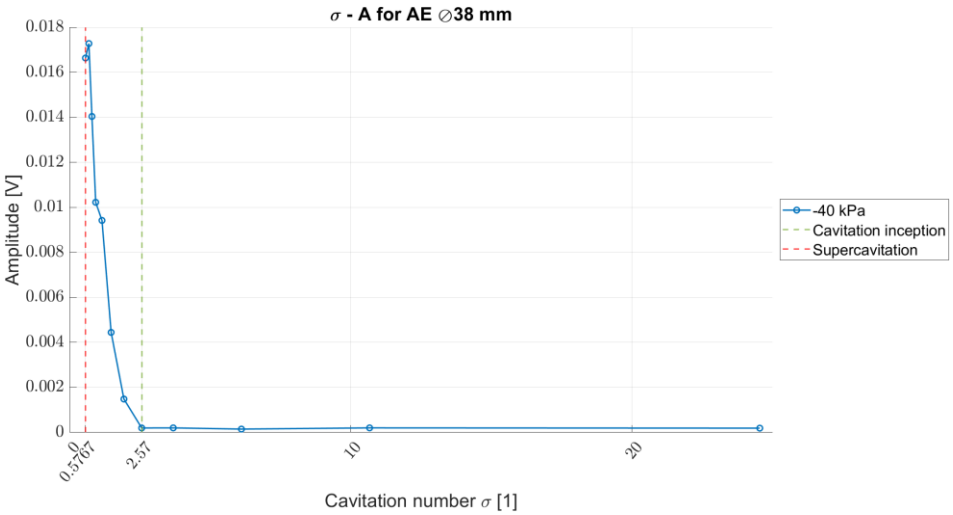

Figure 6-15 Values of peak amplitudes from FFT of AE sensor for each flow rate against cavitation number for cavitator with diameter 38 mm -40 kPa

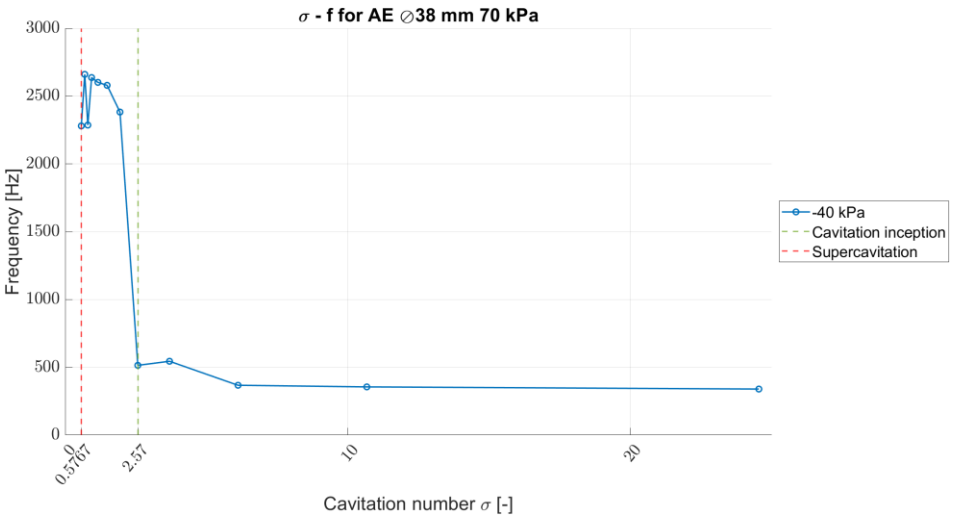

Figure 6-16 Values of peak frequencies from FFT of AE sensor for each flow rate against cavitation number for cavitator with diameter 38 mm -40 kPa

The same procedure was applied for signal evaluation from pressure sensor downstream of the cavitator and dependency of frequency and amplitude on cavitation number is shown in figures Figure 6-17 and Figure 6-18 respectively.

Figures with dependency of cavitation number on amplitude and on frequency for AE sensor are listed in the APPENDIX I - Acoustic emission FFT and dependency of cavitation number on amplitude and on frequency for pressure sensor are listed in the APPENDIX J - Pressure sensor FFT for each diameter of the cavitator. For the cavitator diameter of 40 mm for the atmospheric pressure and all overpressures, the dependency of amplitude on cavitation number doesn't follow the trend, which was observed with other diameters. The explanation to this difference is unfortunately unknown and could be due to some human error.

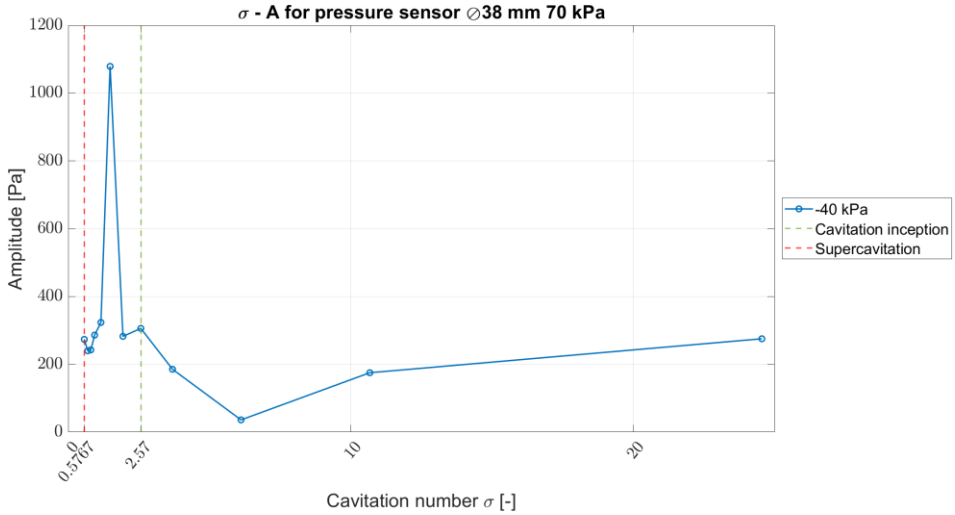

Figure 6-17 Values of peak amplitudes from FFT of pressure sensor for each flow rate against cavitation number for cavitator with diameter 38 mm and underpressure of 40 kPa

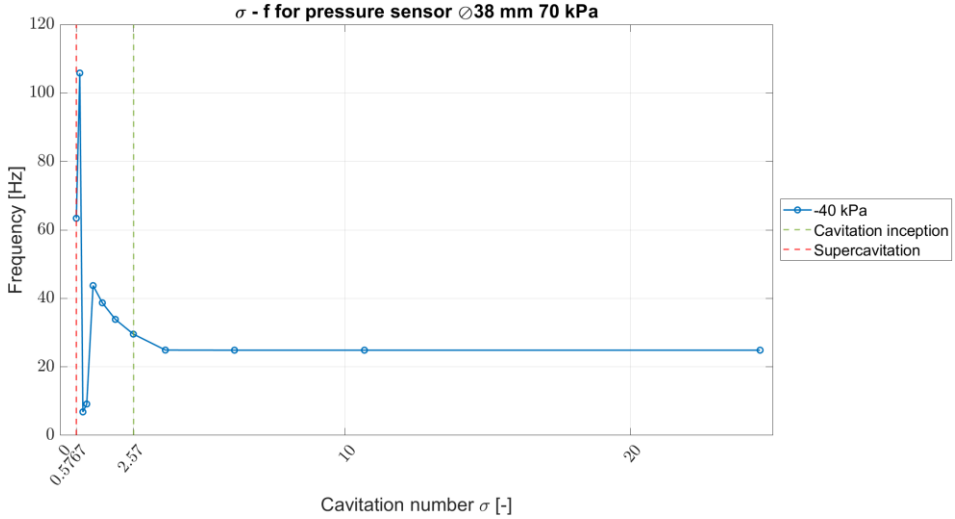

Figure 6-18 Values of peak frequencies from FFT of pressure sensor for each flow rate against cavitation number for cavitator with diameter 38 mm and underpressure of 40 kPa

6.2.2 Root Mean Square

Root mean square (RMS) is one of the most used ways of interpretation of signal of acoustic emission. RMS characterizes the power, eventually the intensity of the signal and is

measured in volts [V]. The root-mean-square value for an array, using the MATLAB software is calculated as:

$$x_{RMS} = \sqrt{\frac{1}{N}\sum_{n=1}^{N}|x_n|^2} \qquad (6.\ 14)$$

Value of RMS for each flow rate for diameter 38 mm and underpressure of 40 kPa plotted against the cavitation number is shown in Figure 6-19. The value of RMS increases after the inception of cavitation with lowering cavitation number. Figures with dependency of cavitation number on RMS for AE sensor are listed in the APPENDIX K - Acoustic emission RMS.

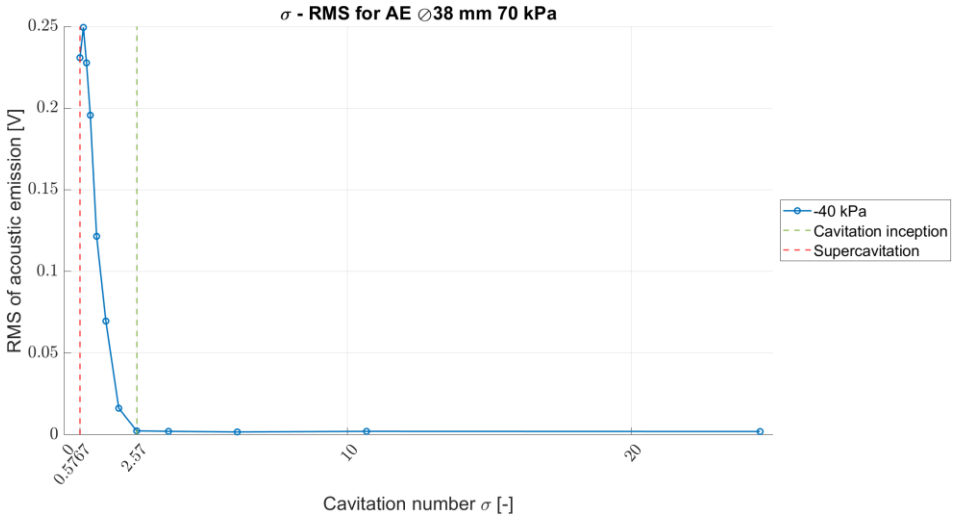

Figure 6-19 Values of RMS for each flow rate against cavitation number for cavitator with diameter 38 mm and underpressure of 40 kPa

7 Comparison of CFD and experimental values

To compare CFD simulation with experiment, the cavitation number for simulation must be calculated. Since the pressure downstream of the cavitation was taken from the pressure sensor, that was located further downstream, than the length of domain in simulation, the pressure from the outlet was considered in calculation. For the vapor pressure, the vapor pressure inputed into ANSYS Fluent simulation was consideredas shown in Figure 7-2. The comparsion itseld is shown in Figure 7-1. The picture of the experiment, taken by a phone camera, for setting of -50 kPa in the pressure vessel and flow rate of 11 l/s is shown in Figure 7-4 with closeup in Figure 7-5.

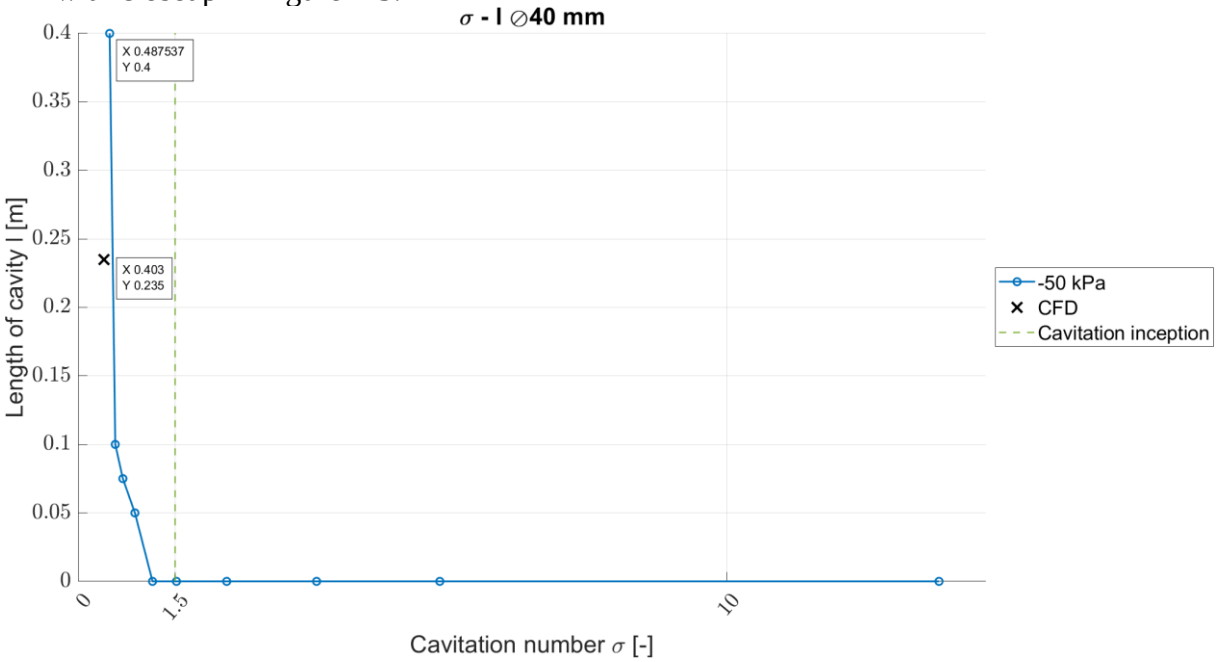

Figure 7-1 Comparison of length of cavity and cavitation number for CFD and experiment

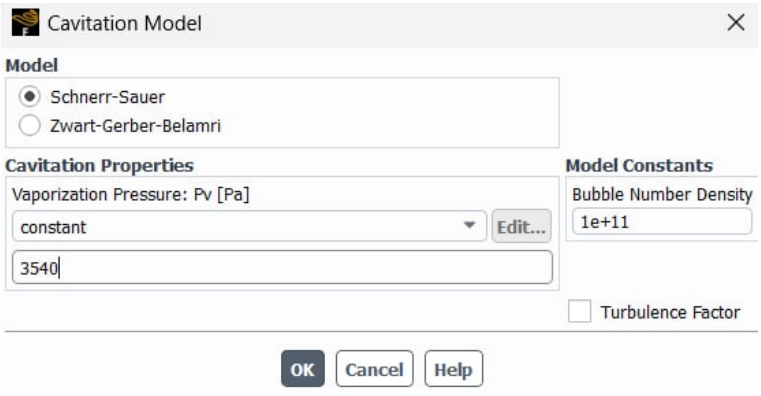

Figure 7-2 Vaporization pressure input into ANSYS Fluent

In Figure 7-3, the comparison of hydraulic performance and loss coefficient is shown. It can be observed, that for computational modeling, both loss coefficient and hydraulic performance is significantly overestimated.

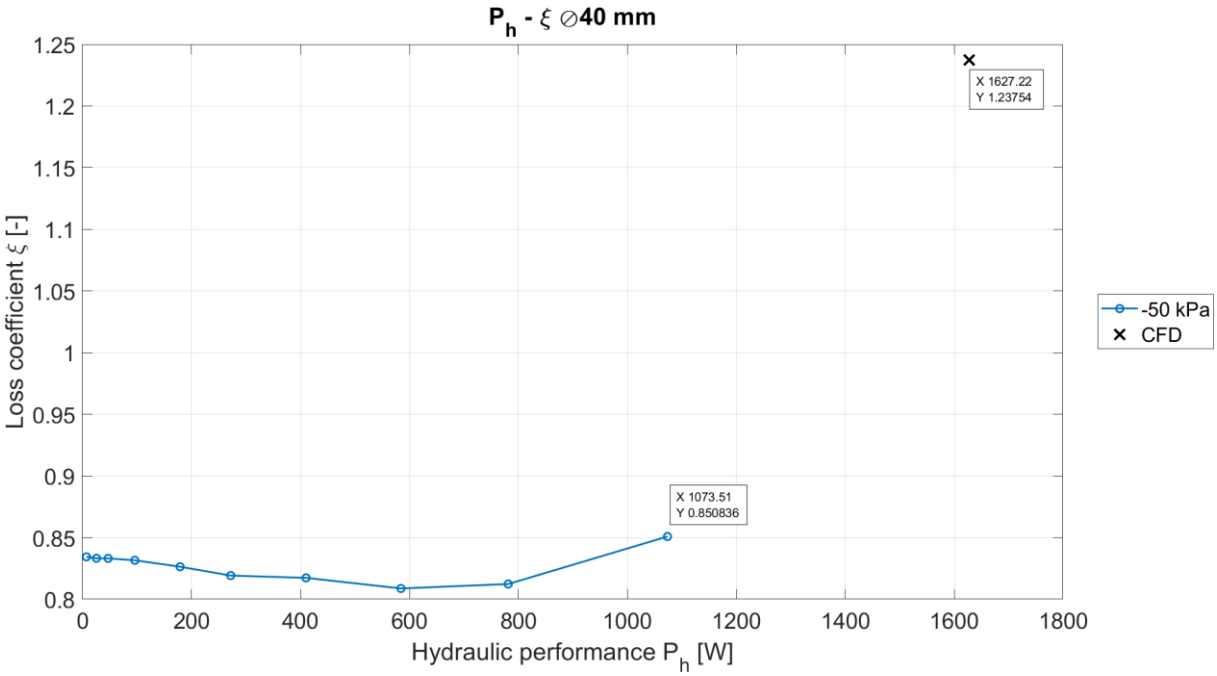

Figure 7-3 Comparison of hydraulic performance and loss coefficient for CFD and experiment

Figure 7-4 Picture of the experiment

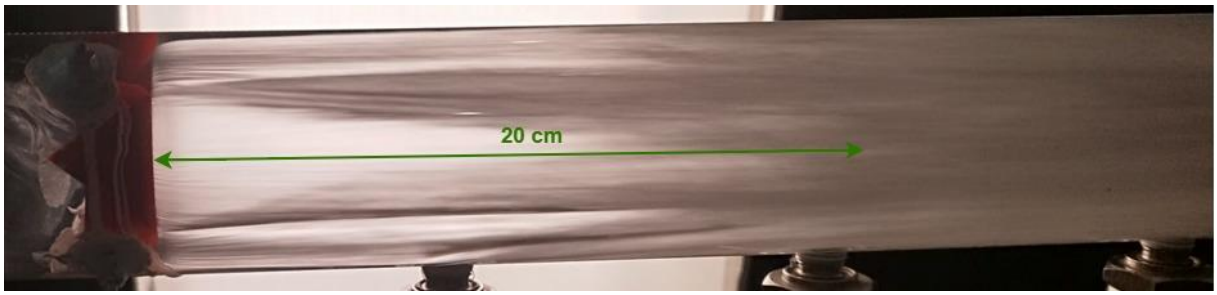

Figure 7-5 Closeup of the experiment

After taking a closer look at Figure 7-5 and Figure 7-6, it is obvious, that supercavitation itself collapses at around 20 cm. This value is much closer to the CFD value shown in Figure 7-7. The difference between the simulation and the experiment could be because the UDF with correction of turbulent viscosity for SST k-ω turbulence model was innapropriate for 2D domain and therefore wasn't used. To obtain more relevant data from simulations in the future, the simulations should be done with 3D domain and with implementation of UDF.

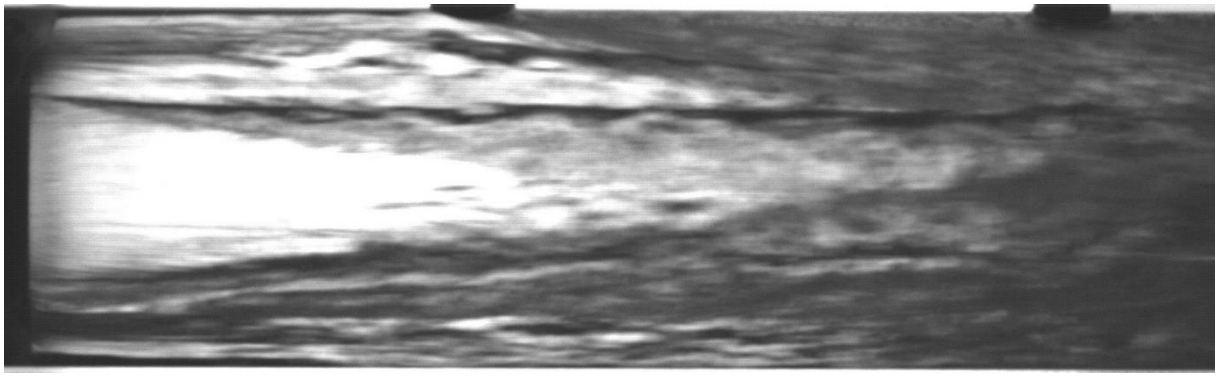

Figure 7-6 Image from high-speed camera for diameter of 40 mm, -50 kPa and flow rate of 11 l/s

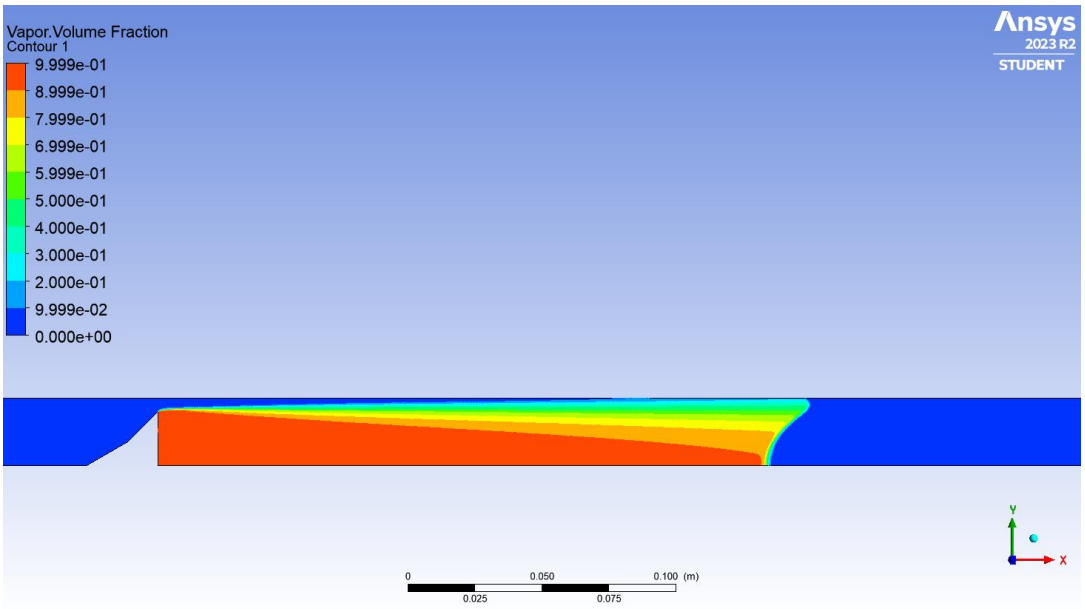

Figure 7-7 Vapor Volume Fraction of double-wedged cone

DISCUSSION

The main goal of the thesis was to propose suitable geometry using computational modelling and experimentally test it for different operating points. The measured data were also evaluated showing hydraulic characteristics and the signals from acoustic emission sensor and pressure sensor behind the cavitation cloud were processed using FFT and RSM. Another goal was to visualize the flow. The flow visualisation in this work is depicted in chapter 6.1.4 for one diameter of a cavitator and one downstream pressure level. All other visualization data is stored at a laboratory of V. Kaplan Department of Fluid Engineering as the files would take up too much space in this work.

In the beginning of computational modelling, the length of cavity was unknown, and domain of length of 1000 mm was proposed, with body located 250 mm from the inlet. After the experiment was conducted, the length of cavitation cloud showed to be 400 mm. Therefore, in the future the domain should be elongated. Simplification that was adopted of domain as 2D axisymmetric turned out to be inappropriate, especially after implementation of user defined function for correction of turbulent viscosity for SST k-ω turbulence model. In the future, it would be appropriate to perform simulations for more than just one operating point on 3D prolonged domain with implementation of UDF.

From the experiments the wide range of experimental data were obtained not only for the proposed geometry of given diameter, but also for one smaller and one larger diameter. All three geometries were subsequently reversed. Altogether six geometries were tested for range of pressure in pressure vessel from -50 kPa to 30 kPa with step of 10 kPa, and for each pressure setting, the range of flow rates from 2 l/s to 13 l/s, with step of 1 l/s was set.

To draw the conclusion, on which cavitator is best suitable for the CaviPlasma device, the table of flow rates, lengths of supercavitations, hydraulic performances, and ratio of power and volume of cavitation for gauge pressure -50 kPa is depicted in Table 4. Where the volume of cavitation is calculated as area of given cavitator base times length of the supercavitation region:

$$V_C = \frac{\pi d^2}{4} l \qquad (6.\ 15)$$

Where:

V_c	Volume of supercavitation	m^3
d	Diameter of the cavitator base	m
l	Length of supercavitation region	m

The data shown in Table 4 are the values at the beginning of supercavitation. The cavitator, that has the lowest energy demand according to the data in Table 4 is 38 mm reversed. For this cavitator, the supercavitation occurs at flow rate of 10 l/s. For the cavitator with diameter 38 mm, the hydraulic performance is only slightly higher than for the 38 mm reversed and the supercavitation occurs at flow rate of 12 l/s.

With increasing diameter, the required flow rate to induce supercavitation decreases, but the hydraulic performance increases. With the cavitator of diameter 38 mm, it is possible to process the largest volume of water using a relatively low hydraulic performance. However, when the ratio of hydraulic performance and volume of cavitation is calculated, the lowest value corresponds to the cavitator with diameter of 38 mm reversed. This means, that there is highest volume of vapor for corresponding hydraulic performance and the cavitator would be the most suitable choice.

Table 4 Flow rate and hydraulic performance for the start of supercavitation for gauge pressure -50kPa

Diameter of the cavitator	*Flow rate* [l/s]	*Length of supercavitation* [m]	*Hydraulic performance* [W]	$\frac{P_h}{V_c}$ [W/cm^3]
38 mm	12	0,14	891	5,612
40 mm	11	0,4	1 073,5	2,136
42 mm	10	0,64	1 387,12	1,564
38 mm reversed	10	0,57	885,74	1,37
40 mm reversed	9	0,28	928,94	2,64
42 mm reversed	8	0,4	1 114,54	2,011

For low flow rates, the calculated error of measurement was extremely large due to pressure difference very close to the error of sensors. This fact can cause, that the shape of characteristics in non-cavitation regimes doesn't reflect reality. Another big problem was observed during data evaluation, when the pressure sensor downstream of the cavitation was often too close (or even in the way) of cavitation cloud. From the experiments, it was observed, that after the cavitation reaches supercavitation regime, the length of the cloud grows rapidly. To obtain more data in the supercavitational regimes, the experiments need to be executed again with more suitable spacing of pressure sensors. Another problem that occurred during the experiments, was insufficient length of plexiglass tube and insufficient length of light for visualisation of data.

To encapsulate the essence of everything said above, in each aspect of this work, there is a room for improvement with proposed solutions. This work offers introductory understanding of supercavitation behind an obstacle and should serve as a starting point for future research.

CONCLUSION

During nine months in which this work was completed, many obstacles had to be tackled as the problematic of supercavitation behind an obstacle was a new topic at V. Kaplan Department of Fluid Engineering. Previous research that dealt with non-ventilated cavitation behind an obstacle was studied but the idea of behaviour could be better understood only at the very end of this work when the experiments were conducted.

In the first stage of the work, when a suitable shape of the body was proposed using computational modelling, the task was simplified to a 2D axisymmetric. With implementation of UDF, this simplification proved to be incorrect.

After choosing the geometry, the body itself was made using FDM with PETG material. The mounting supports were added into the 3D geometry, to ensure the centring of the body and to enable attachment to the tube. The same body was made in 5 versions, with different maximum diameters ranging from 22,9 mm to 45,8 mm. However, only 3 of the bodies were successfully tested. During the experiments, not only the proposed bodies were tested for several operating points, but also the reversed geometries, which made it possible to expand the measured data.

The processing of the data was done in MATLAB software. When processing the data, it was observed, that pressure sensor downstream of the cavitator was often affected during the supercavitation regime and the data couldn't be used. To better understand the supercavitational regimes, the experiments should be conducted again, using a more suitable placement of sensors and longer plexiglass tube, to properly see the length of cavitational cloud.

In conclusion, this work offers a gateway for research regarding use of supercavitaion behing an obstacle for water purification. A lot of data were collected and can be used for comparison with other methods of inducing cavitation. Many problems were depicted and their solutions were offered to gain better knowledge of the problematic.

REFERENCES

[1] NOSKIEVIČ, Jaromír. Kavitace. Praha: Academia, 1969. ISBN 21-047-69.

[2] ROY, Samir, 2015. Modeling and analysis of material behaviour during cavitation erosion. DOCTORATE OF THE UNIVERSITY GRENOBLE ALPES. Grenoble: Université Grenoble Alpes.

[3] FRANC, Jean-Pierre a MICHEL, Jean-Marie. Fundamentals of Cavitation. Springer, 2006. ISBN 978-1-4020-2233-3.

[4] FLUIDON. *Cavitation*. Online. Available at: https://www.fluidon.com/en/tools/dshplus/piping/cavitation. [Accessed 19 January 2024].

[5] Standard Test Method for Pin Abrasion Testing. ASTM International - Standards Worldwide. Available from: https://www.astm.org/g0132-96r18.html. [Accessed 1 February 2024].

[6] SINIBALDI, G., OCCHICONE, A., ALVES PEREIRA, F., CAPRINI, D., MARINO, L., MICHELOTTI, F., CASCIOLA, C. M.: Laser induced cavitation: Plasma generation and breakdown shockwave. Physics of Fluids, 1 October 2019, vol. 31, no. 10, 103302. DOI: https://doi.org/10.1063/1.5119794.

[7] Michel, J.M. Introduction to Cavitation and Supercavitation. RTO AVT Lecture Series on "Supercavitating Flows", February 2001, Bruxelles, Belgium. HAL-03013734.

[8] BRENNEN, Christopher E. Cavitation and Bubble Dynamics. Cambridge: Cambridge University Press, 2013. DOI: 10.1017/CBO9781107338760. ISBN 9781107338760.

[9] ISLAM, Tajamul; ALTAF, Hamid; BASHIR, Seerab and ZAHOOR, Rutbah, 2021. A case study about cavitation. In: *International journal of creative research thoughts*. 9. ISSN 2320-2882. Available at: https://doi.org/10.1729/Journal.28568.

[10] MOGHIMI, M.; NOURI, Nowrouz Mohammad and MOLAVI, Esmael, 2017. Experimental Investigation on Supercavitating Flow over Parabolic Cavitators. Online. *Journal of Applied Fluid Mechanics*. 2017-1-1, roč. 10, č. 1, pp. 95-102. ISSN 1735-3572. Available at: https://doi.org/10.18869/acadpub.jafm.73.238.26678.

[11] VYSOKÉ UČENÍ TECHNICKÉ V BRNĚ, BRNO, VEVEŘÍ, CZ MASARYKOVA UNIVERZITA, BRNO, BRNO-MĚSTO, CZ BOTANICKÝ ÚSTAV AV ČR, V.V.I., PRŮHONICE, CZ (Česká republika). Zařízení pro čištění kapalin a způsob čištění kapalin s využitím tohoto zařízení. Doc. Ing. Pavel Rudolf, Ph.D., Blansko, CZ prof. Ing. František Pochylý, CSc., Brno, Žabovřesky, CZ doc. Mgr. Pavel Sťahel, Ph.D., Brno, Starý Lískovec, CZ doc. RNDr. Jozef Ráheľ, Ph.D., Brno, Nový Lískovec, CZ Mgr. Jan Čech, Ph.D., Brno, Bohunice, CZ prof. Ing. Blahoslav Maršálek, CSc., Brno, Chrlice, CZ. Přihl.: 13.12.2019. Uděl.: 16.09.2020. Available at: https://isdv.upv.gov.cz/doc/FullFiles/Patents/FullDocuments/308/308532.pdf. [Accessed. 23 January 2024].

[12] MARŠÁLEK, Blahoslav; MARŠÁLKOVÁ, Eliška; ODEHNALOVÁ, Klára; POCHYLÝ, František; RUDOLF, Pavel et al., 2020. Removal of Microcystis aeruginosa through the Combined Effect of Plasma Discharge and Hydrodynamic Cavitation. Online. Water. Roč. 12, č. 1. ISSN 2073-4441. Available at: https://doi.org/10.3390/w12010008. [Accessed 2 November 2023].

[13] BALKO, M., MONKOVÁ, P., RUDOLF, P. Hydraulic characteristics of the convergent-divergent nozzle with the inner electrode in cavitating conditions. In: MATEC Web of Conferences, October 2023, vol. 383. DOI: 10.1051/matecconf/202338300002.

[14] SHAFAGHAT, R., HOSSEINALIPOUR, S.M., LASHGARI, I., VAHEDGERMI, A. Shape optimization of axisymmetric cavitators in supercavitating flows, using the NSGA II algorithm. Applied Ocean Research, 2011, vol. 33, no. 3, pp. 193–198. DOI: 10.1016/j.apor.2011.03.001.

[15] GOPALA KRISHNAN, T., Lokesharun, D., Saravanan, R., Poornachandiran, N. (2020). *CFD based shape optimization of axisymmetric cavitators in supercavitating flows . AIP Conference Proceedings PROCEEDINGS OF INTERNATIONAL CONFERENCE ON RECENT TRENDS IN MECHANICAL AND MATERIALS ENGINEERING: ICRTMME 2019.* doi:10.1063/5.0025254

[16] ANSYS, Inc. Mixture Model Theory. [online] Available from: https://www.afs.enea.it/project/neptunius/docs/fluent/html/th/node343.htm. [Accessed 3 March 2024].

[17] ANSYS, Inc. Cavitation Models. [online] Available from: https://www.afs.enea.it/project/neptunius/docs/fluent/html/th/node343.htm. [Accessed 3 March 2024].

[18] Courant Number in CFD. SimFlow [online]. Available at: https://sim-flow.com/courant-number-in-cfd/ [Accessed 20 January 2024].

[19] ZEMAN, Radek. Hydrodynamická kavitace v minifluidické Venturiho dýze. Brno, 2022. Dostupné také z: https://www.vutbr.cz/studenti/zav-prace/detail/143010. Diplomová práce. Vysoké učení technické v Brně, Fakulta strojního inženýrství, Energetický ústav. Vedoucí práce Pavel Rudolf. [Accessed 8 April 2024]

[20] ZHANG, Xin-Lei; GE, Ming-Ming; ZHANG, Guang-Jian and COUTIER-DELGOSHA, Olivier, 2021. Compressible effects modeling for turbulent cavitating flow in a small venturi channel: An empirical turbulent eddy viscosity correction. Online. *Physics of Fluids*. 2021-03-01, roč. 33, č. 3. ISSN 1070-6631. Available at: https://doi.org/10.1063/5.0041463.

[21] COUTIER-DELGOSHA, O.; FORTES-PATELLA, R. and REBOUD, J. L., 2003. Evaluation of the Turbulence Model Influence on the Numerical Simulations of Unsteady Cavitation. Online. *Journal of Fluids Engineering*. 2003-01-01, roč. 125, č. 1, pp. 38-45. ISSN 0098-2202. Available at: https://doi.org/10.1115/1.1524584.

[22] JONES, F.E., HARRIS, G.L., ITS-90 density of water formulation for volumetric standardscalibration. Journal of research of the National Institute of Standards and Technology,97(3), pp.335-340. (1992) [Accessed 8 May 2024].

[23] HUANG, J., A Simple Accurate Formula for Calculating Saturation Vapor Pressure ofWater and Ice. Journal of applied meteorology and climatology, 57(6), pp.1265-1272.(2018) [Accessed 8 May 2024].

[24] PALENČÁR, R., VDOLEČEK, F., HALAJ, M.:Nejistoty v měření III: nejistoty nepřímých měření, Automa, 7, 2001, no. 12, pg. 28-33.

[25] PALENČÁR, R., VDOLEČEK, F., HALAJ, M.:Nejistoty v měření I: vyjadřování nejistot, Automa, 7, 2001, no. 7-8, pg. 50-54.

SYMBOLS AND ABBREVIATIONS

Abbreviation	**Meaning**
AE	Acoustic emission
CD	Convergent-divergent
CFD	Computational Fluid Modelling
FDM	Fused Deposition Modelling
FFT	Fast Fourier Transform
NSGA-I	Non-Dominated Sorting Genetic Algorithm version I
PAW	Plasma Activated Water
RANS	Reynolds Averaged Navier-Stokes
RMS	Root-Mean Square
SST	Shear Stress Transport
UDF	User Defined Function

LIST OF FIGURES

LIST OF TABLES

LIST OF ATTACHMENTS

APPENDIX A - User defined function

```
/**UDF to modify the Turbulence Viscosity **/
#include "udf.h"
#include "mem.h"
#define max(a,b) (((a) > (b)) ? (a) : (b))
DEFINE_TURBULENT_VISCOSITY(cavitation_mu_t, c, t)
{
 int n = 10;
 Thread** pt = THREAD_SUB_THREADS(t);
 real omega = C_O(c,t);
 real k = C_K(c,t);
 real y = C_WALL_DIST(c,t);
 real rhoM = C_R(c, t);
 real rhoL = C_R(c, pt[P_PHASE]);
 real rhoV = C_R(c, pt[S_PHASE]);
 real f_of_rho = rhoV + pow((rhoM - rhoV)/(rhoL - rhoV), n)*(rhoL - rhoV);
 real phi_2 =
max(2*pow(k,0.5)/(0.09*omega*y),500*C_MU_L(c,t)/(rhoM*SQR(y)*omega));
 real F_2 = tanh(SQR(phi_2));
 real a_star =
1*(0.072/3+rhoM*k/(omega*C_MU_L(c,t))/6)/(1+rhoM*k/(omega*C_MU_L(c,t))/6);
 return
f_of_rho*k/omega/max(1/a_star,C_STRAIN_RATE_MAG(c,t)*F_2/(0.31*omega));
}
```

APPENDIX B - Pump and motor parameters

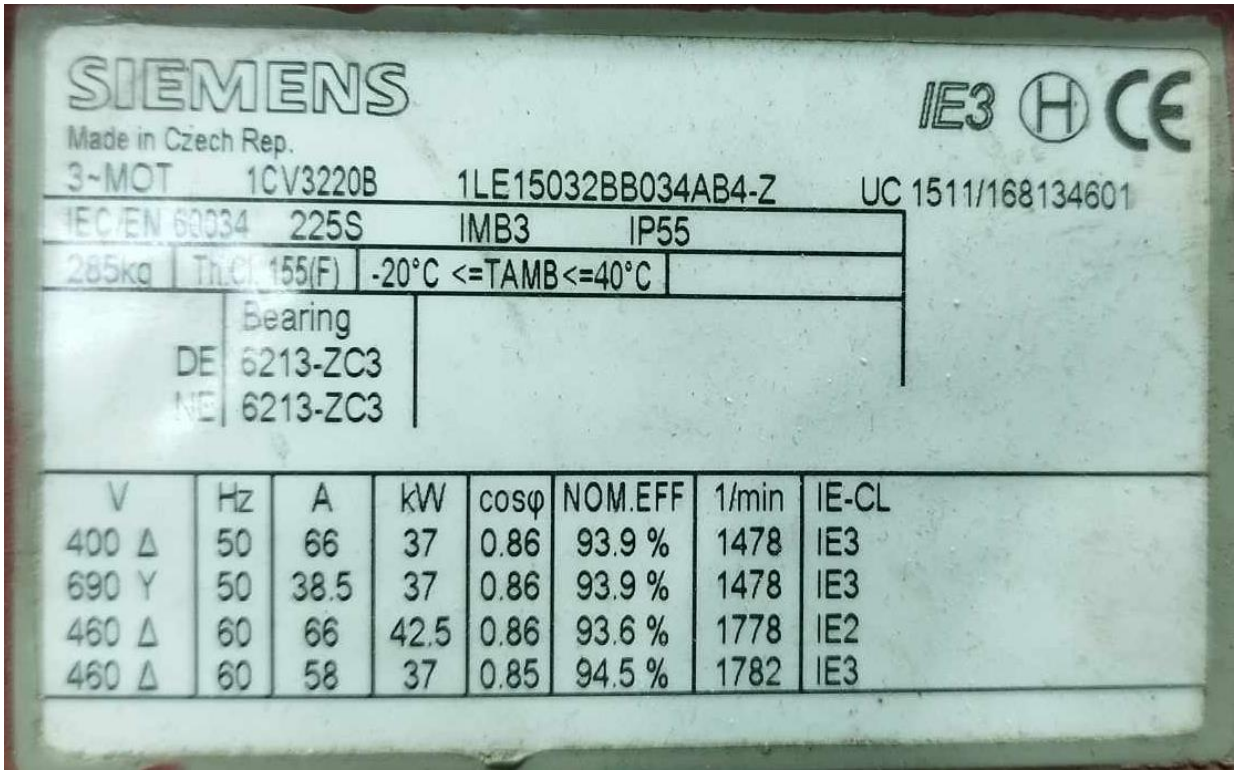

APPENDIX C - Hydraulic characteristics

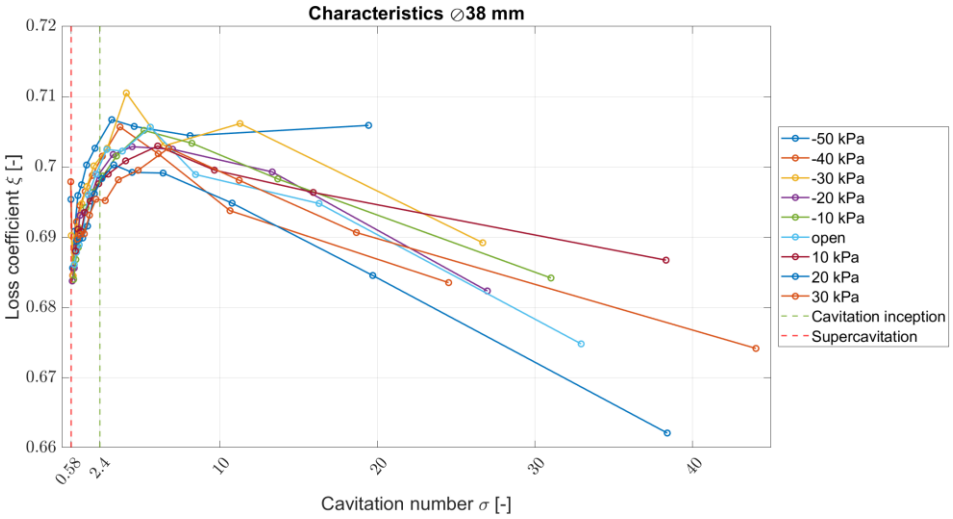

Hydraulic characteristic 38 mm

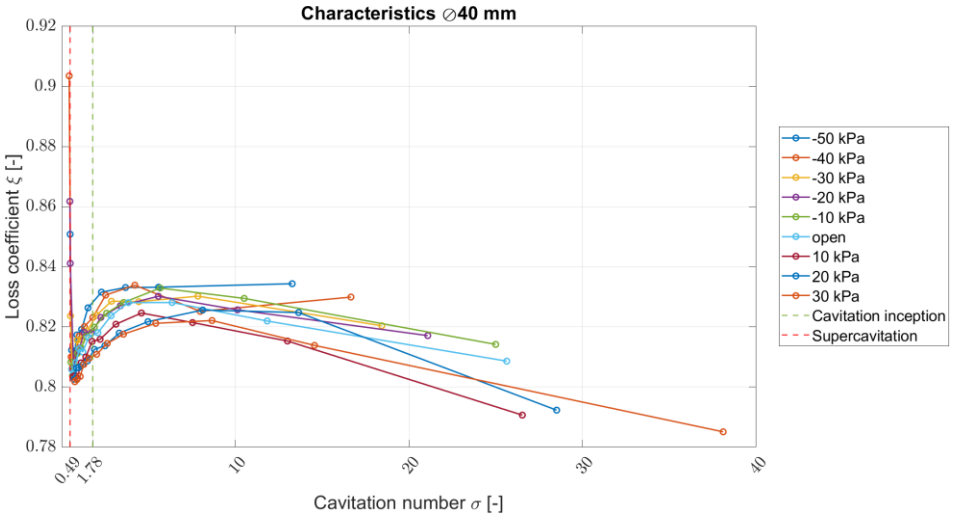

Hydraulic characteristic 40 mm

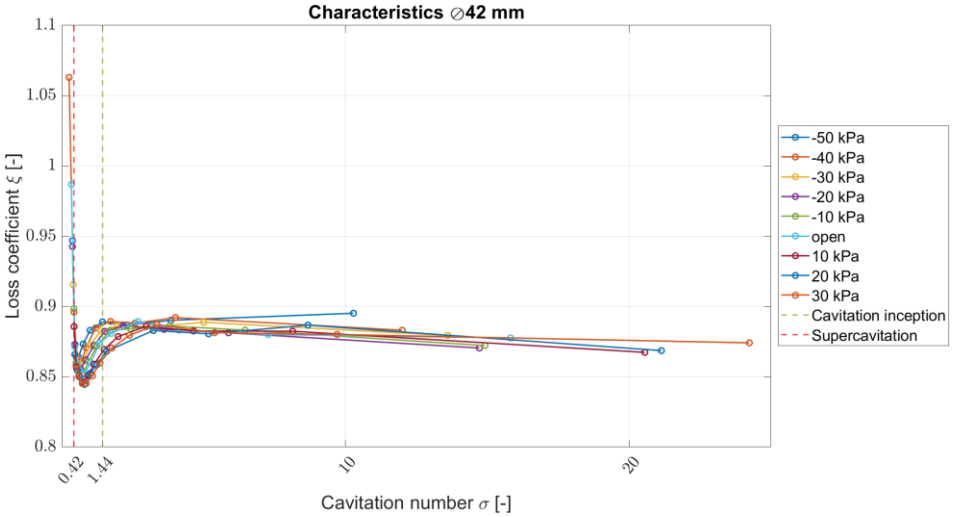

Hydraulic characteristic 42 mm

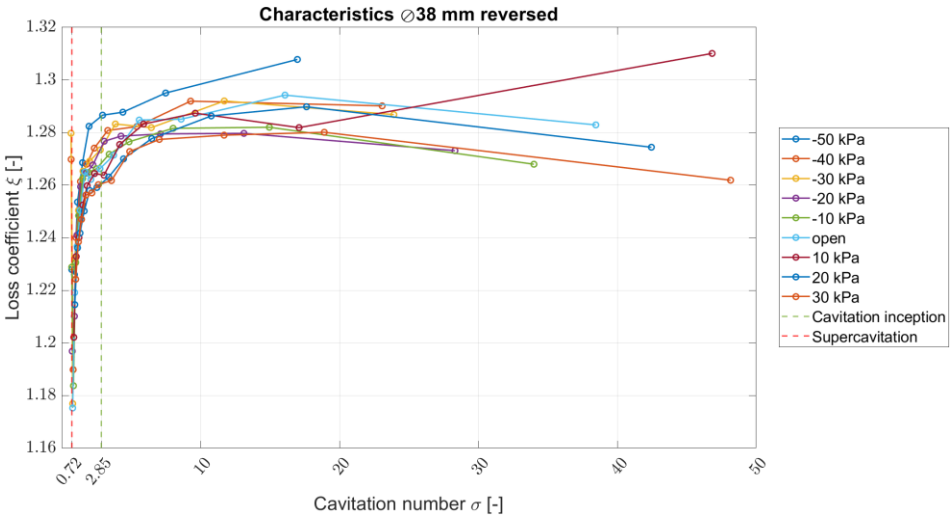

Hydraulic characteristic 38 mm reversed

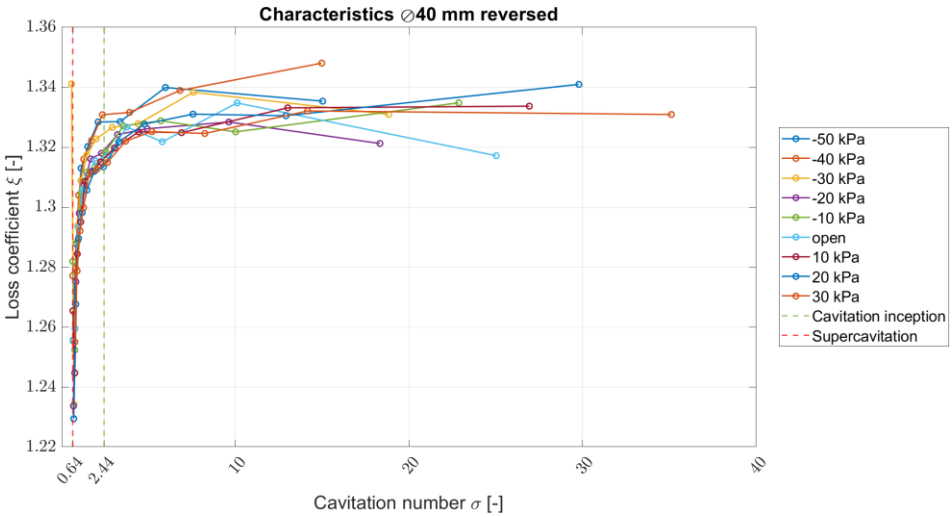

Hydraulic characteristic 40 mm reversed

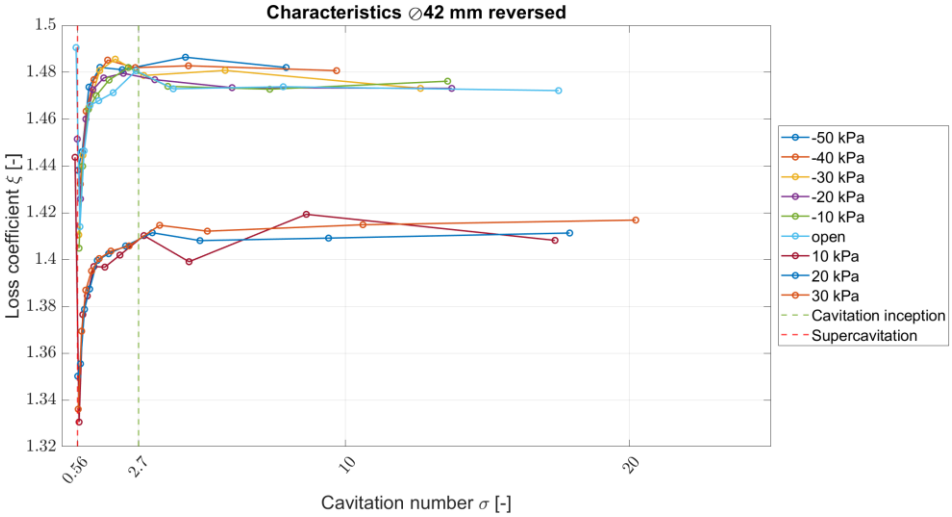

Hydraulic characteristic 42 mm reversed

APPENDIX D - Errorbar for hydraulic characteristics

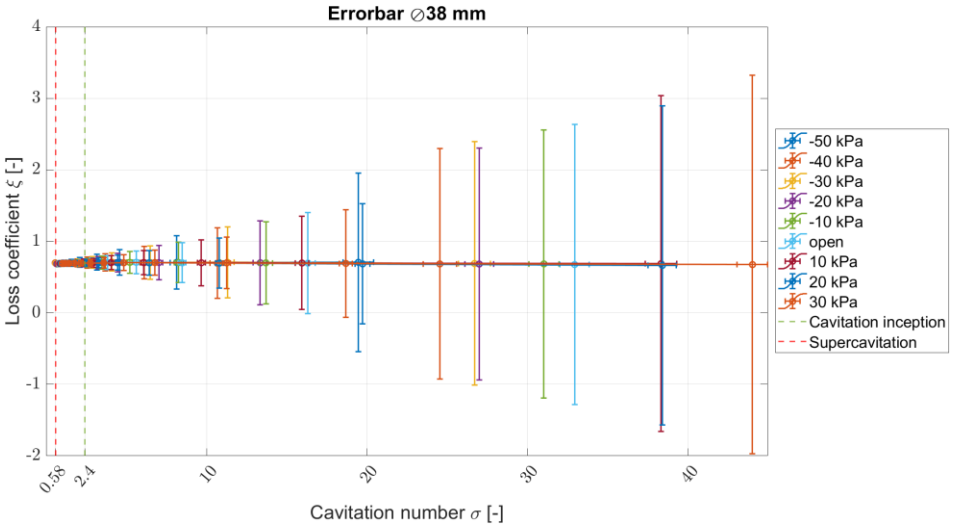

Errorbar of hydraulic characteristic 38 mm

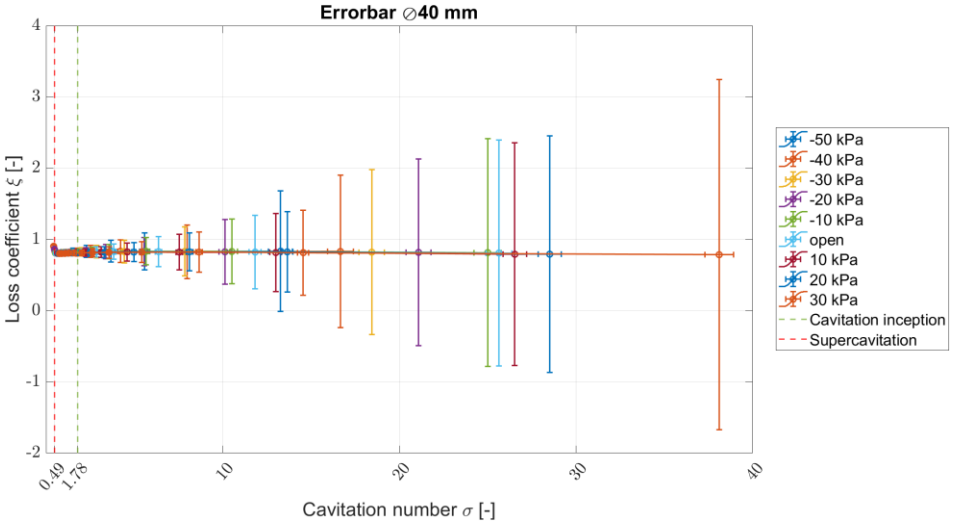

Errorbar of hydraulic characteristic 40 mm

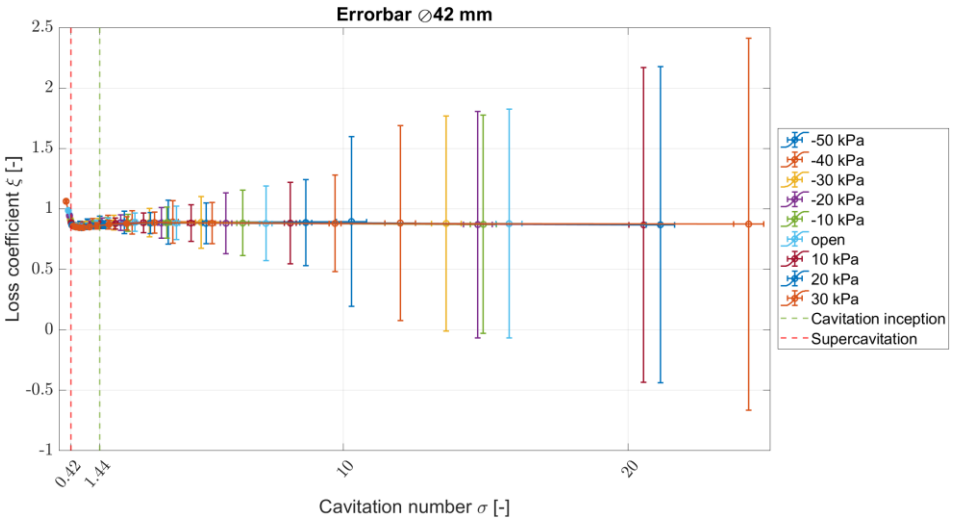

Errorbar of hydraulic characteristic 42 mm

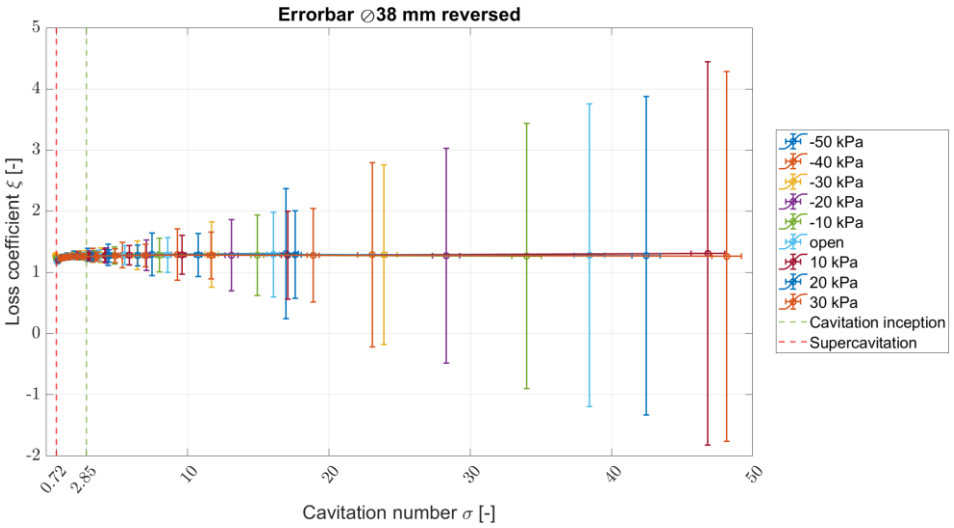

Errorbar of hydraulic characteristic 38 mm reversed

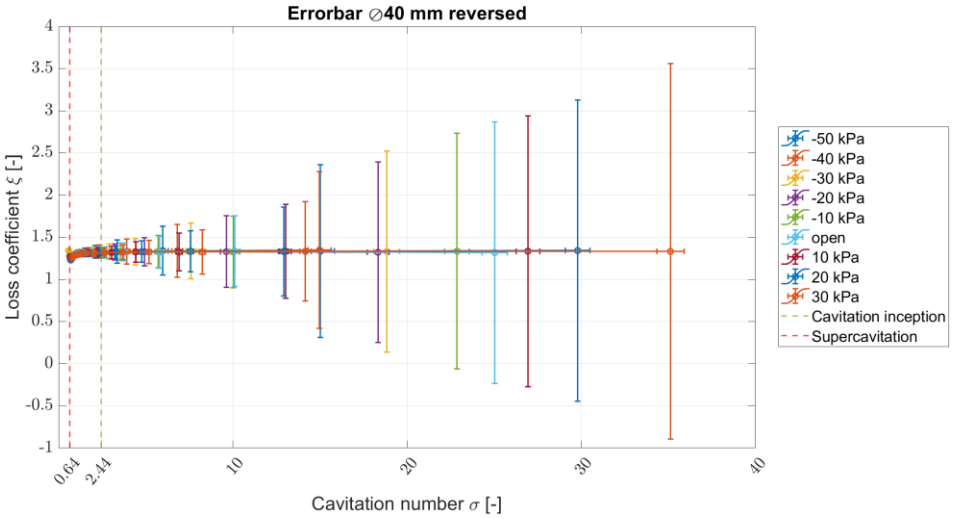

Errorbar of hydraulic characteristic 40 mm reversed

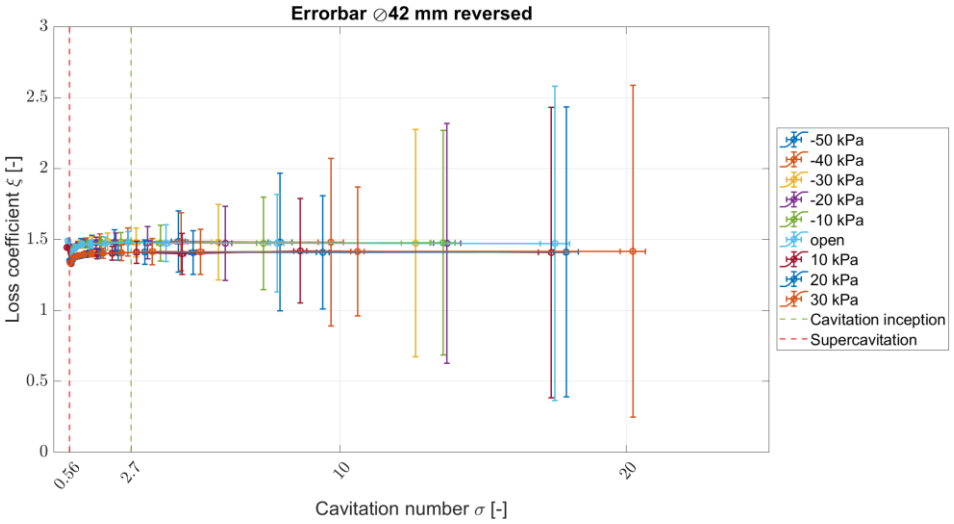

Errorbar of hydraulic characteristic 42 mm reversed

APPENDIX E - Length of cavity on cavitation number

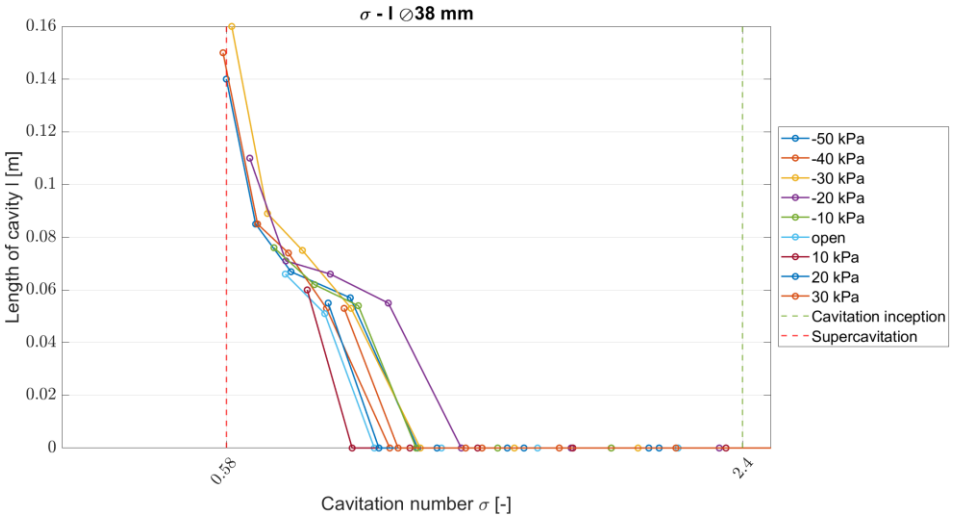

Length of cavity on cavitation number 38 mm

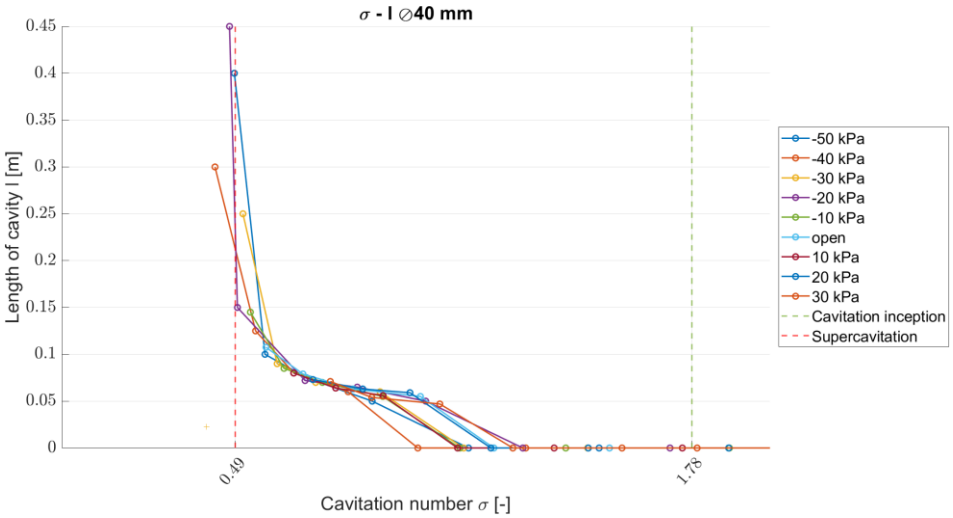

Length of cavity on cavitation number 40 mm

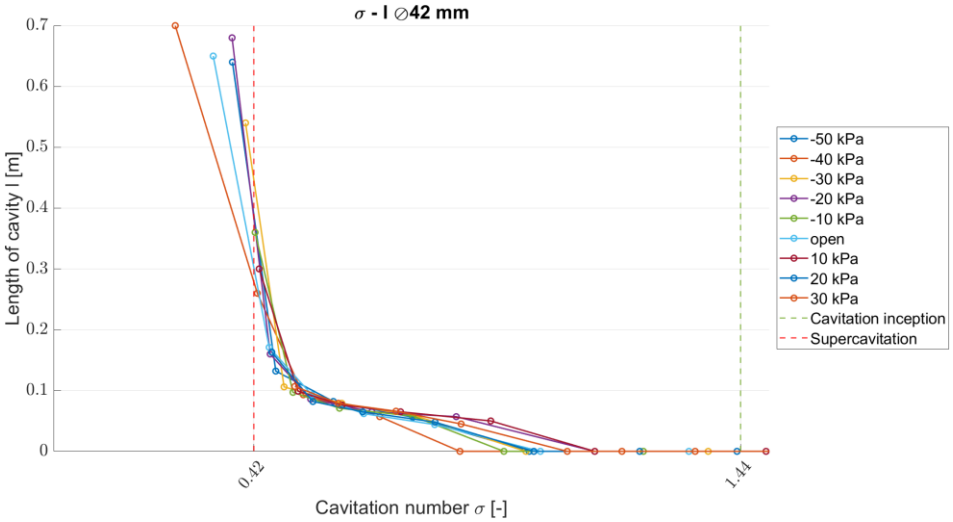

Length of cavity on cavitation number 42 mm

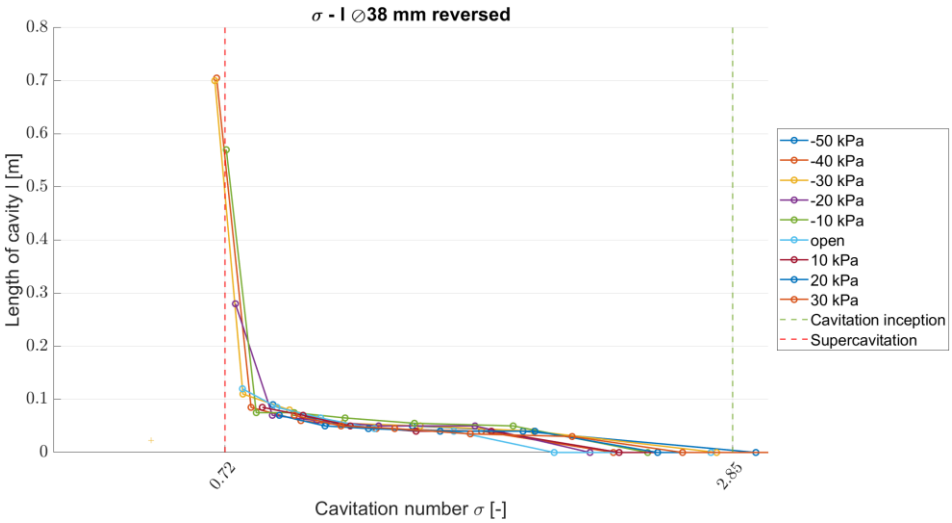

Length of cavity on cavitation number 38 mm reversed

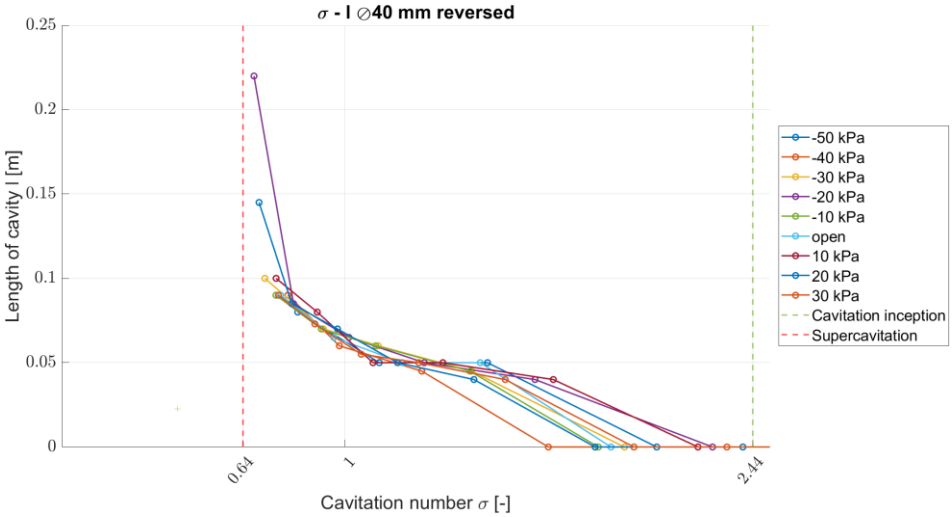

Length of cavity on cavitation number 40 mm reversed

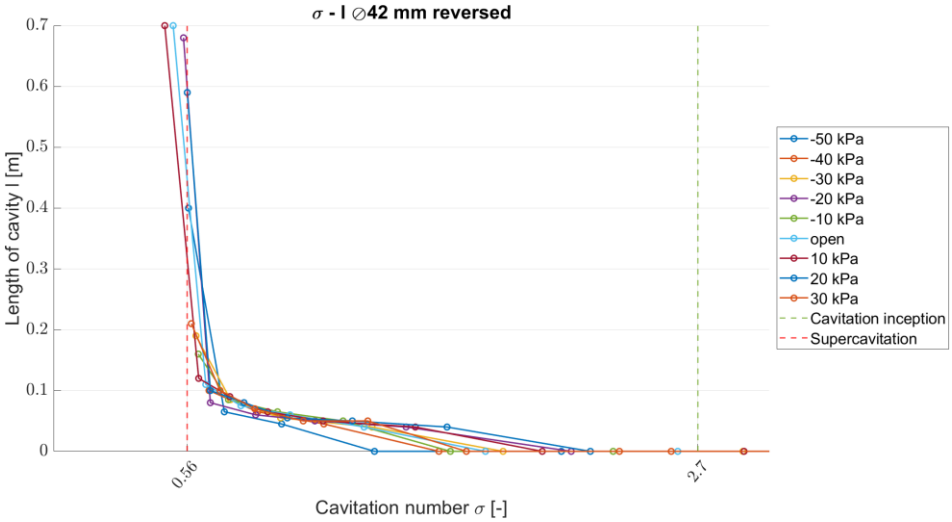

Length of cavity on cavitation number 42 mm reversed

APPENDIX F - Pressure difference on cavitation number

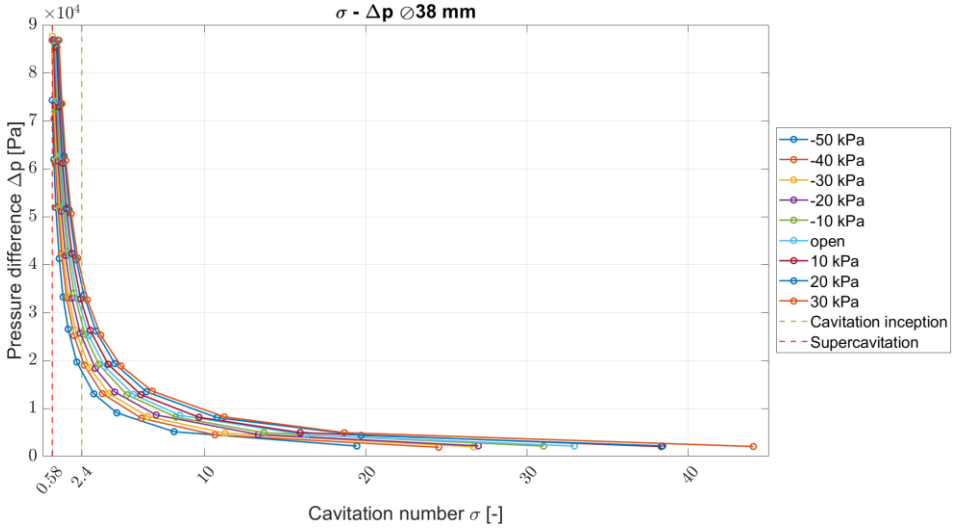

Dependancy of pressure difrence on cavitation number for cavitator of diameter 38 mm

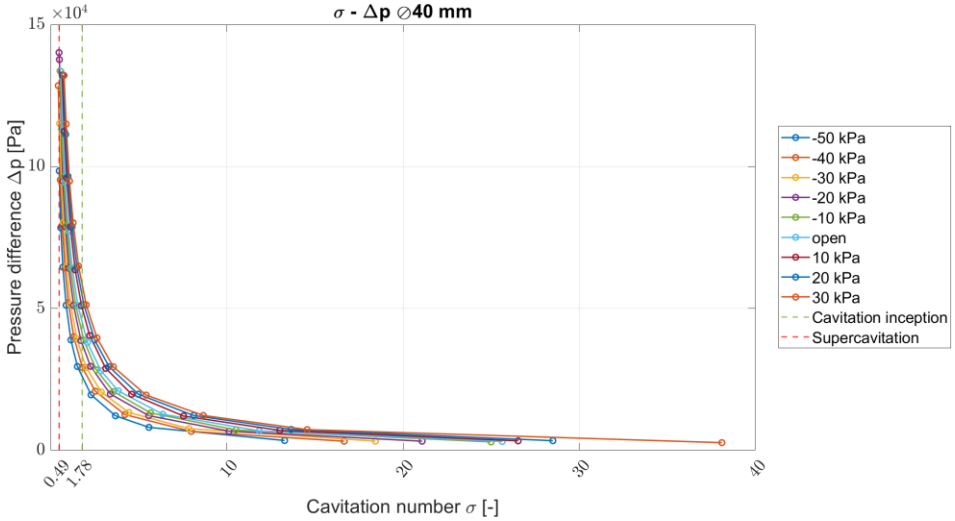

Dependancy of pressure difrence on cavitation number for cavitator of diameter 40 mm

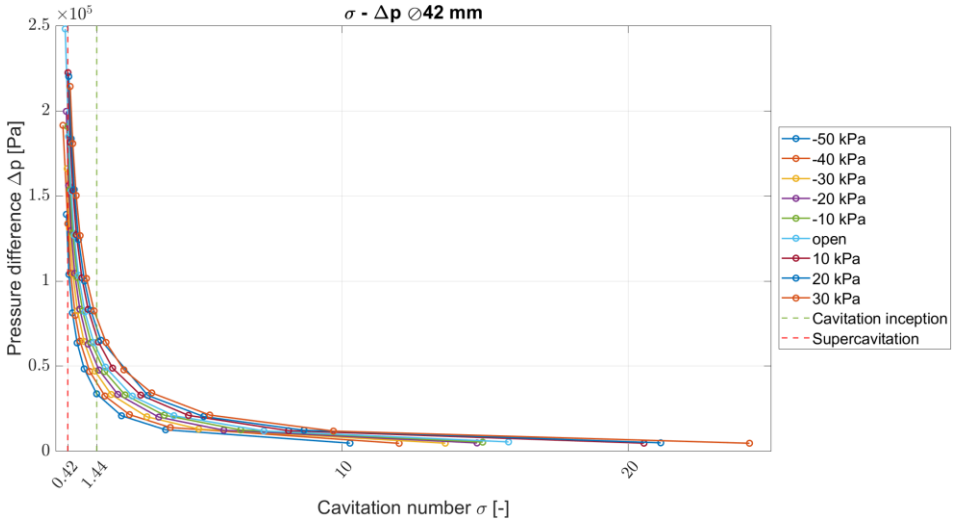

Dependancy of pressure difrence on cavitation number for cavitator of diameter 42 mm

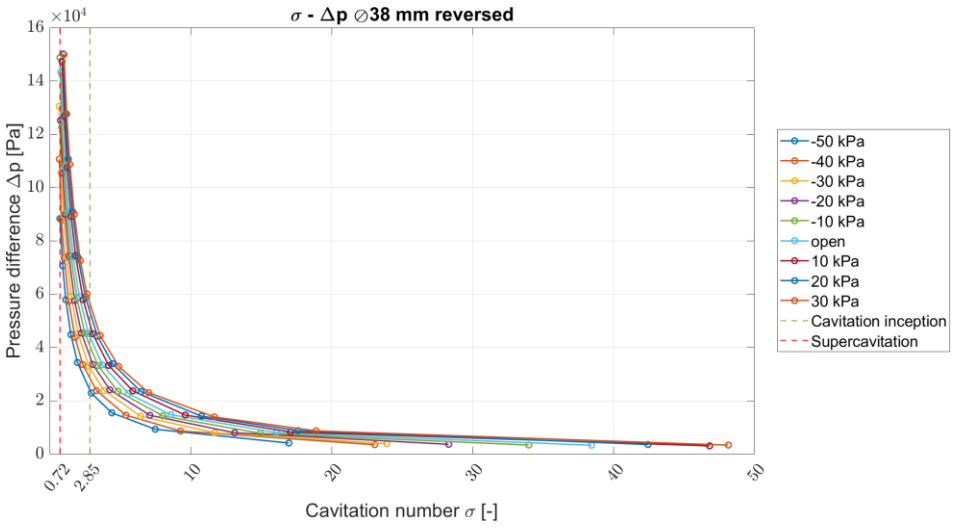

Dependancy of pressure difrence on cavitation number for cavitator of diameter 38 mm reversed

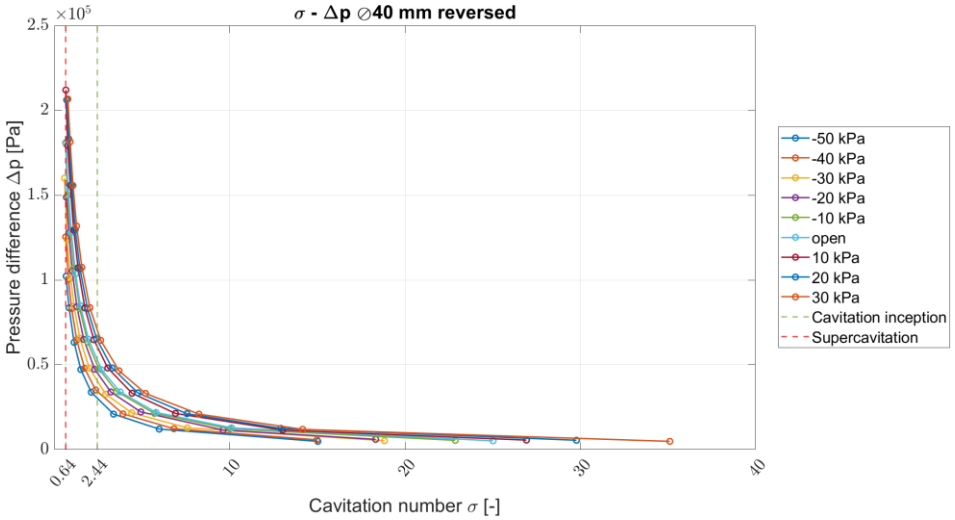

Dependancy of pressure difrence on cavitation number for cavitator of diameter 40 mm reversed

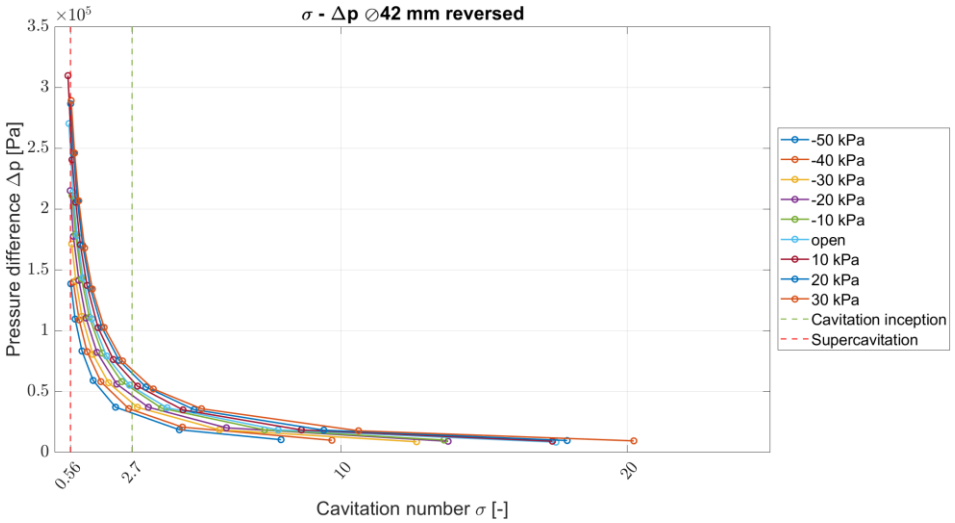

Dependancy of pressure difrence on cavitation number for cavitator of diameter 42 mm reversed

APPENDIX G - Hydraulic performance on cavitation number

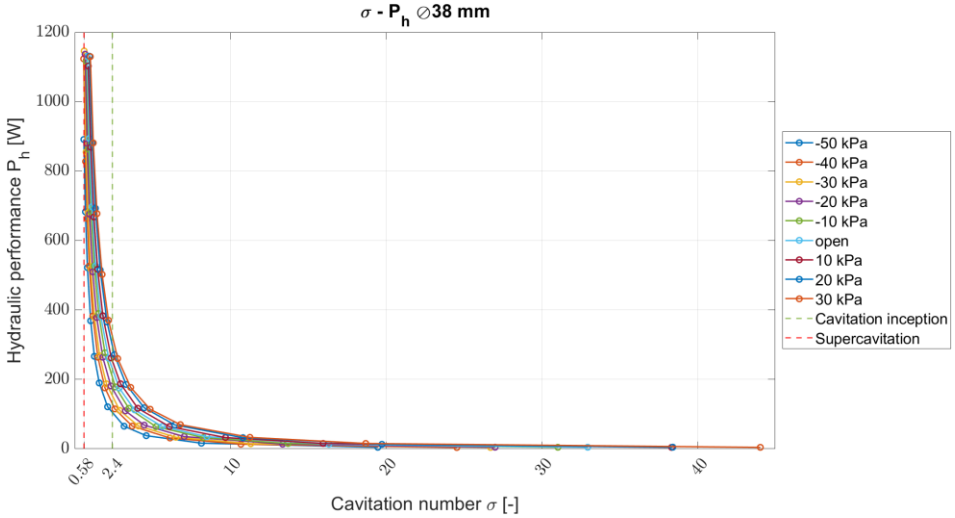

Hydraulic performance on cavitation number for cavitator with diameter 38 mm

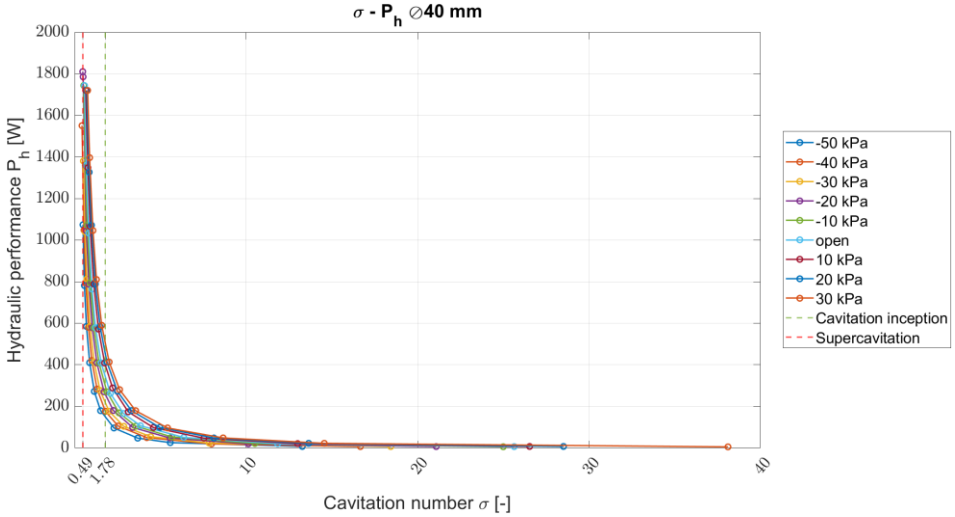

Hydraulic performance on cavitation number for cavitator with diameter 40 mm

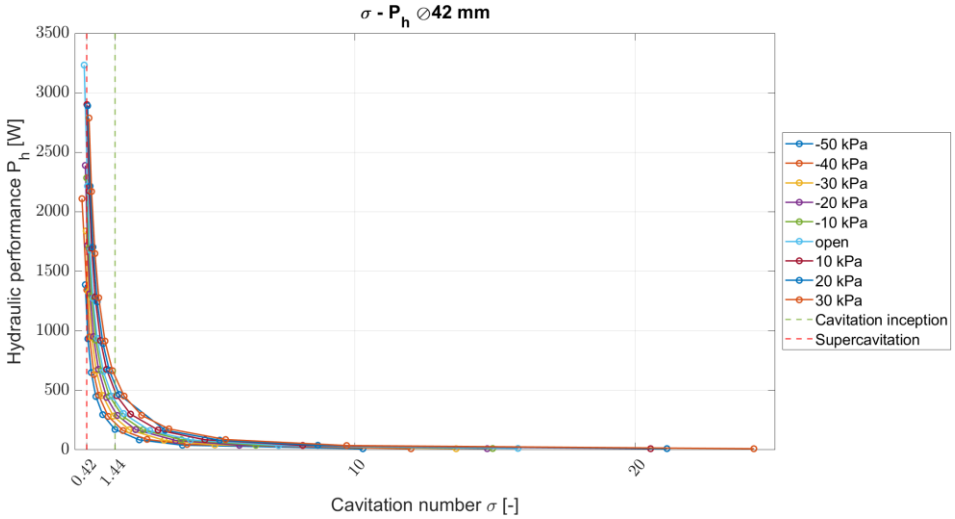

Hydraulic performance on cavitation number for cavitator with diameter 42 mm

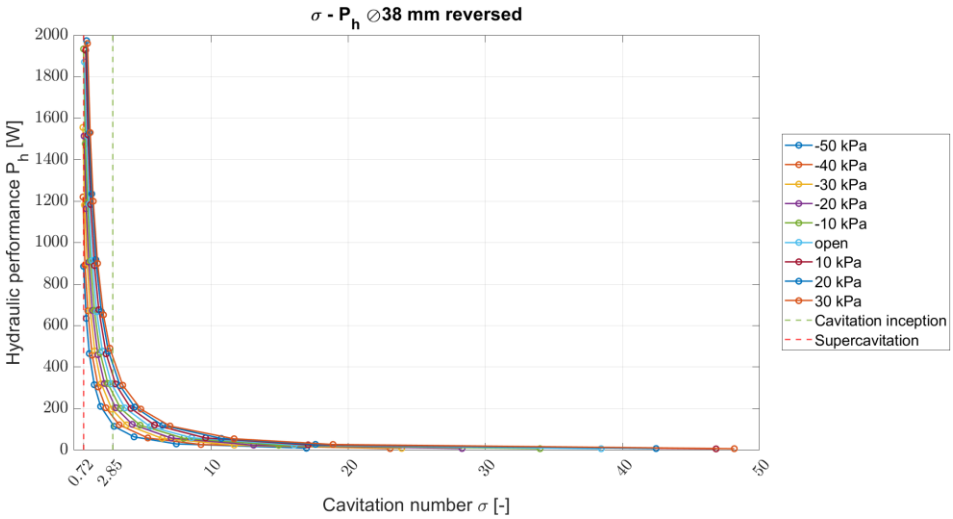

Hydraulic performance on cavitation number for cavitator with diameter 38 mm reversed

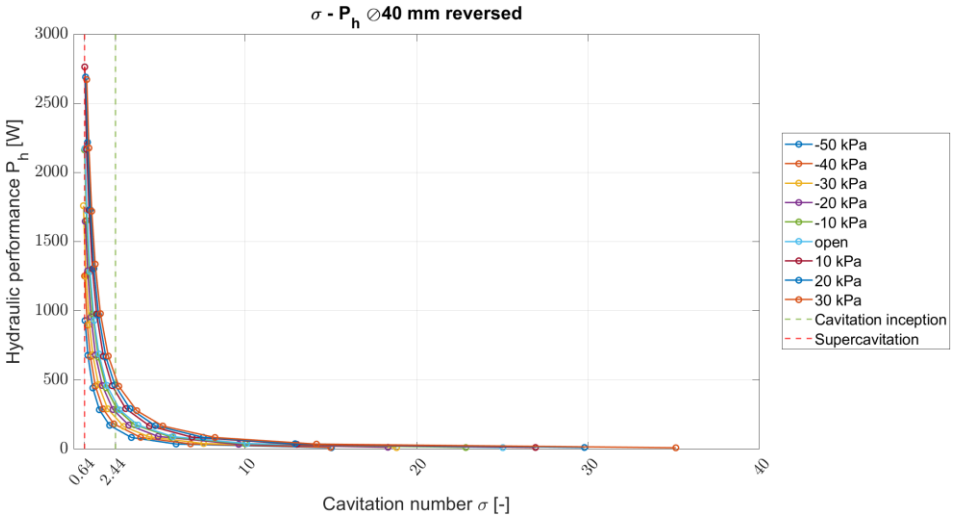

Hydraulic performance on cavitation number for cavitator with diameter 40 mm reversed

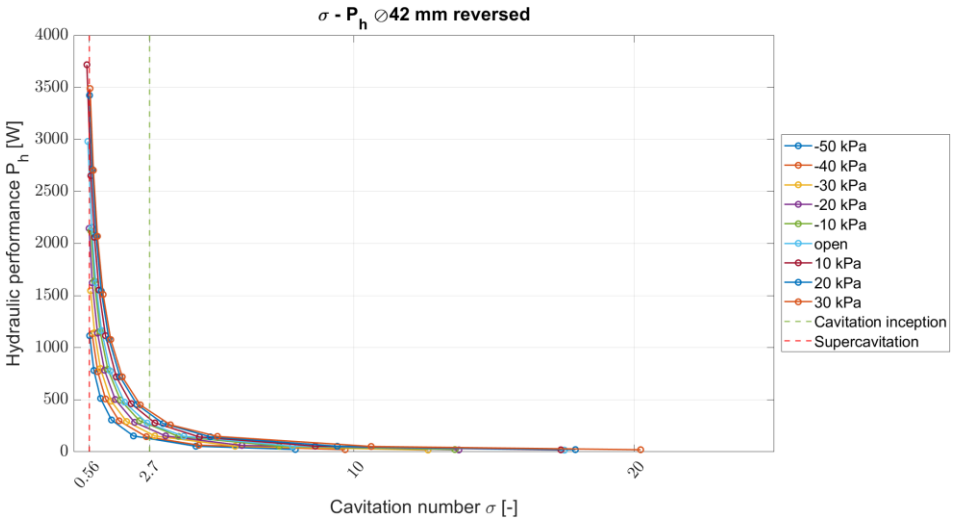

Hydraulic performance on cavitation number for cavitator with diameter 42 mm reversed

APPENDIX H - Loss coefficient on flow rate

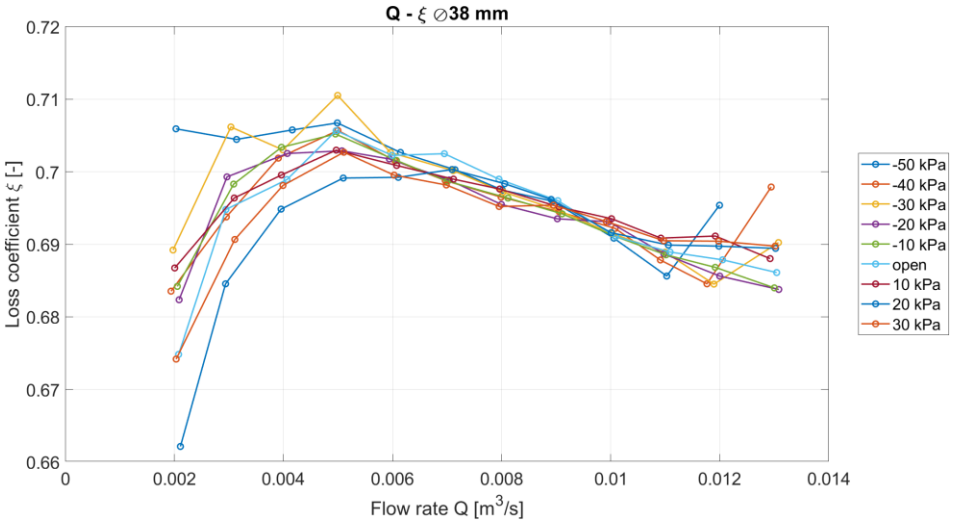

Dependancy of loss coefficient on flow rate for cavitator with diameter 38 mm

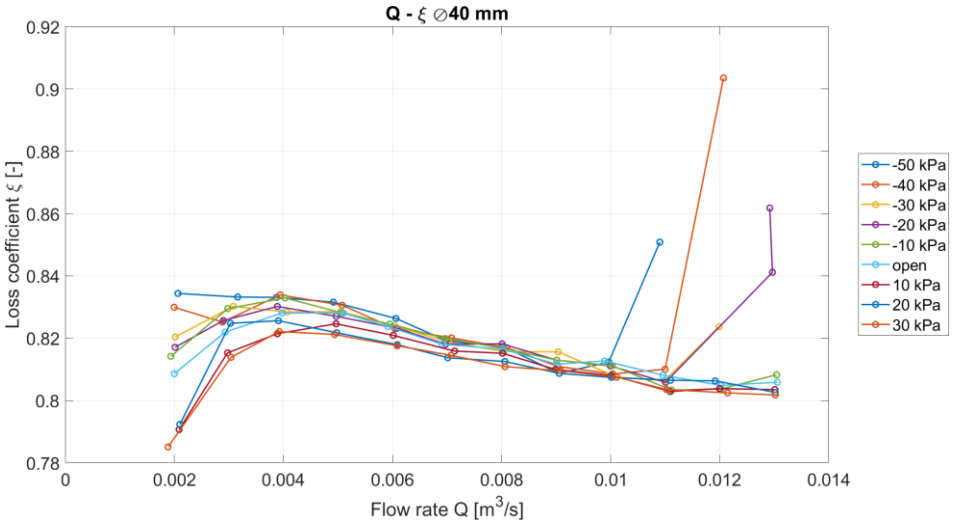

Dependancy of loss coefficient on flow rate for cavitator with diameter 40 mm

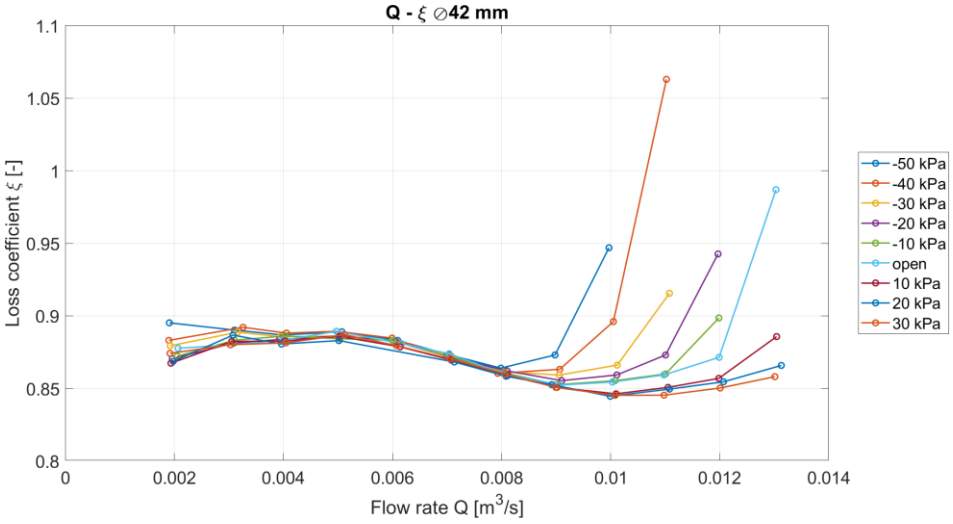

Dependancy of loss coefficient on flow rate for cavitator with diameter 42 mm

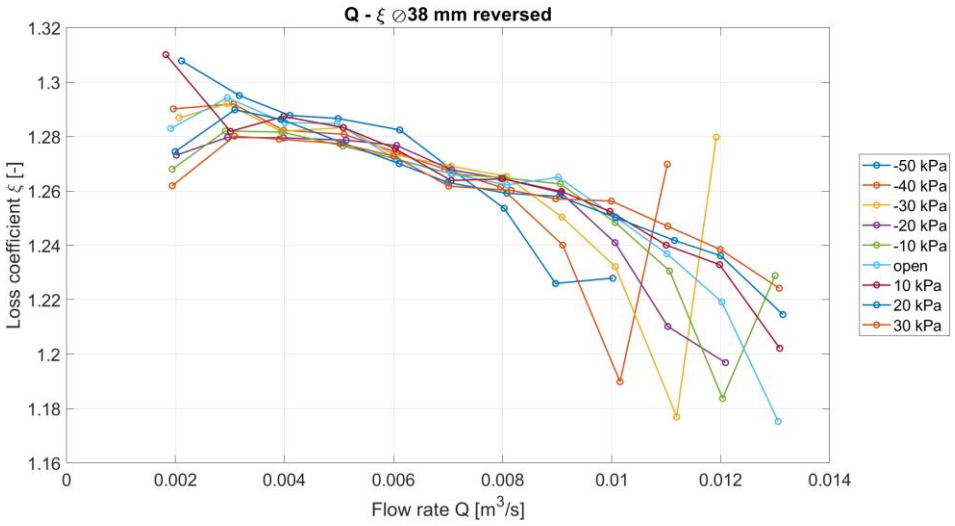

Dependancy of loss coefficient on flow rate for cavitator with diameter 38 mm reversed

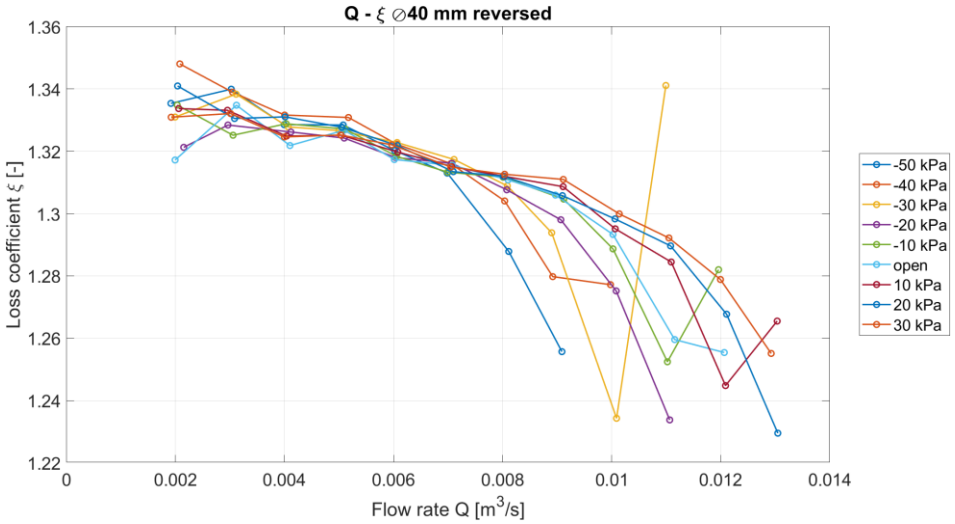

Dependancy of loss coefficient on flow rate for cavitator with diameter 40 mm reversed

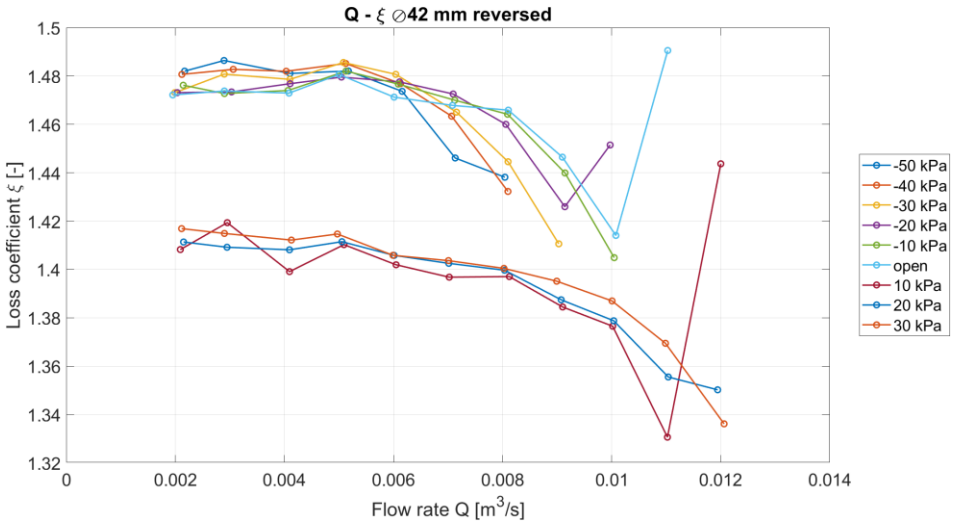

Dependancy of loss coefficient on flow rate for cavitator with diameter 42 mm reversed

APPENDIX I - Acoustic emission FFT

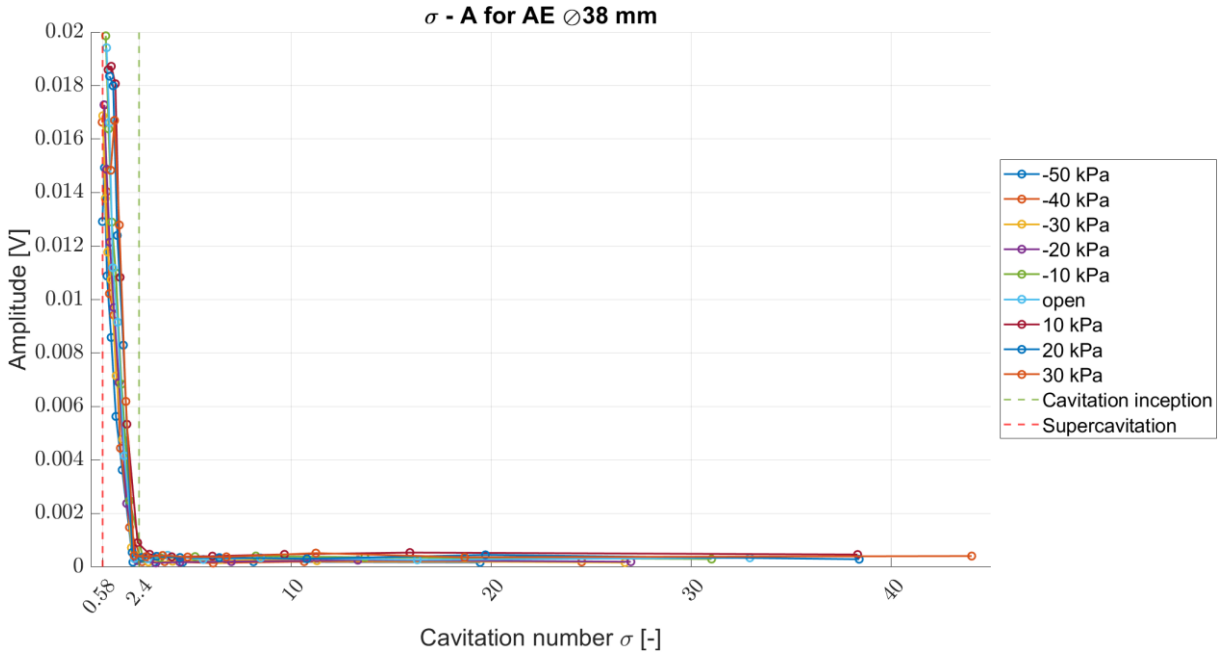

Values of peak amplitudes from FFT of AE sensor for each flow rate against cavitation number for cavitator with diameter 38 mm

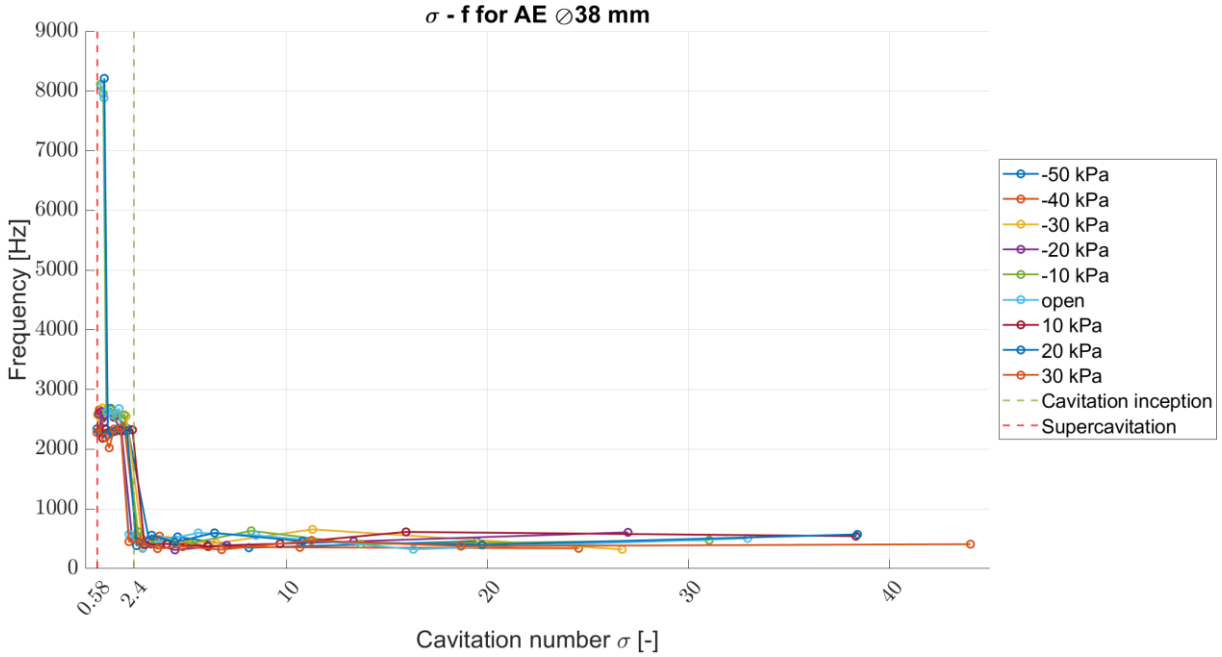

Values of peak frequencies from FFT of AE sensor for each flow rate against cavitation number for cavitator with diameter 38 mm

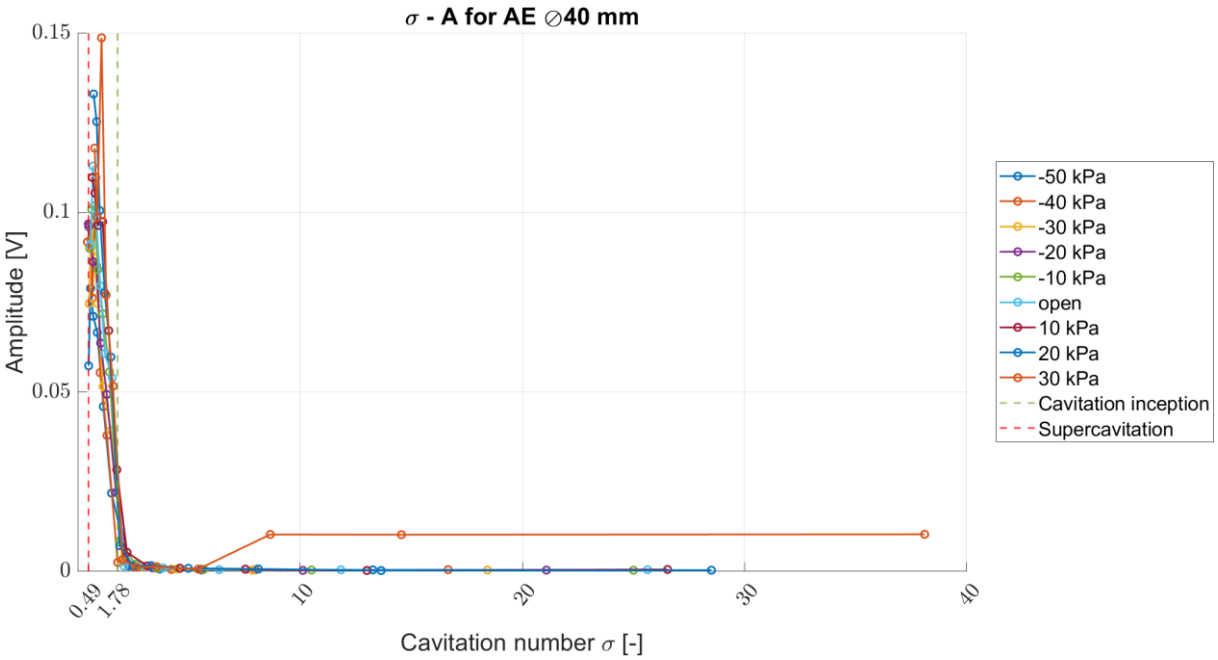

Values of peak amplitudes from FFT of AE sensor for each flow rate against cavitation number for cavitator with diameter 40 mm

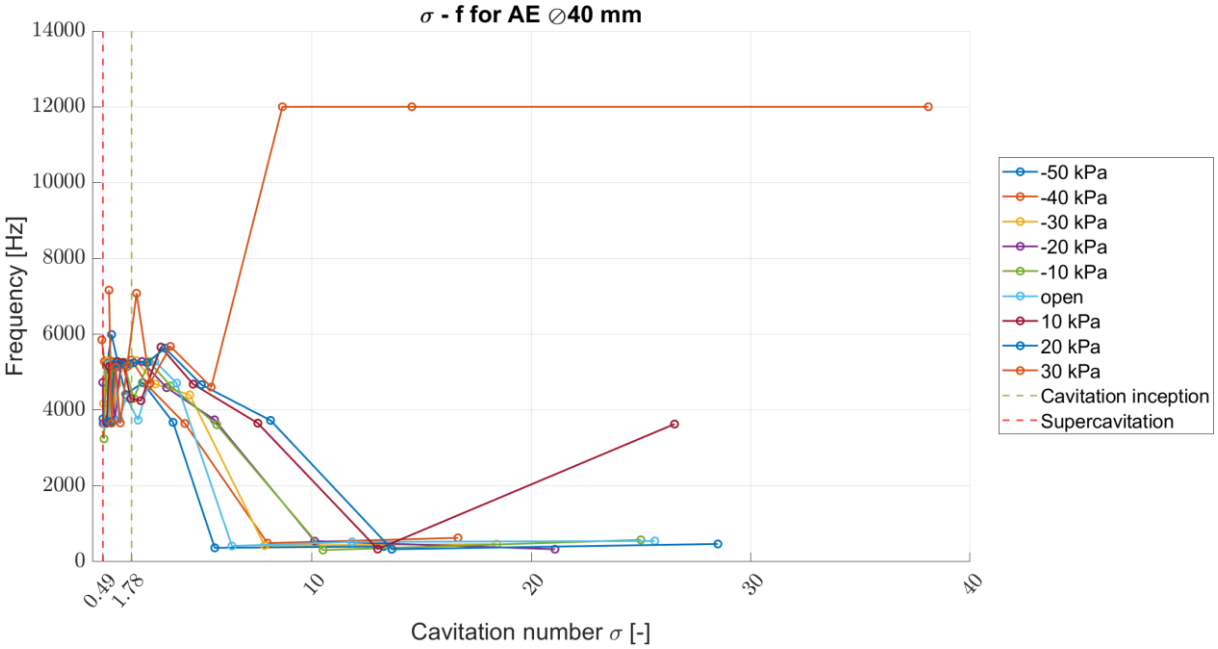

Values of peak frequencies from FFT of AE sensor for each flow rate against cavitation number for cavitator with diameter 40 mm

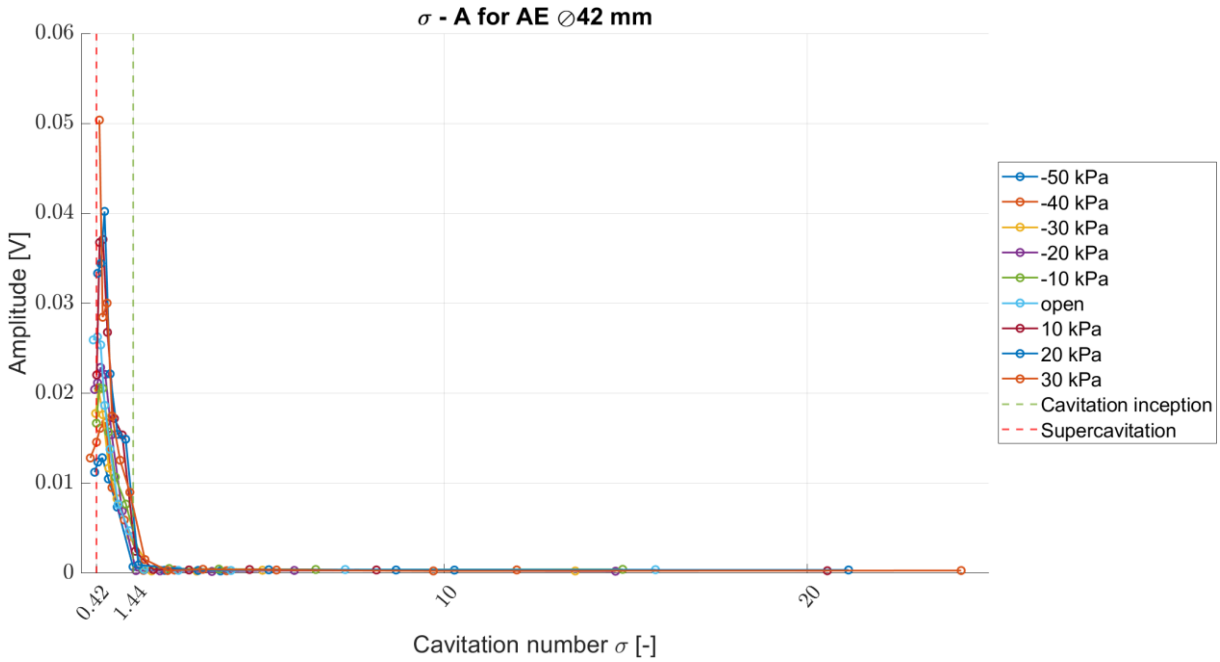

Values of peak amplitudes from FFT of AE sensor for each flow rate against cavitation number for cavitator with diameter 42 mm

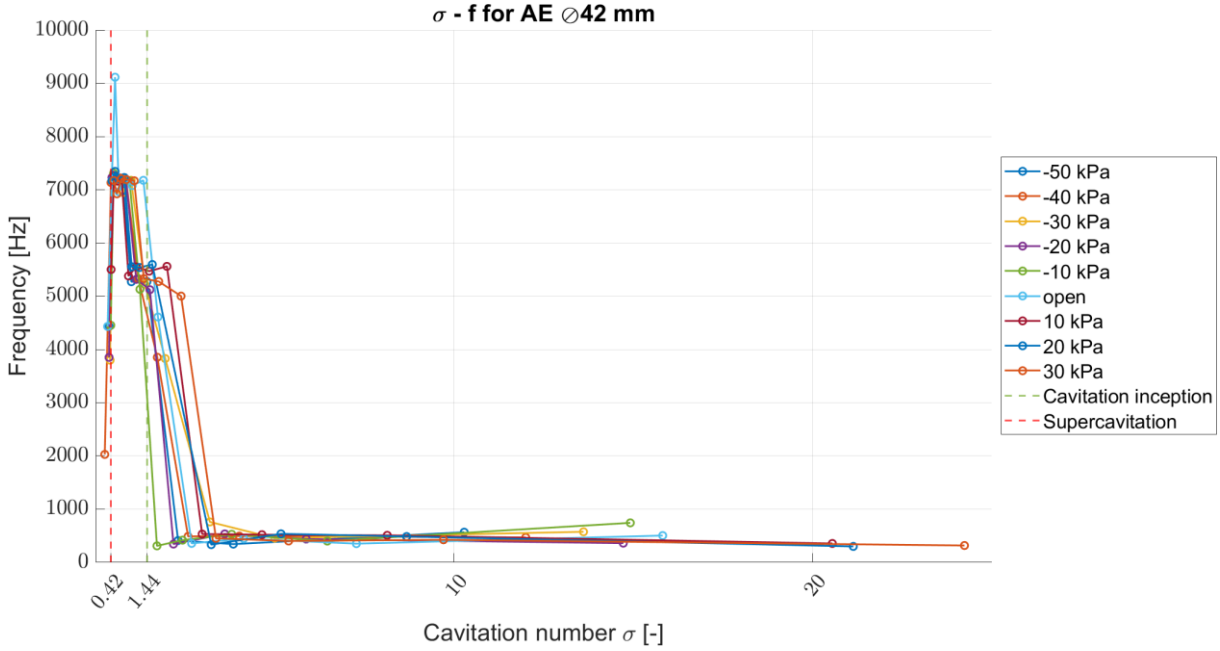

Values of peak frequencies from FFT of AE sensor for each flow rate against cavitation number for cavitator with diameter 42 mm

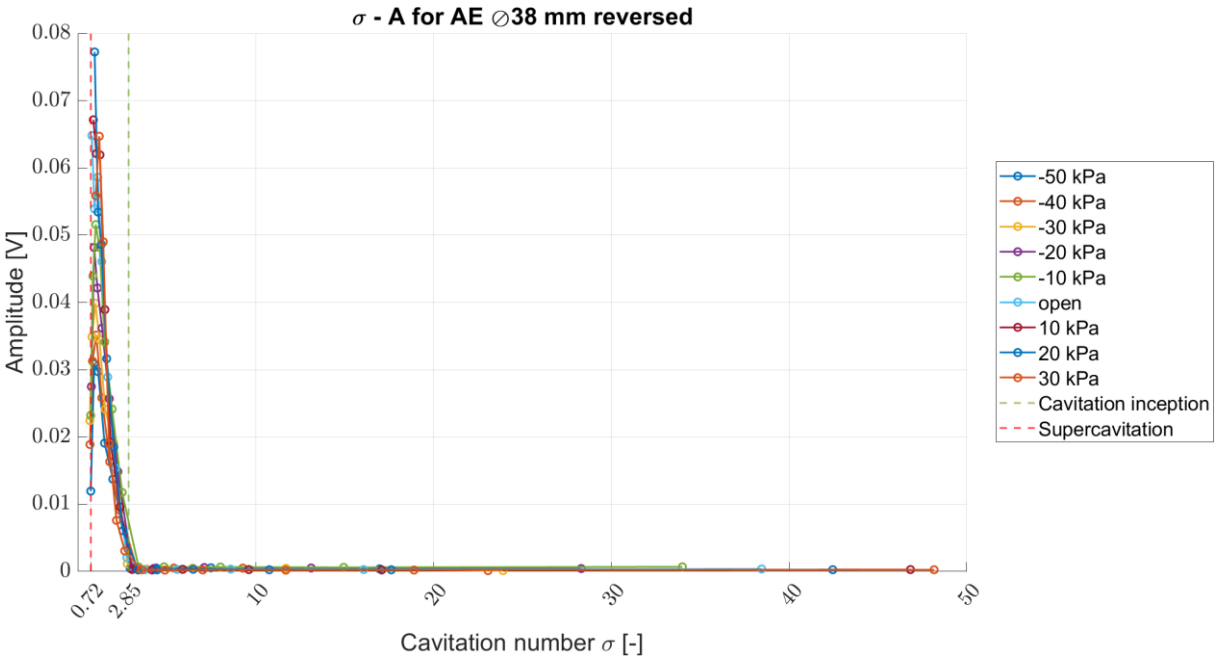

Values of peak amplitudes from FFT of AE sensor for each flow rate against cavitation number for cavitator with diameter 38 mm reversed

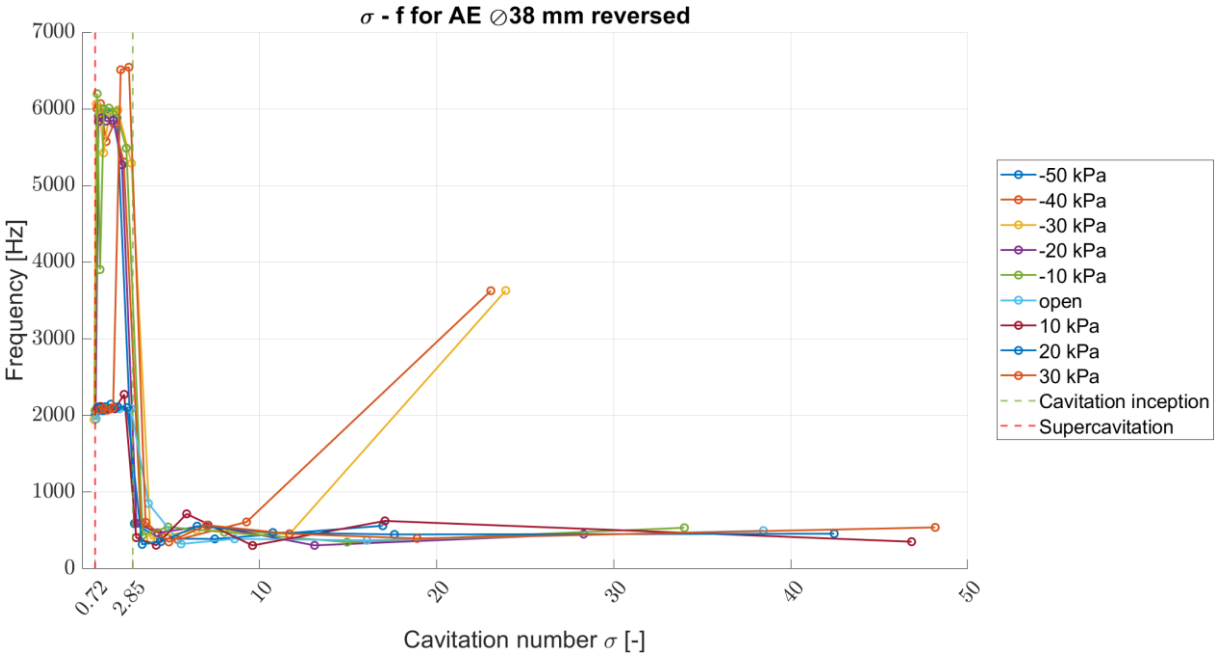

Values of peak frequencies from FFT of AE sensor for each flow rate against cavitation number for cavitator with diameter 38 mm reversed

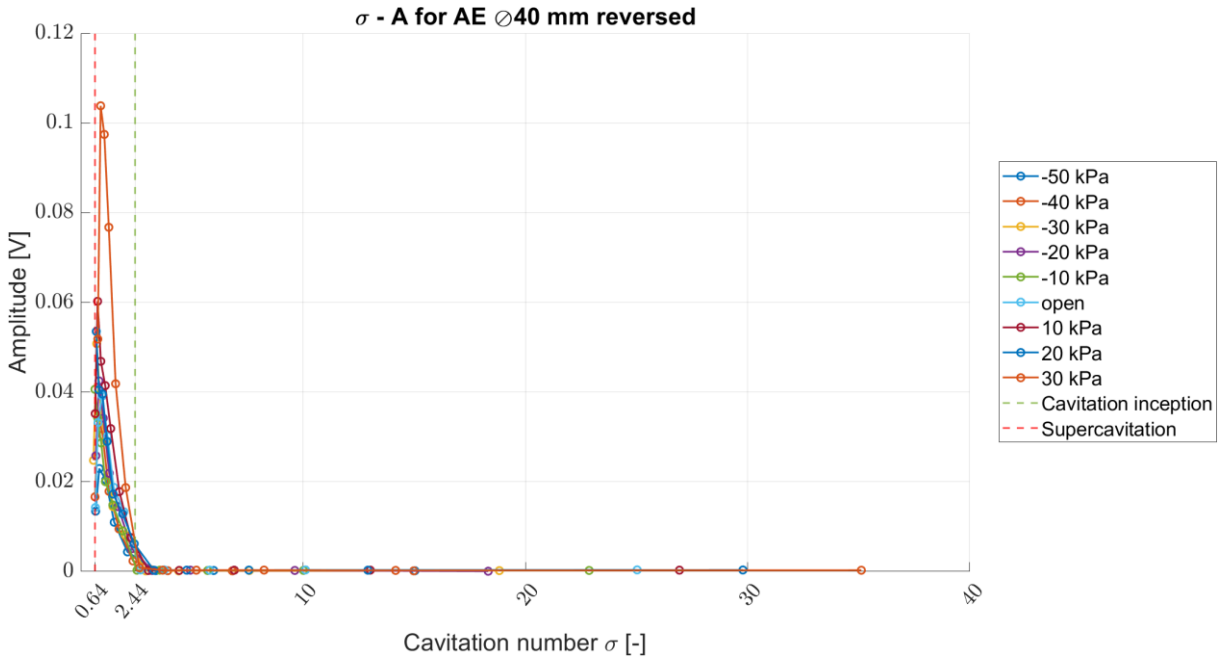

Values of peak amplitudes from FFT of AE sensor for each flow rate against cavitation number for cavitator with diameter 40 mm reversed

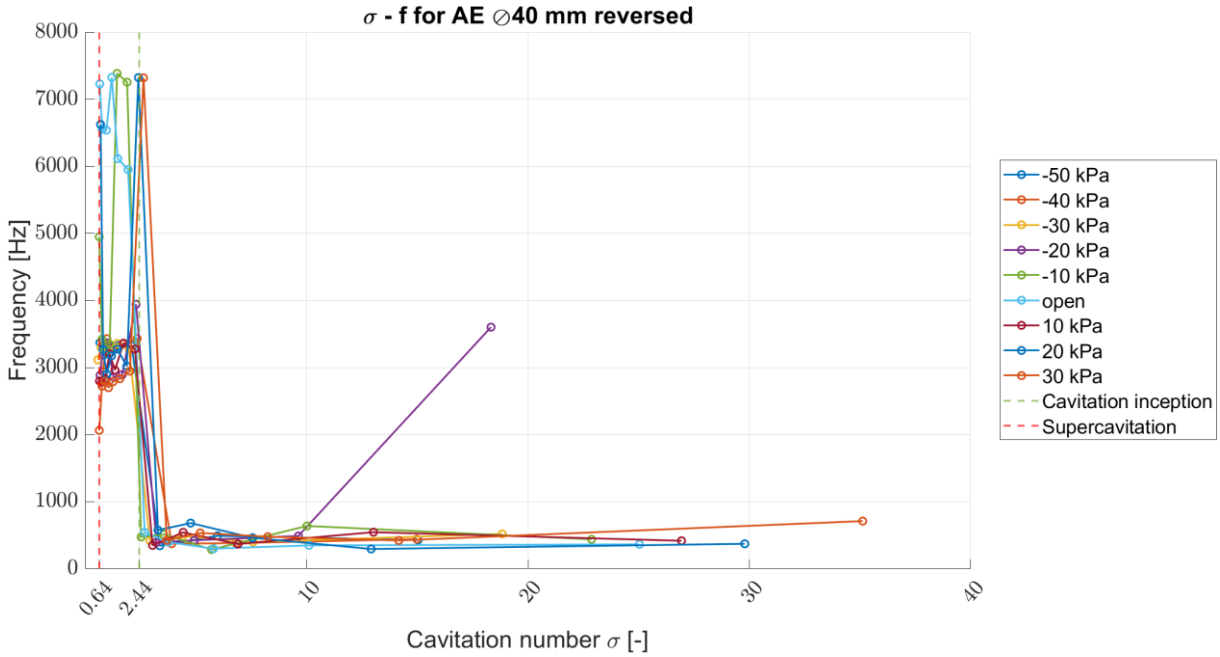

Values of peak frequencies from FFT of AE sensor for each flow rate against cavitation number for cavitator with diameter 40 mm reversed

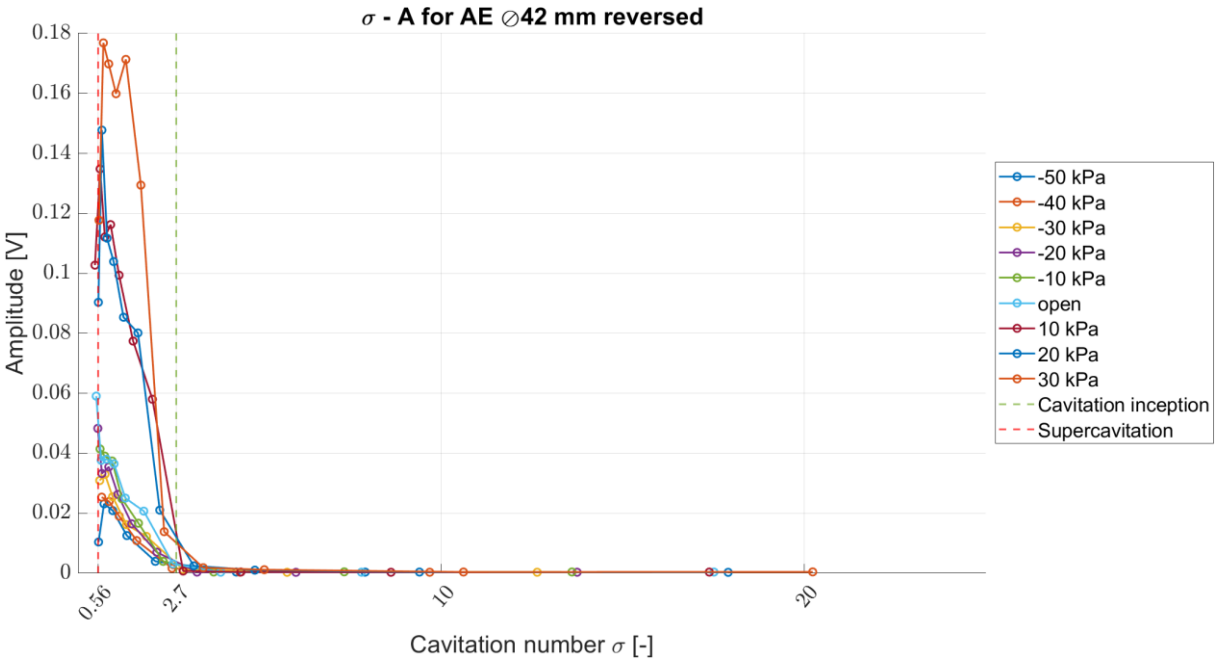

Values of peak amplitudes from FFT of AE sensor for each flow rate against cavitation number for cavitator with diameter 42 mm reversed

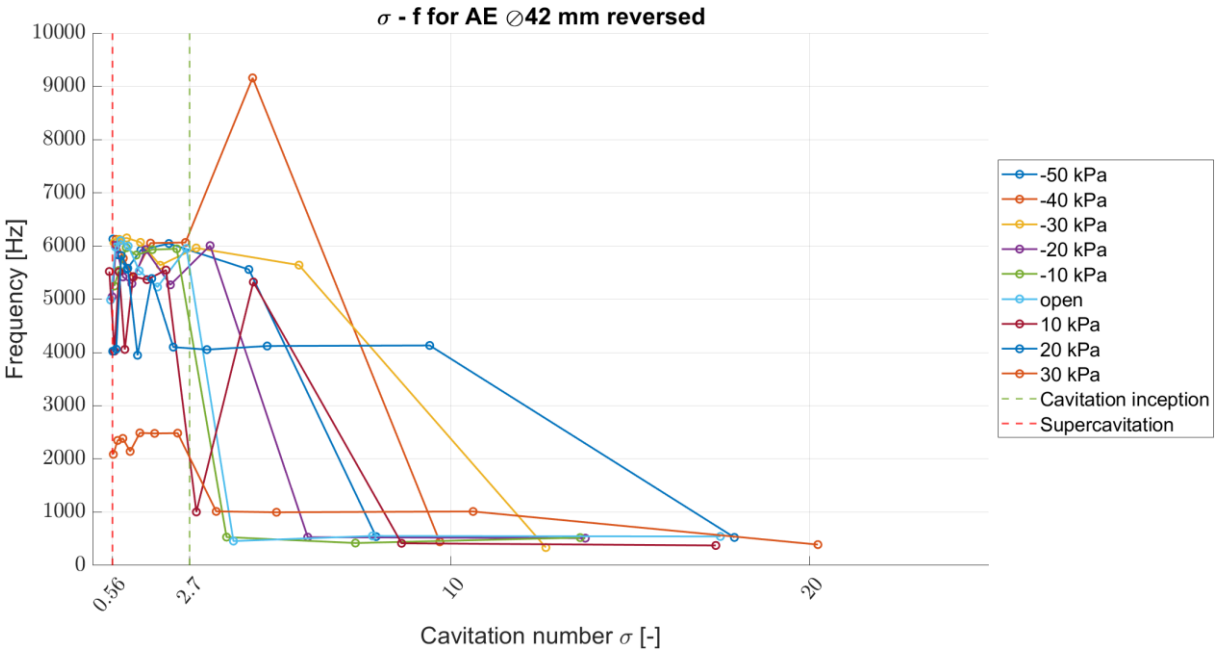

Values of peak frequencies from FFT of AE sensor for each flow rate against cavitation number for cavitator with diameter 42 mm reversed

APPENDIX J - Pressure sensor FFT

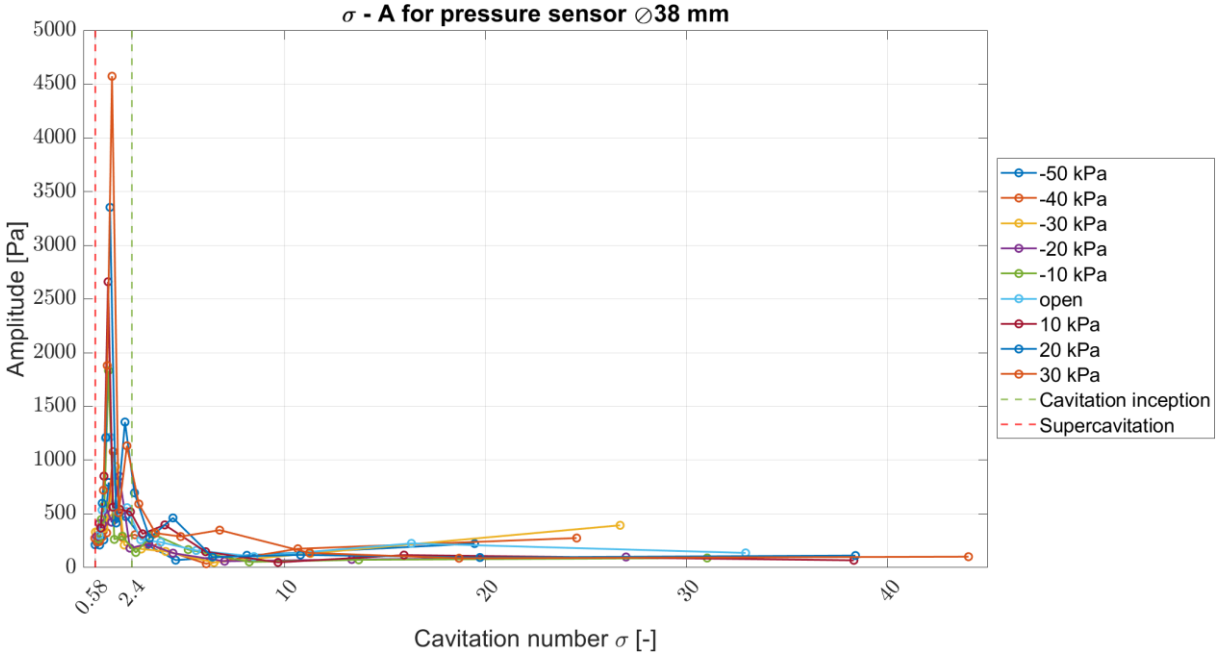

Values of peak amplitudes from FFT of pressure sensor for each flow rate against cavitation number for cavitator with diameter 38 mm

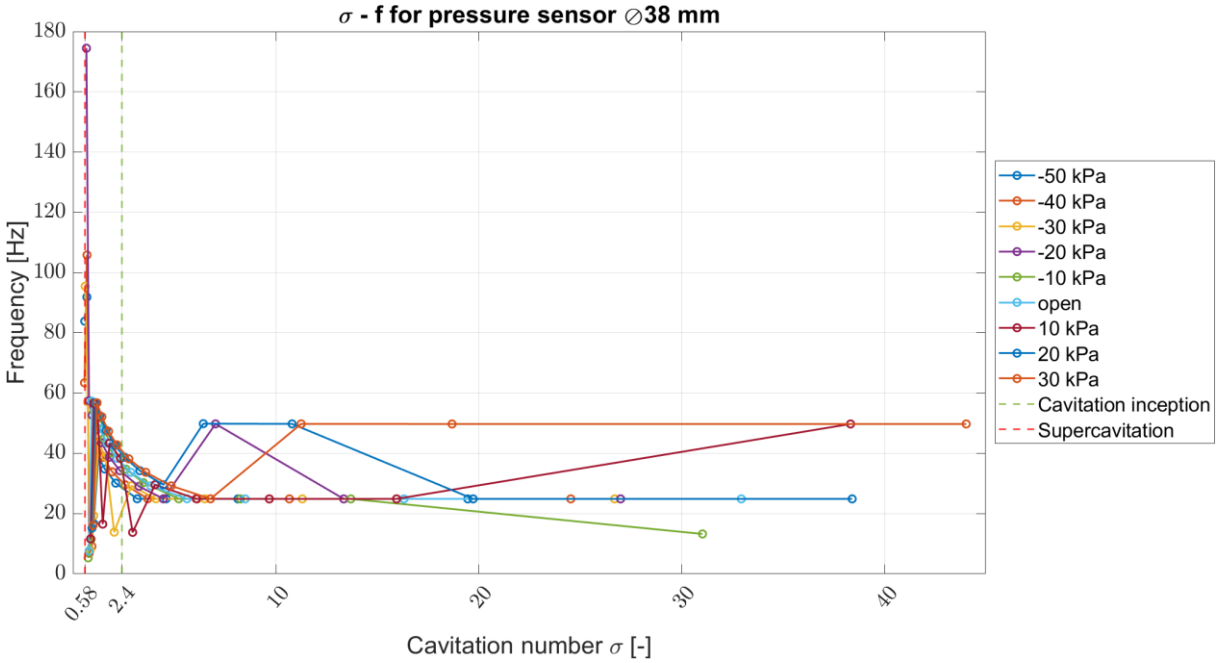

Values of peak frequencies from FFT of pressure sensor for each flow rate against cavitation number for cavitator with diameter 38 mm

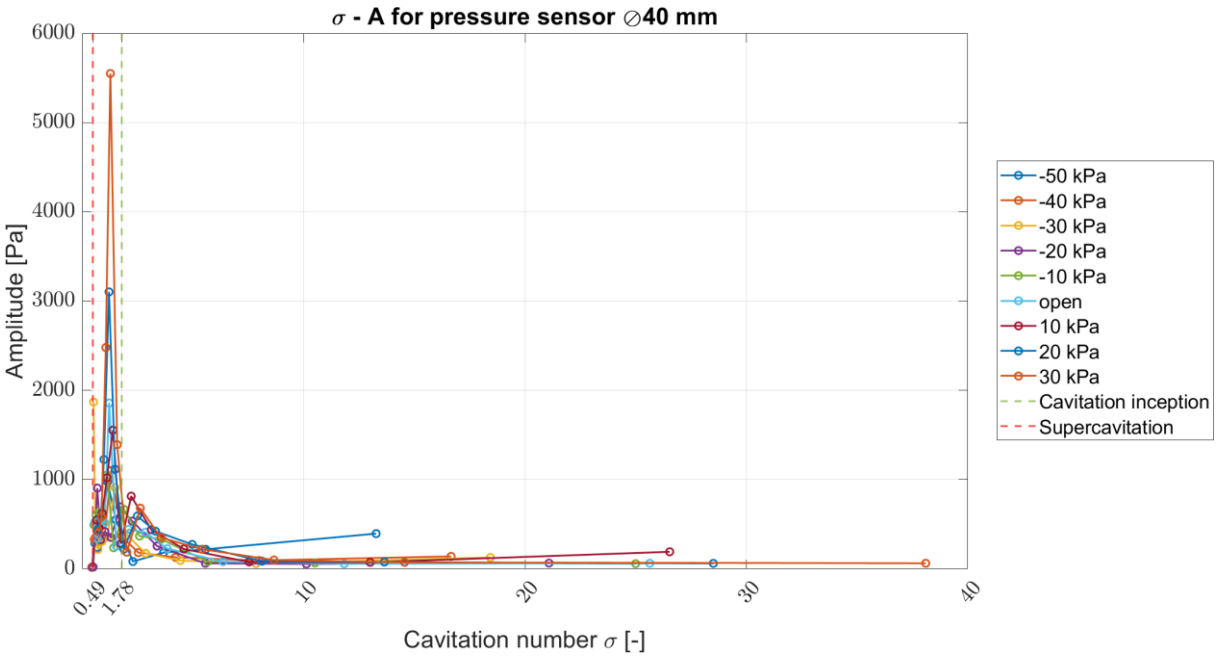

Values of peak amplitudes from FFT of pressure sensor for each flow rate against cavitation number for cavitator with diameter 40 mm

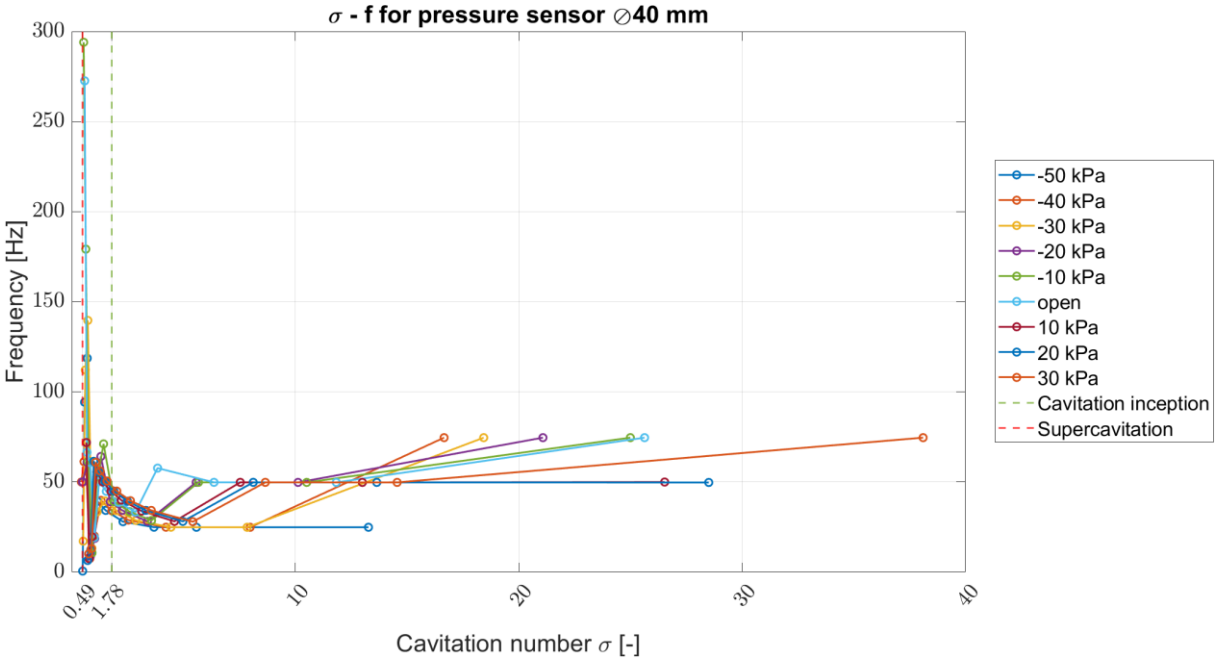

Values of peak frequencies from FFT of pressure sensor for each flow rate against cavitation number for cavitator with diameter 40 mm

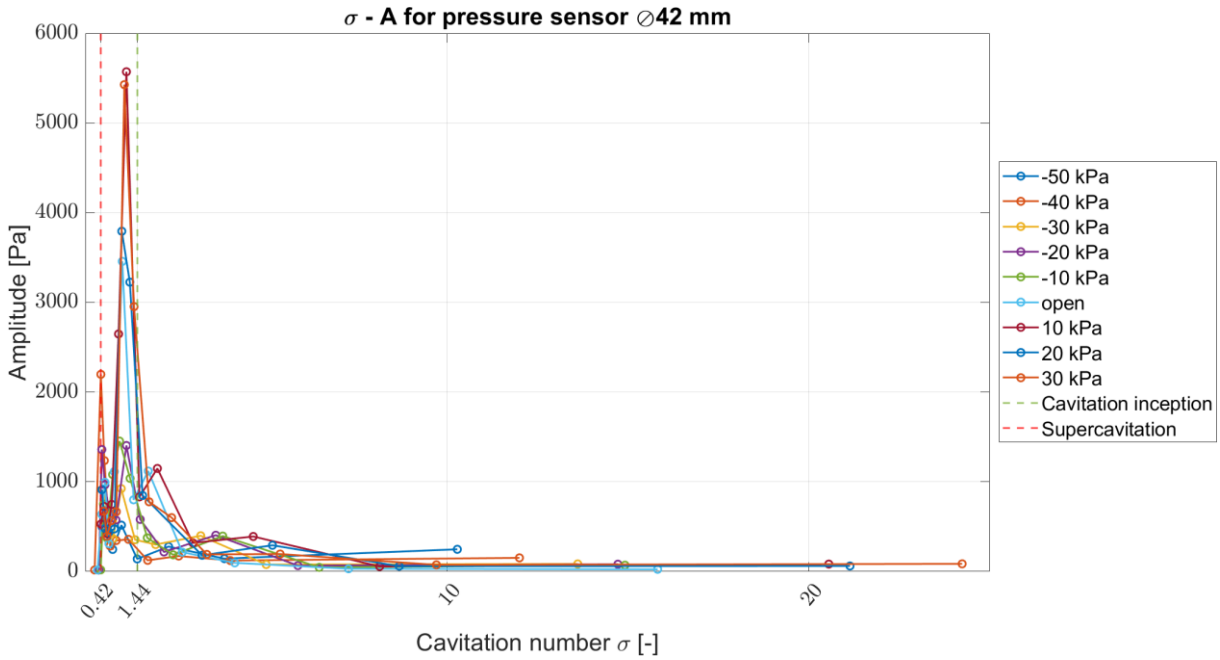

Values of peak amplitudes from FFT of pressure sensor for each flow rate against cavitation number for cavitator with diameter 42 mm

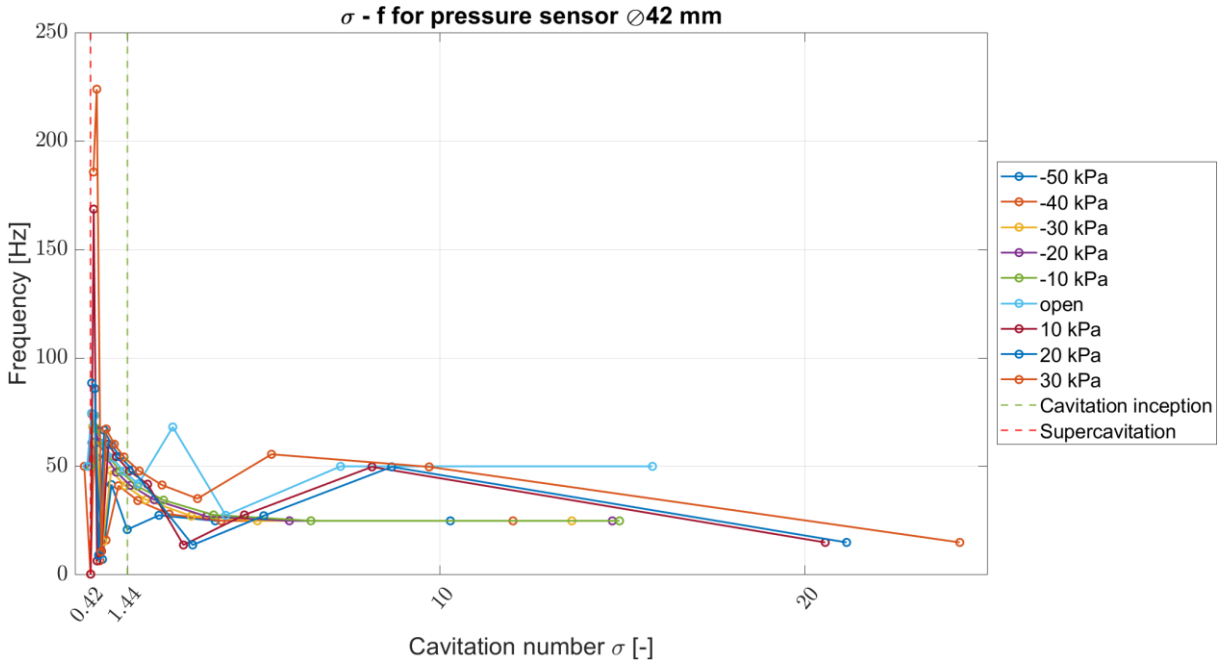

Values of peak frequencies from FFT of pressure sensor for each flow rate against cavitation number for cavitator with diameter 42 mm

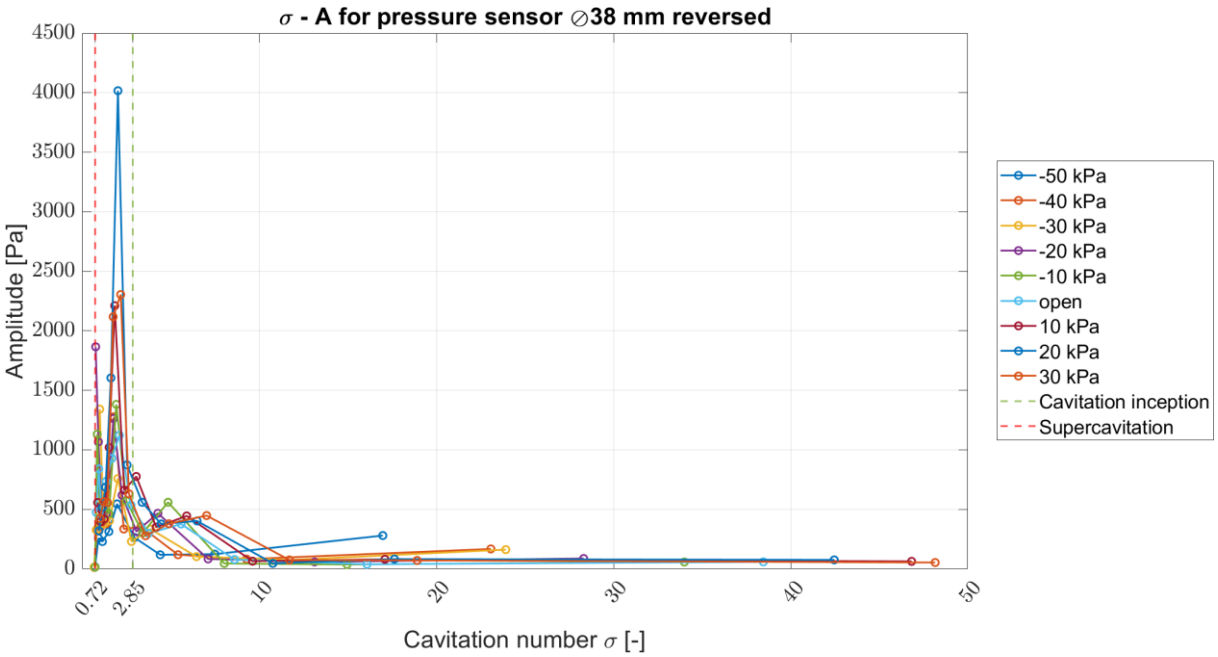

Values of peak amplitudes from FFT of pressure sensor for each flow rate against cavitation number for cavitator with diameter 38 mm reversed

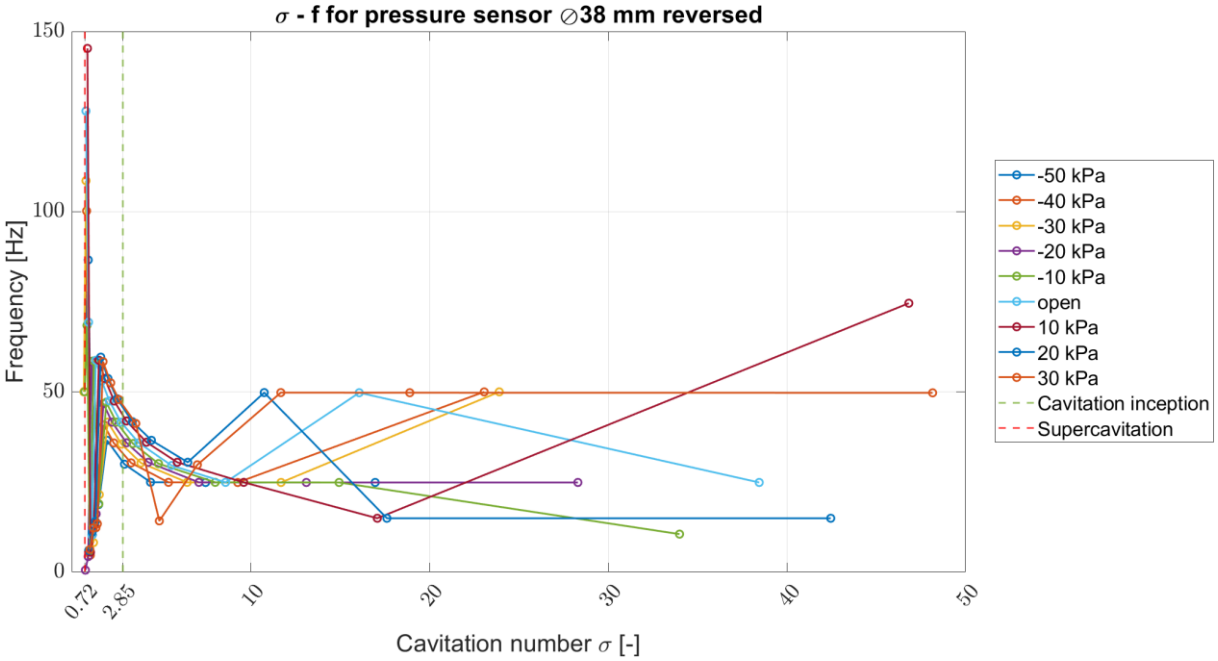

Values of peak frequencies from FFT of pressure sensor for each flow rate against cavitation number for cavitator with diameter 38 mm reversed

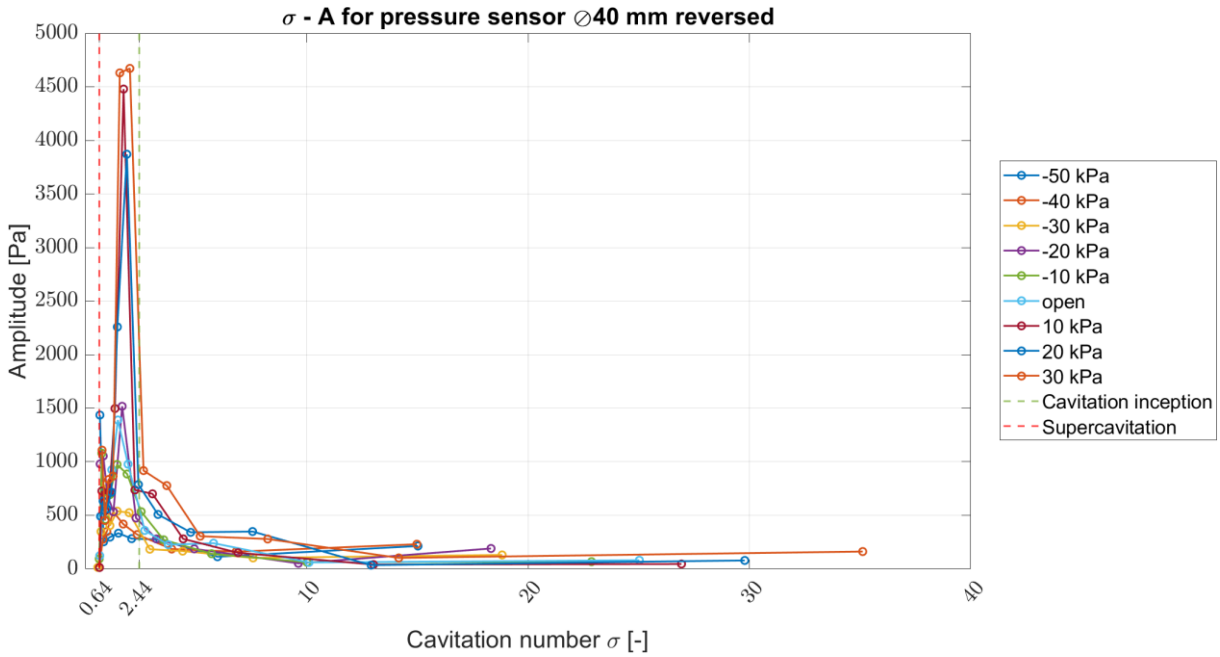

Values of peak amplitudes from FFT of pressure sensor for each flow rate against cavitation number for cavitator with diameter 40 mm reversed

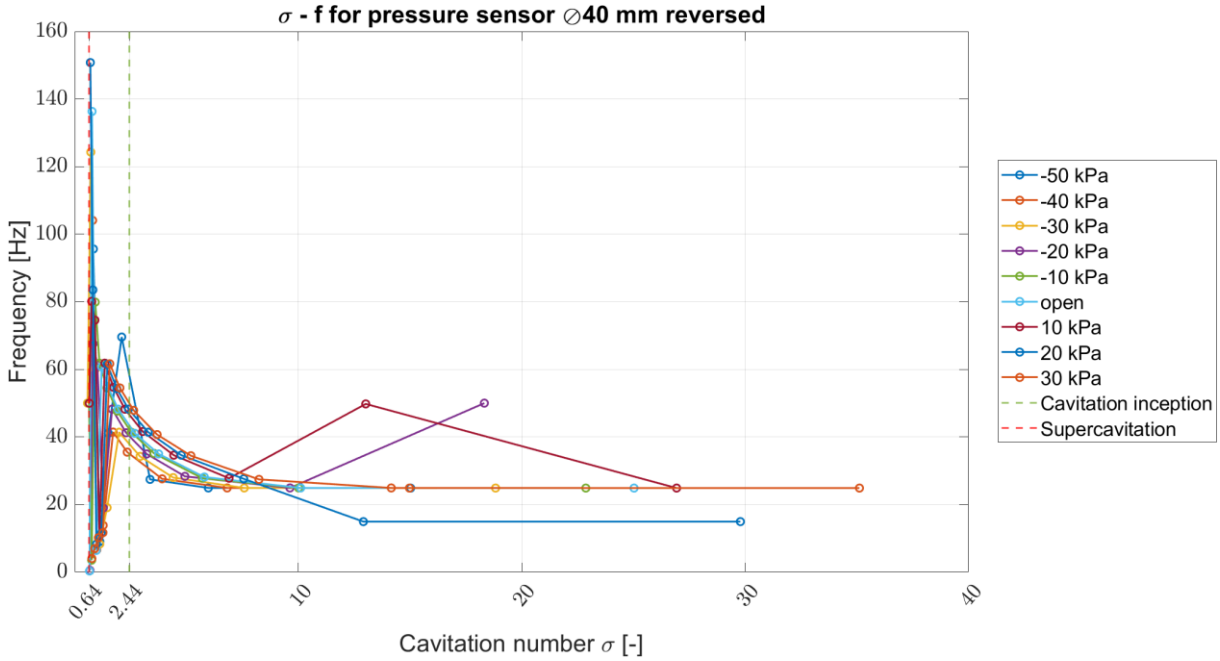

Values of peak frequencies from FFT of pressure sensor for each flow rate against cavitation number for cavitator with diameter 40 mm reversed

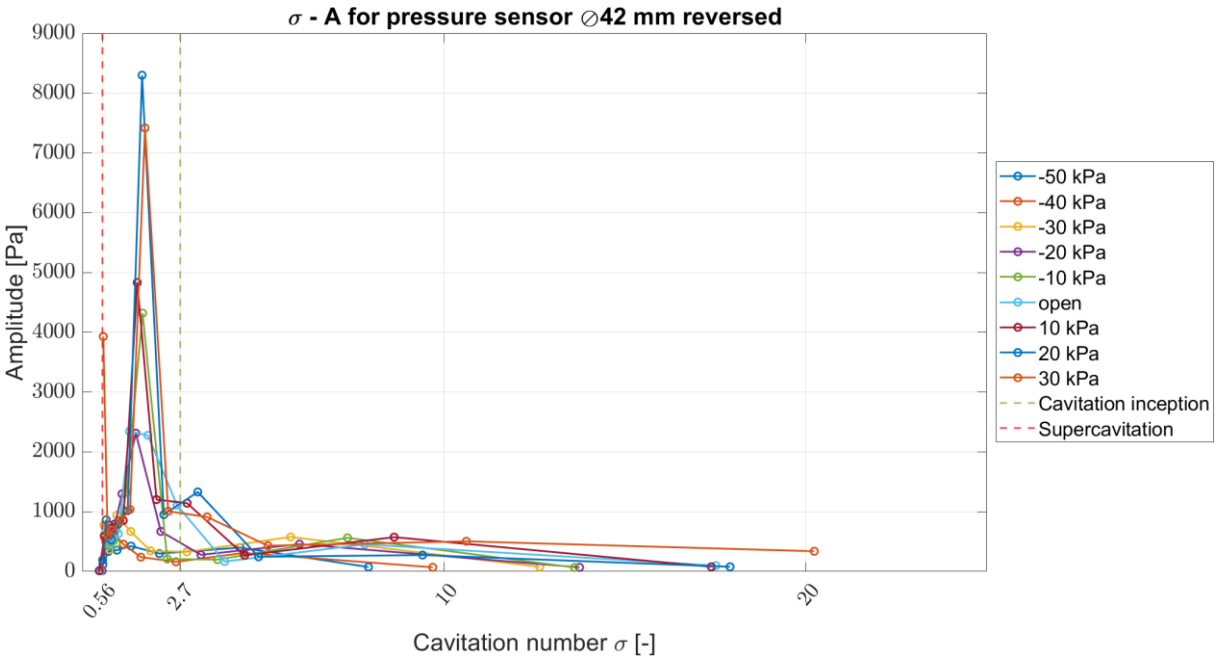

Values of peak amplitudes from FFT of pressure sensor for each flow rate against cavitation number for cavitator with diameter 42 mm reversed

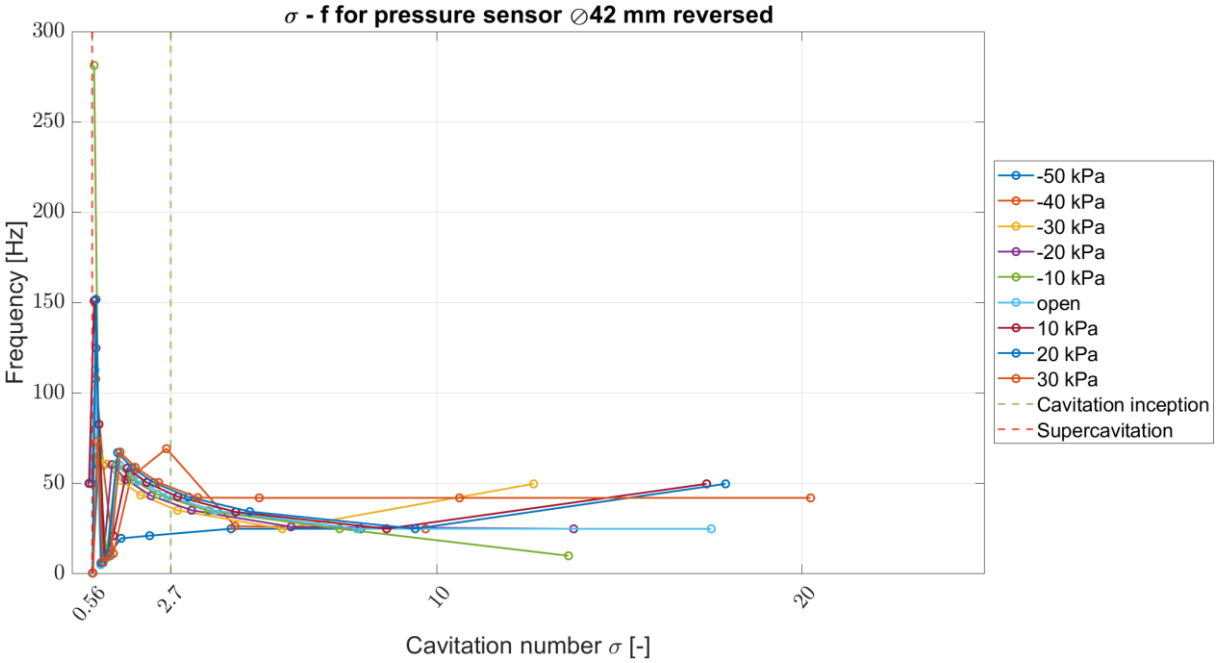

Values of peak frequencies from FFT of pressure sensor for each flow rate against cavitation number for cavitator with diameter 42 mm reversed

APPENDIX K - Acoustic emission RMS

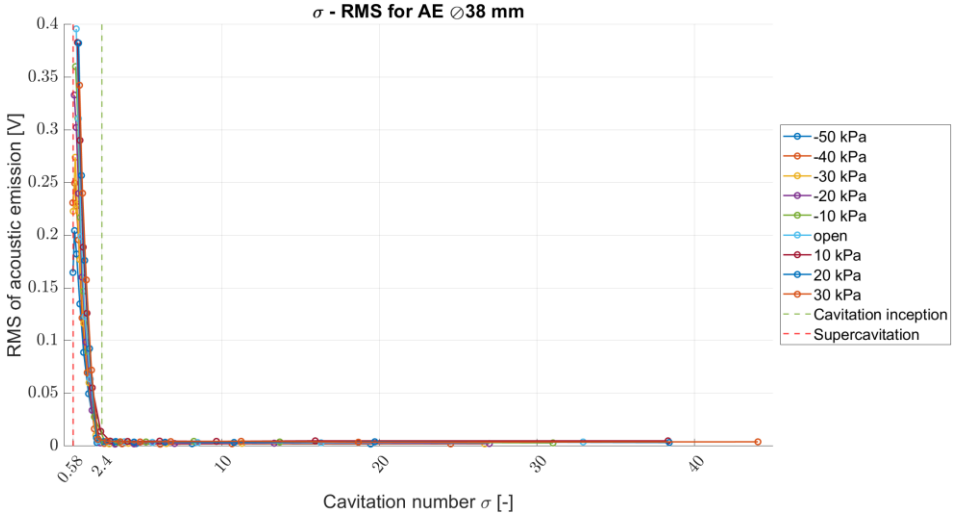

RMS values for each flow rate against cavitation number for cavitator with diameter 38 mm

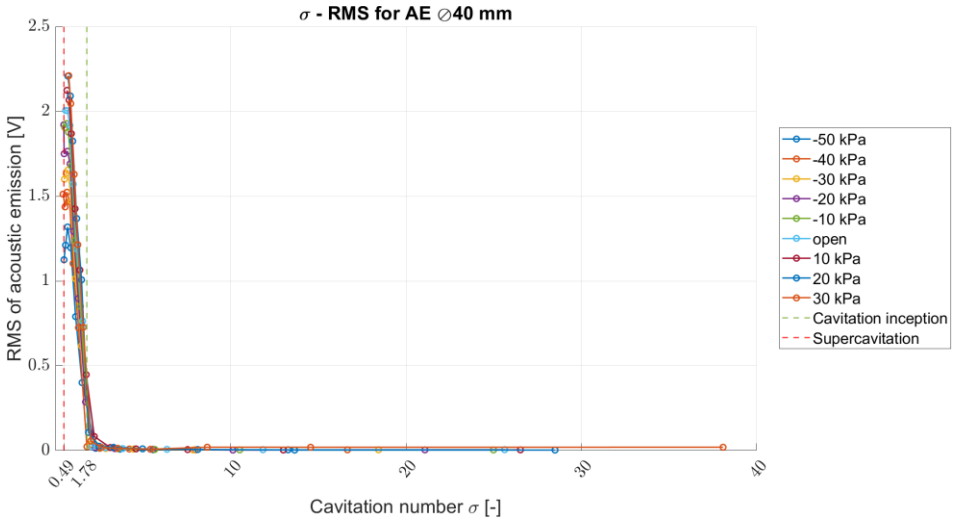

RMS values for each flow rate against cavitation number for cavitator with diameter 40 mm

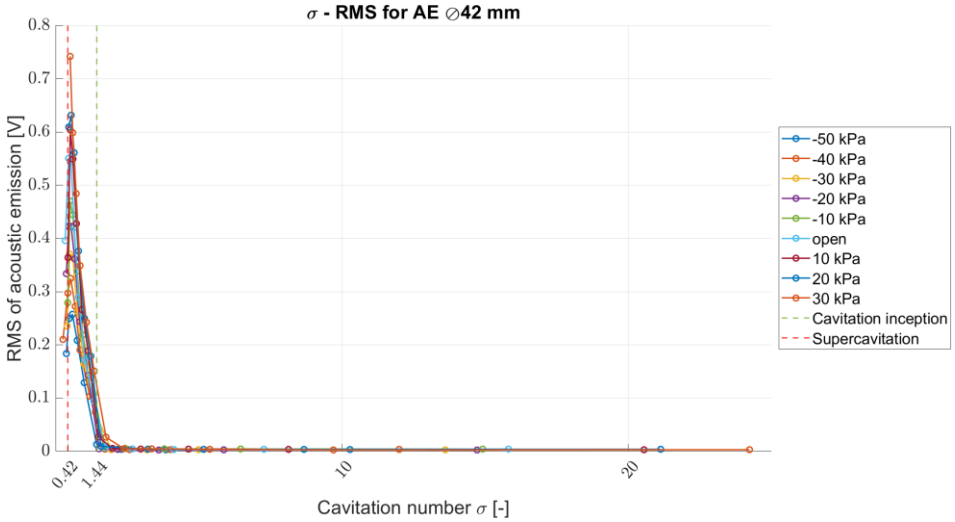

RMS values for each flow rate against cavitation number for cavitator with diameter 42 mm

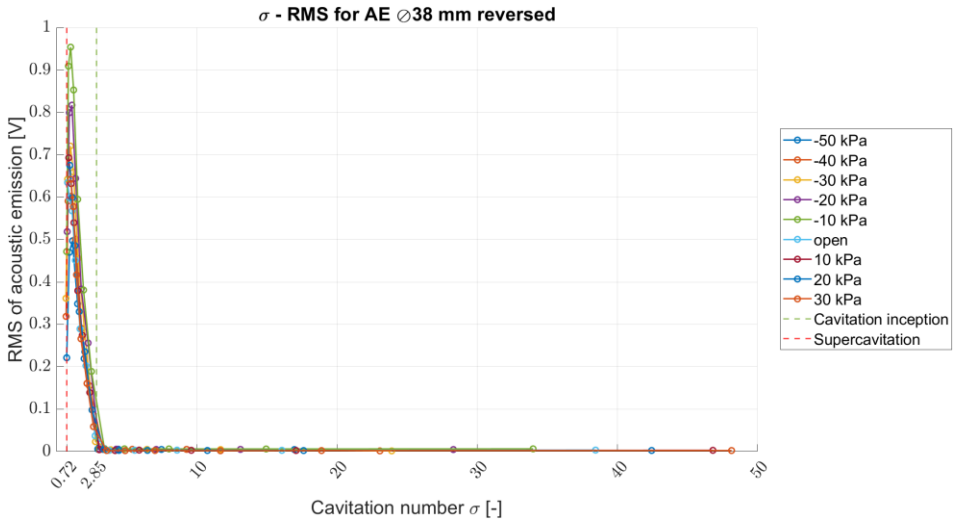

RMS values for each flow rate against cavitation number for cavitator with diameter 38 mm reversed

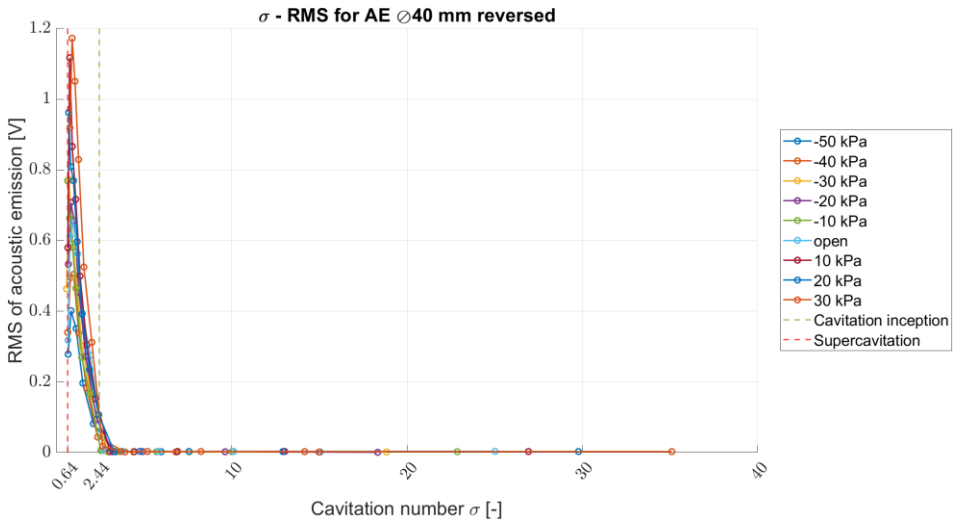

RMS values for each flow rate against cavitation number for cavitator with diameter 40 mm reversed

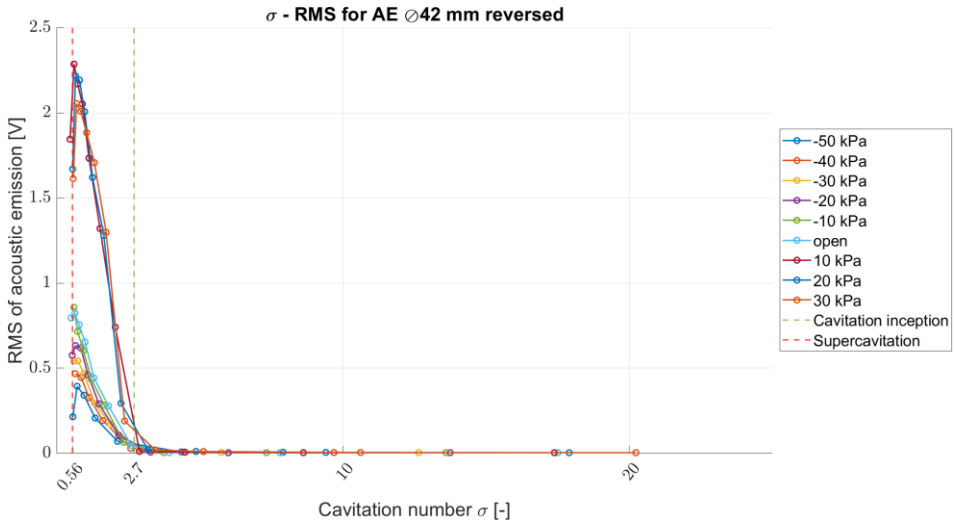

RMS values for each flow rate against cavitation number for cavitator with diameter 42 mm reversed